PHOTOPRODUCTION OF THE $\Lambda^*(1520)$ HYPERON

OFF PROTONS AND NEUTRONS IN DEUTERIUM

By

Zhiwen Zhao

Bachelor of Science
Shanxi University 1999, China
Master of Science
Institute of Physics, Chinese Academy of Sciences 2002, China

_____

Submitted in Partial Fulfillment of the Requirements

for the Degree of Doctor of Philosophy in

Physics

College of Arts and Sciences

University of South Carolina

2010

Accepted by:

Ralf W. Gothe, Major Professor

Elton S. Smith, Committee Member

Chaden Djalali, Committee Member

Yordanka Ilieva, Committee Member

James Buggy, Interim Dean of the Graduate School

DEDICATION

To this Universe

Acknowledgments

The biggest thank goes to my adviser, Ralf Gothe, who has created a sense of no boundary for me to pursue some crazy ideas and maintained a high standard when I tried to prove the ideas right or wrong. My journey of getting a PhD would not have been so enjoyable without those energetic and lengthy discussions with him. My academic style will be imprinted with his strong and colorful force for the years to come. And I know I will always come back for visit no matter if his wife will bake her magic cake for us.

I can not thank enough all CLAS eg3 collaborators. Many of them are also my group mates. Jörn Langheinrich has shown me how to do CLAS analysis for the very first time and my main analysis code is entirely based on his code. He is such a quick shooter for physics problems and always writes programs with beyond-me-complexity. Haiyun Lu and Lewis Graham, and I started our PhD programs at the same time and all worked with eg3 experiment. We were comrades on the same boat and had totally enjoyed the up and down times together through the amazing ride. So hi, guys, you are welcome. I would like thank Elton Smith for organizing the eg3 effort through out the years and gracefully served on my thesis committee. I would like thank Stepan Stepanyan for being the go-to person for me wherever I had any question about the CLAS detector and its physics. I would like thank Hovanes Egiyan and Kijun Park for provide me endless helps on data analysis. I would like thank Paul Mattione for doing a lot of work for eg3 so I can just pick the fruits. Many thanks go to Eugene Pasyuk, Raffaella De Vita, Maurik Holtrop, Maurizio Ungaro, David Tedeschi, Steffen Strauch, Nathan Baltzell, Michael Paolone, Rakhsha Nasseripour,

Henry Juengst, Pawel Nadel-Turonski, and other eg3 collaborators or general CLAS members. It was a collaboration after all. Special thanks go to the wonderful Chaden Djalali and Yordanka Ilieva who were on my thesis committee. Also thank you, the rest of my group members, Evan Phelps, Ye Tian, Robert Steinman and Joshua Witthuhn, you guys are good company. Thanks should go other teachers I had in the US, Fred Myhrer, Kuniharu Kubodera, Pawel Mazur, Milind Purohit, Varsha Kulkarni, Shmuel Nossinov, Eva Andrei etc and the teachers I had in the past, Haihu Wen, Deming Li, Changmin Chen, Dachun Su, Lu Li, Jiuqing Liang, Changde Xie, Kunchi Peng, jinfen Wang etc, who put bricks down and lighted up the road.

Please allow me to thank some people from the actual world and for non-physics reasons. I want to thank my wife for standing by me no matter what. Sweetheart, you are right, always. To my parents, I am deeply indebted for this life, the freedom to explore its meaning and their sacrifice. Thanks goes to my brother, my grandparents, my in-laws and all the rest of our big family for being there for me. I would like thank our department staff, Beth Powell, Mary Papp, Dee Brown, Laura Bouknight, Robert Sproul, and Richard Hoskins for making everyday life easy. Last but not least, thank you, all my friends in US and China. I am running out of space on this page, so you know I mean you, right? Finally, I thank my daughter for carrying my genes without complaining so far and starting another iteration to measure the world with improved accuracy.

ABSTRACT

The photoproduction of the $\Lambda^*(1520)$ off both protons and neutrons in deuterium has been studied using the CLAS eg3 run data. The reactions are $\gamma d \rightarrow K^+\Lambda^*(n)$ and $\gamma d \rightarrow K^0\Lambda^*(p)$. $\Lambda^*(1520)$ cross sections and decay angle distributions are extracted in the photon energy region 1.75 GeV $< E_\gamma <$ 5.50 GeV. This is the first time that exclusive photoproduction of $\Lambda^*(1520)$ on neutrons has been reported. Moreover our results on protons extend to higher energies than the previous studies.

Contents

LIST OF TABLES

LIST OF FIGURES

xv

xvii

CHAPTER 1

INTRODUCTION

1.1. STRONG FORCE AND QCD

There are four fundamental forces being found so far in the physical world. The gravitational force forms stars, galaxies, and large-scale structures in the universe. The electromagnetic force binds nuclei and electrons together to form atoms, which are the building blocks of everyday matter. The strong force holds quarks together to form nucleons (protons and neutrons) and holds nucleons together to form nuclei, which are responsible for most of the mass in the visible universe. To make it more interesting, the weak force changes quark flavors and breaks parity. With the exception of gravity, the other three forces are unified in the Standard Model.

Within this frame work, the electromagnetic and weak force can be described by a single theory: the electro-weak Quantum Electrodynamics (QED) [8]. The basic elements are quarks and leptons, and the force carriers are photon, W and Z bosons. QED has been tested by experiments with unprecedented precision, but this is not the case for Quantum Chromodynamics (QCD) [9], which is the fundamental theory describing the strong force. The complication is due to the strong force carriers, gluons, having the ability of interacting with each other unlike the electro-weak force carriers. When quarks, the basic elements of the strong force, are close to each other, and thus have high momenta according to Heisenberg's uncertainty principle, their interaction is coulombic and can be calculated by perturbative QCD (pQCD) [9]. However, when quarks are far away from each other and have lower momenta, the strong force potential is linear and cannot be fully predicted by analytic methods so far.

An alternative way is to compute non-perturbative QCD in purely numeric fashion by brute force. Lattice QCD (LQCD) does exactly that by placing the QCD Lagrangian on a discrete space-time lattice [10]. Unfortunately, the computing power required rises exponentially with smaller and smaller lattice intervals. To achieve a solution of demanded precision is still beyond reach of the current computing technology.

1.2. HADRON SPECTROSCOPY

Almost all of the visible universe is made of hadrons, which are particles made of quarks held together by gluons. But we still do not really understand how the binding works and what hadron's internal structures are. This is because the physics here is right in the regime of non-perturbative QCD. It is therefore necessary to have models to explain it.

1.2.1. Constituent Quark Models. The Constituent Quark Model (CQM) approach is very successful in explaining the hadron spectrum. Historically, CQM actually led the way to QCD [11]. There are a large number of hadrons discovered besides the lowest mass ones (p, n, π, K) and they all find their places in CQM.

In this approach, we have two types of hadrons: baryons made of three quarks and mesons made of a quark and an anti-quark. The properties of baryons and mesons come from quarks. For example, a quark has a baryon number of 1/3 and an anti-quark has $-1/3$, so each baryon has a baryon number of 1 and each meson has a baryon number of 0. Baryon number conservation observed by experiments can be simply translated into quark number conservation.

There are totally 6 different current (bare) quarks in QCD. Table 1.1 summarizes their properties. In CQM, the quarks are not basic particles like these current quarks. They carry the same quantum numbers, but their masses are much larger than their

TABLE 1.1. Properties of quarks [1]

Symbol	u	c	t
Name	Up	Charm	Top
Charge(e)	+2/3	+2/3	+2/3
Mass(MeV/c^2)	1.5-3.0	1250 ± 90	$1.725 \pm 0.023 \times 10^5$

Symbol	d	s	b
Name	Down	Strange	Bottom
Charge(e)	-1/3	-1/3	-1/3
Mass(MeV/c^2)	3-7	95 ± 25	4200 ± 70

current counterparts. They are called constituent quarks and are essentially gluon-dressed bare quarks. Therefore, the gluon degree of freedom is entirely hidden in CQM.

When the constituent quarks work as building blocks of hadrons, there are spatial, color, spin and flavor as quantum numbers. The ground-state wave functions should have only zero spatial component. The three colors are governed by $SU(3)_{color}$ group. For all of 6 quarks, the $SU(6)_{flavor}$ group dominates. But only $SU(3)_{flavor}$ is needed for the hadrons made of only three light quarks (u, d, and s). Adding the spin symmetry, $SU(6)_{flavor-spin} = SU(2)_{spin} \otimes SU(3)_{flavor}$ is the final symmetry if we ignore the color quantum number for now.

Because a ground state meson is made of a quark of spin 1/2 and an anti-quark of spin 1/2, its spin component can be 0 or 1. The flavor composition has nine states, $SU(3)_{quark} \otimes SU(3)_{antiquark} = 8 \oplus 1$. Therefore there are totally two nonets with different spins shown in Figure 1.1.

A similar situation happens again for ground state baryons which are made of three quarks. The total spin state can be 1/2 and 3/2 and the flavor decomposition is $SU(3) \otimes SU(3) \otimes SU(3) = 10 \oplus 8 \oplus 8 \oplus 1$. The octet with spin 1/2 and the decuplet with spin 3/2 are shown in Figure 1.2.

All these multiplets are showing the ground states of light hadrons that are explained by CQM. As composite particles, hadrons can have excited states due to their
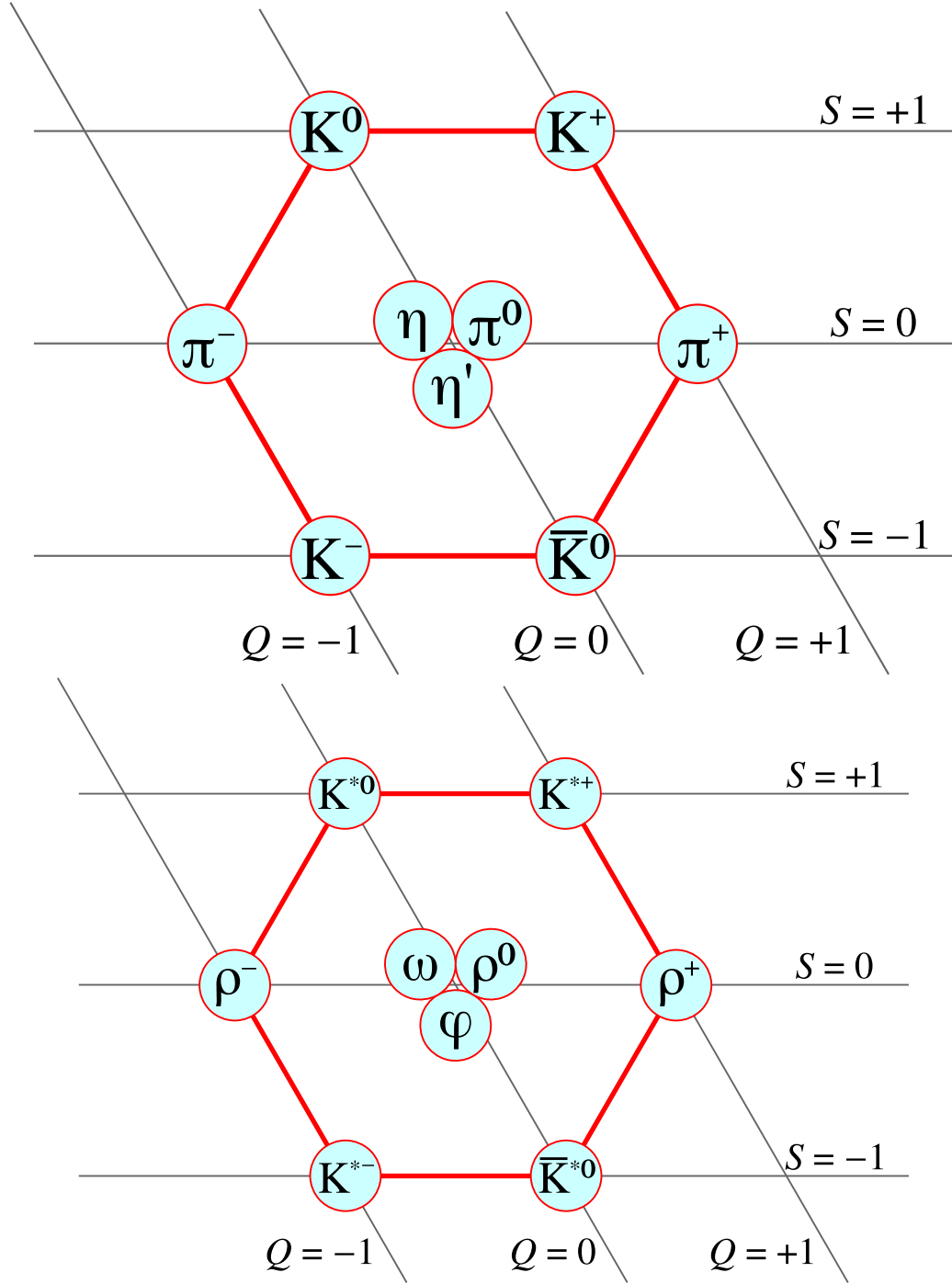
FIGURE 1.1. The pseudo-scalar and vector meson nonets

internal degrees of freedom. CQM has some successes and some failures in describing these excited states.

One example is shown here. Table 1.2 lists the predicted excited nucleon (p, n) states with resonance masses, angular momenta, and parities and compares them
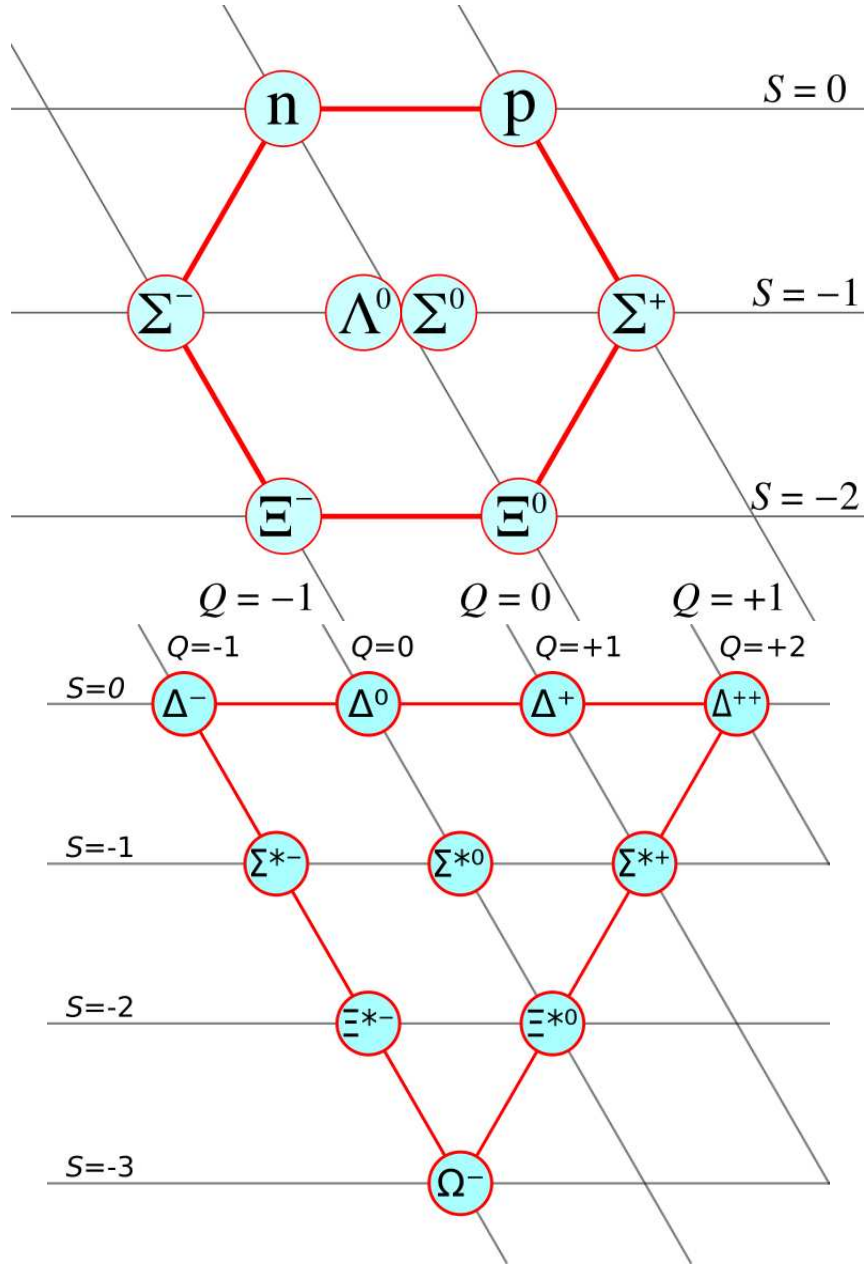
FIGURE 1.2. The baryon octet and decuplet

with experimentally found resonances, whose evidence is ranked by the number of stars. Some of predictions match well with the results of the experiments, but most of the predicted states are not found experimentally. They are often called "missing resonances". It could be that the prediction is wrong or that they are not found because most experiments used pion scattering off nucleons, and the missing states may not have strong coupling to πN reaction.

TABLE 1.2. N* spectrum predicted by the Constituent Quark Model [2].

J^P	M_{CQM}	M_{PDG}	Rating	J^P	M_{CQM}	M_{PDG}	Rating
$1/2^-$	1460	1535	****	$1/2^+$	1540	1440	****
$1/2^-$	1535	1650	****	$1/2^+$	1770	1710	***
$1/2^-$	1945	2090	*	$1/2^+$	1880		
$1/2^-$	2030			$1/2^+$	1975		
$1/2^-$	2070			$1/2^+$	2065	2100	*
$1/2^-$	2145			$1/2^+$	2210		
$1/2^-$	2195						
$3/2^-$	1495	1520	****	$3/2^+$	1795	1720	****
$3/2^-$	1625	1700	***	$3/2^+$	1870		
$3/2^-$	1960	2080	**	$3/2^+$	1910		
$3/2^-$	2055			$3/2^+$	1950		
$3/2^-$	2095			$3/2^+$	2030		
$3/2^-$	2165						
$3/2^-$	2180						
$5/2^-$	1630	1675	****	$5/2^+$	1770	1680	****
$5/2^-$	2080			$5/2^+$	1980	20000	**
$5/2^-$	2095	2200	**	$5/2^+$	1995		
$5/2^-$	2180						
$5/2^-$	2235						
$5/2^-$	2260						
$5/2^-$	2295						
$5/2^-$	2305						
$7/2^-$	2090	2190	****	$7/2^+$	2000	1990	**
$7/2^-$	2205			$7/2^+$	2390		
$7/2^-$	2255			$7/2^+$	2410		
$7/2^-$	2305			$7/2^+$	2455		
$7/2^-$	2355						
$9/2^-$	2215	2250	****	$9/2^+$	2345	2220	****
$11/2^-$	2600	2600	***				
$11/2^-$	2670						
$11/2^-$	2700						
$11/2^-$	2770						
$13/2^-$	2715						

1.2.2. Hyperon. One of the reasons to study hyperons (baryons with strangeness), is to see if any missing resonance has strong coupling to kaon-hyperon (KY) reactions [12]. But hyperons themselves are of great interest, not only because they lack experimental data due to their small cross sections, but also because their production mechanism may shed light on general baryon models with the SU(3) flavor symmetry broken by the relatively heavy strange quark.

Many hyperon photoproduction experiments have been carried out in recent years and more of them are under way. Some experiments focus on the complete measurement of the scattering amplitude by using a combination of linearly and circularly polarized photon beams, longitudinal and transverse polarized targets, and hyperon recoil polarization. Some experiments are looking for new resonances in Ξ range and even pentaquarks.

Pentaquarks have been a controversial topic since the Laser Electron Photon beamline at SPring-8 (LEPS) collaboration published their first result in 2003 [13]. The pentaquark Θ^+ is composed of 5 quark-antiquark with the exotic quantum number, strangeness $S = 1$, which cannot be explained in the traditional CQM with three quarks only. The reaction studied by LEPS is $\gamma d \to K^- K^+ pn$, where K^+ and n come from the pentaquark Θ^+ decay. Even though most of the recent pentaquark searches at other facilities gave null results, LEPS had new results confirming its previous discovery in 2009 [14]. For the same final state, there are two possible channels. One is $K^- K^+$ from $\phi(1020)$ decay and the other is $K^- p$ from $\Lambda^*(1520)$ decay. It is not easy to claim an exotic new resonance without a good understanding of these two resonances.

1.3. $\Lambda^*(1520)$ PRODUCTION

$\Lambda^*(1520)$ is an excited hyperon state with total spin $J = 3/2$, negative parity and strangeness $S = -1$. Its mass and width (15.6 MeV) are similar to the reported pentaquark $\Theta^+(1540)$. It is often the main background of the pentaquark production and thus can be used to check the normalization by comparing the known resonance $\Lambda^*(1520)$ to existing data. However, there are still few $\Lambda^*(1520)$ production studies published and its mechanism is not well understood due to the lack of experimental data.

1.3.1. Previous Studies of Cross Section. There are three $\Lambda^*(1520)$ electroproduction studies published. The Hall-A collaboration at the Thomas Jefferson

National Lab (JLab) has done a detailed study [15] on the mass and width of the resonance. One early electroproduction [16] studied the variation of the cross section at the virtual photon invariant mass squared Q^2 from 0.1 to 0.5 GeV^2. The latest cross section study [7] from the CLAS at JLab covered the kinematic region at the virtual photon invariant mass squared Q^2 from 0.9 to 2.4 GeV^2 and the total energy in center of mass frame W from 1.95 to 2.65 GeV. They all suggest t-channel dominant processes.

There are more photoproduction studies available. One early experiment [17] at Stanford Linear Accelerator Center (SLAC), used a 11 GeV photon beam on hydrogen to study the inclusive reaction $\gamma p \rightarrow K^+ Y$, where Y represents a produced hyperon. They reported $\Lambda^*(1520)$ cross sections at different K^+ scattering angles. Another early experiment on hydrogen [3] from the LAMP2 collaboration at Daresbury, studied the exclusive reaction $\gamma p \rightarrow K^+ \Lambda^*$ with $\Lambda^* \rightarrow pK^-$ at photon energies ranging from 2.8 GeV to 4.8 GeV. Both of them reported exponential t-dependent differential cross sections. The two latest experiments [6, 18] from the LEPS collaboration reported the same reaction from the near-threshold photon energies from 1.6 GeV to 2.4 GeV. As a forward angle detector, LEPS detects forward $K^- p$ (thus K^+ going backward) or forward K^+ and their results are shown in Figure 1.3 and Figure 1.4 respectively.

A series of theoretical papers have tried to study the $\Lambda^*(1520)$ photoproduction [4, 19, 5, 20]. The studies are based on an effective Lagrangian model with Regge contributions. The t-channel exchange particle propagators are employed in a gauge-invariant manner. The four relevant Feynman diagrams are shown in Figure 1.5. They include the nucleon-pole and nucleon-resonance contributions in the s-channel, the Λ-pole contribution in the u-channel, K and K^* exchanges in the t-channel, and the contact-term contribution [5].
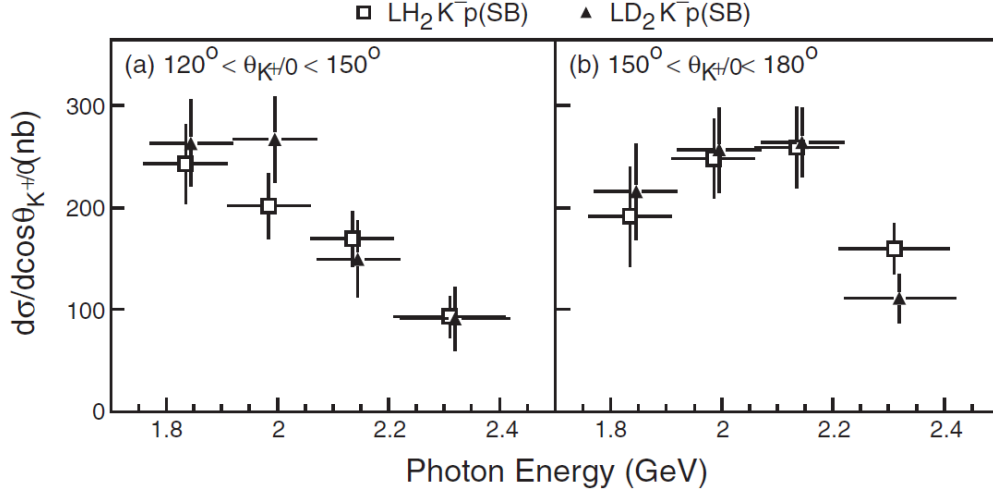
FIGURE 1.3. The differential cross sections from LEPS by detecting the forward K^-p, while backward K^+/K^0 t-channel meson stays undetected. Two angle bins for both reactions on hydrogen and deuterium showing very different distributions.

The model [4] is used to fit to the available cross section data of the production on protons, as shown in Figure 1.6. The fitting function describes the $\Lambda^*(1520)$ production on protons qualitatively well. According to the fit, the major part of the cross section is from the contact term, the t-channel term has second large contribution, and the s-channel and u-channel contributions are very small. After the parameters in the model are fixed by the fit, the prediction of the cross section on neutrons is made and it is one order of magnitude smaller than that on protons. This is because the contact term is absent in the neutron channel when no charge is present in all parties of the reaction.

The only published data for the photoproduction on neutrons can be found in Ref. [6]. They studied inclusive reaction by detecting only pK^- on both deuterium and hydrogen target and their differential cross sections are compared as shown in Figure 1.3. The cross section on neutrons can be estimated by evaluating the ratio of production from deuterons to that from protons, 1.02 ± 0.11. With limited statistics, the cross section on neutrons is two orders smaller than the cross section on protons at backward K^0 angles. The LEPS result supports the importance of the contact
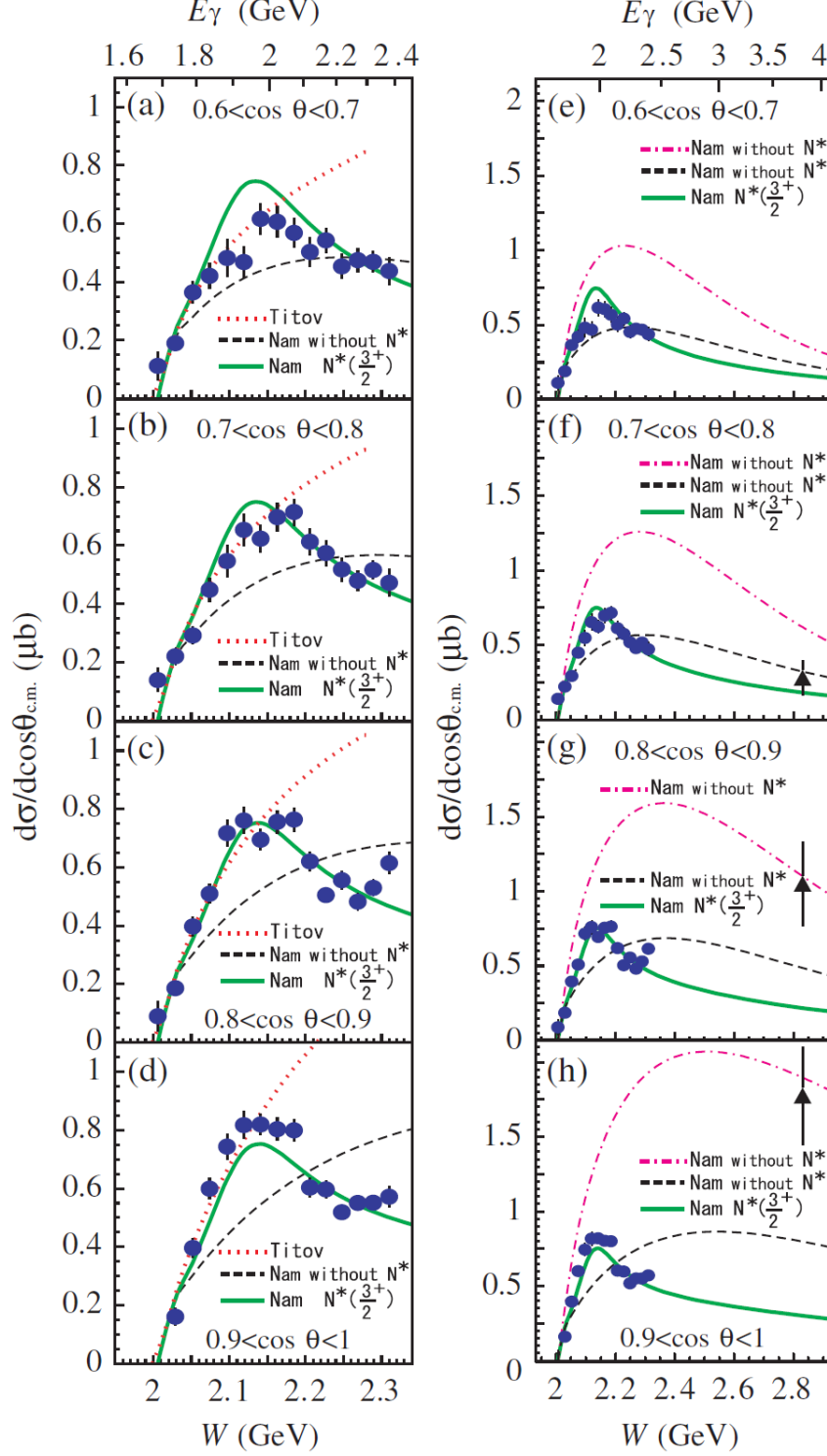
FIGURE 1.4. The differential cross sections on protons from LEPS by detecting forward angle K^+. The left plots are zoom-ins of the right plots. Four different angle bins are shown. A potential resonance structure is suggested at about $W = 2.1$ GeV and photon energy 2 GeV.
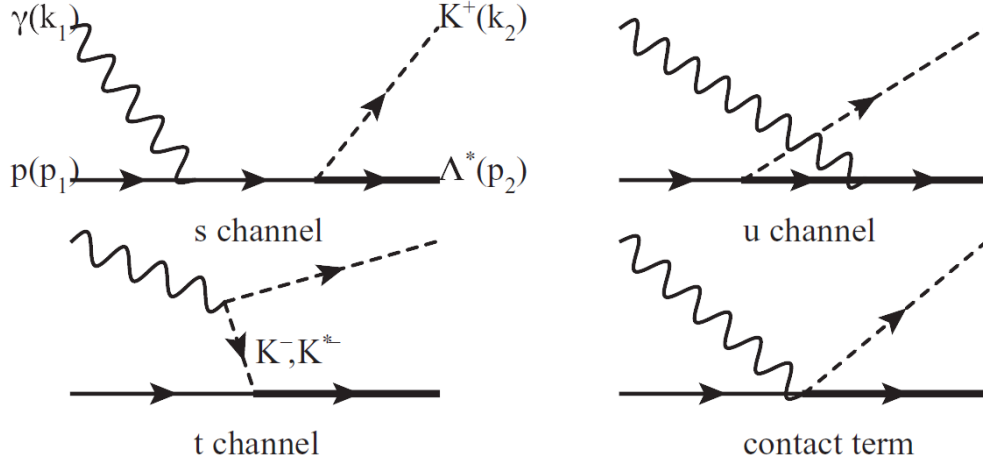
FIGURE 1.5. Four relevant Feynman diagrams of $\Lambda^*(1520)$ photoproduction.

Reactions	$\gamma p \to K^+ \Lambda^*$	$\gamma n \to K^0 \Lambda^*$
σ	$\sim 900\ nb$	$\sim 30\ nb$
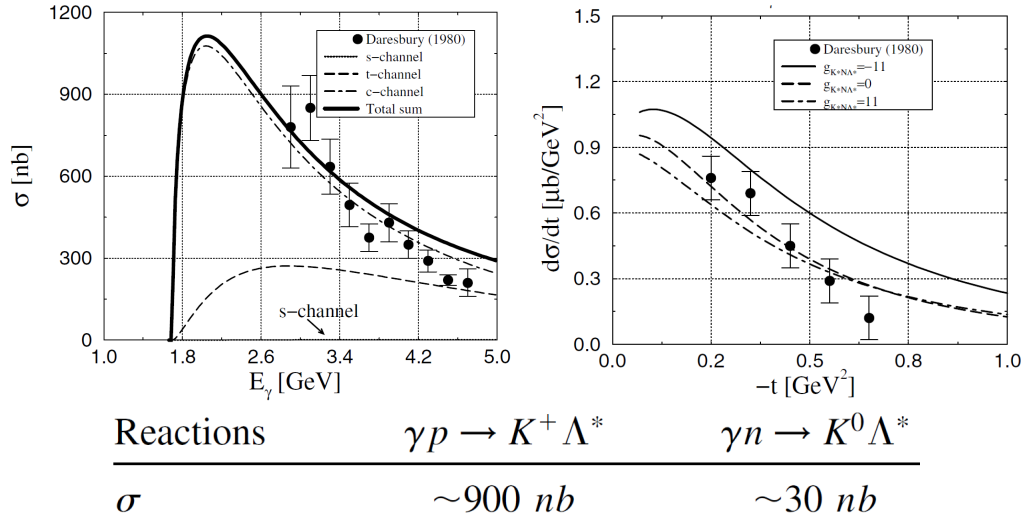
FIGURE 1.6. The total and differential cross sections for Λ^* photoproduction on protons from the studies of [3] fitted by the model by [4]. The same model predicts very different cross sections on protons and neutrons.

term which coexists with t-channel K exchange like what the theory has suggested [4].

1.3.2. Previous Studies of Decay Angle. $\Lambda^*(1520)$ has $J^p = 3/2^-$. Its strong NK decay channel, including pK^- and nK^0, conserves its parity. For $\Lambda^*(1520)$
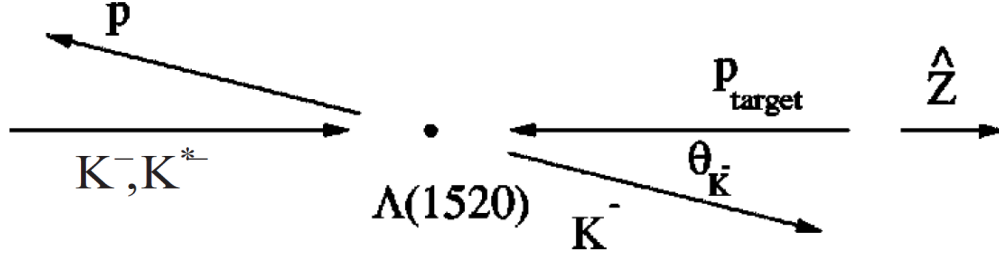
FIGURE 1.7. $\Lambda^*(1520)$ decay in the Gottfried-Jackson frame.

photoproduction on nucleons, taking angular momentum conservation and Clebsch-Gordon coefficients into account, it can be shown that for $\Lambda^*(1520)$ with $m_z = \pm 3/2$, the pK^- decay is characterized by a $sin^2\theta_{K^-}^{GJ} = 1 - cos^2\theta_{K^-}^{GJ}$ distribution and for $\Lambda^*(1520)$ with $m_z = \pm 1/2$, $1/3 + cos^2\theta_{K^-}^{GJ}$ [7]. As shown in Figure 1.7, the $\theta_{K^-}^{GJ}$ is the angle between K^- and the opposite direction of target nucleon in the Gottfried-Jackson frame (i.e.,t-channel helicity frame) where is the $\Lambda^*(1520)$ is at rest.

The physical reaction can be a mixture of the two distributions and the interference terms with odd powers of $cos\theta_{K^-}^{GJ}$ due to other neighboring $J = 1/2$ hyperons in the background. The overall distribution of $\Lambda^*(1520)$ decay angle can be represented by

$$f(\theta_{K^-}^{GJ}) = \alpha \left(\frac{1}{3} + cos^2\theta_{K^-}^{GJ} \right) + \beta \left(1 - cos^2\theta_{K^-}^{GJ} \right) + \gamma \left(cos\theta_{K^-}^{GJ} \right) \qquad (1.1)$$

where α, β, γ are the coefficients for $m_z = \pm 1/2, m_z = \pm 3/2$, and the interference term respectively.

The t-channel exchange particle can be a pseudo-scalar meson K with $J^p = 0^-$ and/or a vector meson K^* with $J^p = 1^-$. The target nucleon N has $J^p = 1/2^+$. If the t-channel exchange particle is a spinless K, the $\Lambda^*(1520)$ spin projection is $m_z = \pm 1/2$ and thus β and the β/α ratio are zero. On the other hand, if a vector K^* is the exclusive exchange particle, both $\Lambda^*(1520)$ spin projection $m_z = \pm 1/2$ and $m_z = \pm 3/2$ are possible and the β/α ratio is 3 if solely determined by Clebsch-Gordon coefficients. Any interference background will show up as a none-zero γ.
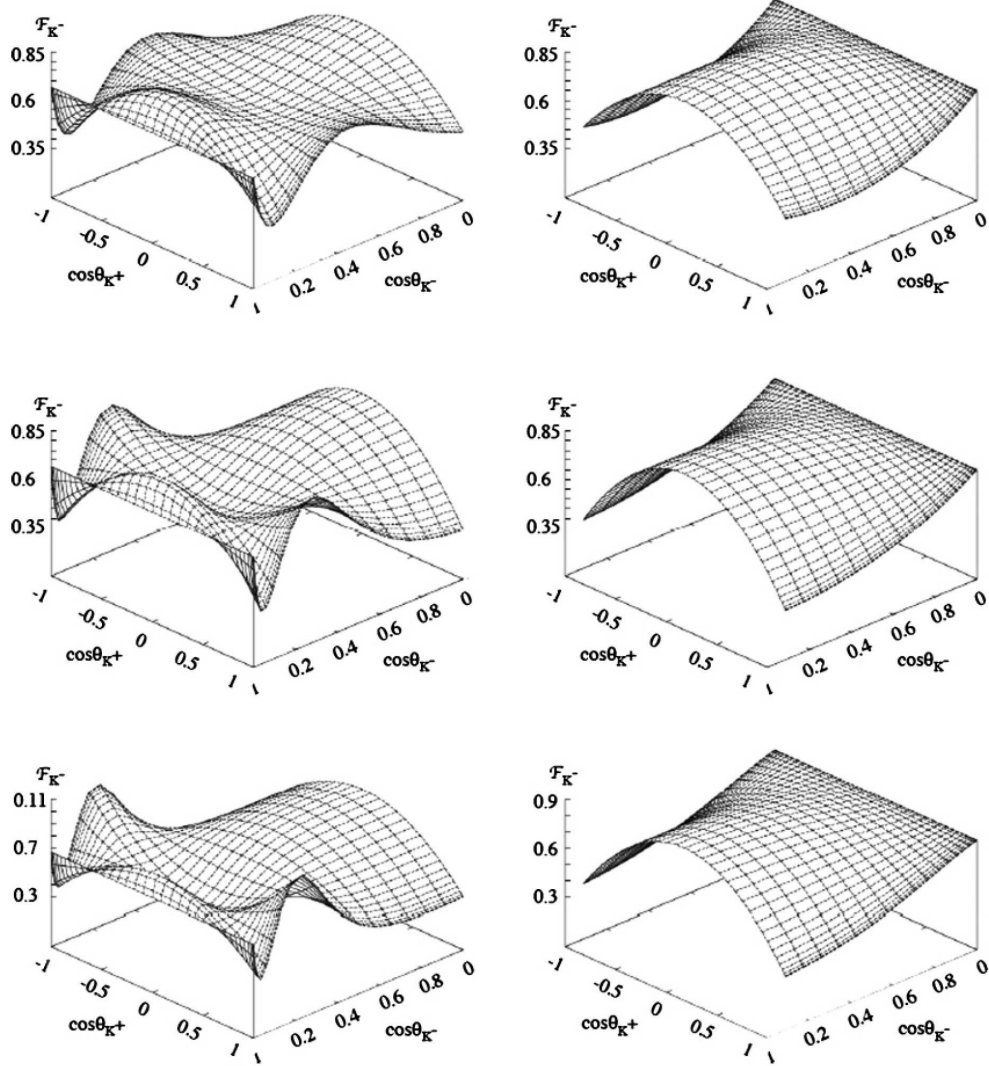
FIGURE 1.8. From [5], K^- angle distribution function F_{K^-} as a function of $cos\theta_{K^-}$ and $cos\theta_{K^+}$ for $E_{gamma} = 2.25$ GeV (first row), 3.25 GeV (second row), and 4.25 GeV (third row). The left column indicates the forward region $\theta = (0 - 90)°$, whereas the right column the backward region, $\theta = (90 - 180)°$. Here $\theta = \theta_{K^+}$.

A more detailed theoretical calculation for the reaction on protons has been carried out without the interference term in Ref. [5]. The function $F_{K^-} = \alpha \left(\frac{1}{3} + cos^2\theta_{K^-}^{GJ} \right) + \beta \left(1 - cos^2\theta_{K^-}^{GJ} \right)$ shows complicated dependence of E_{gamma}, $cos\theta_{K^-}$ and $cos\theta_{K^+}$ as shown in Figure 1.8. The shape of F_{K^-} greatly depends on the value of $cos\theta_{K^+}$ in the forward region, but is insensitive to that in the backward one.

13
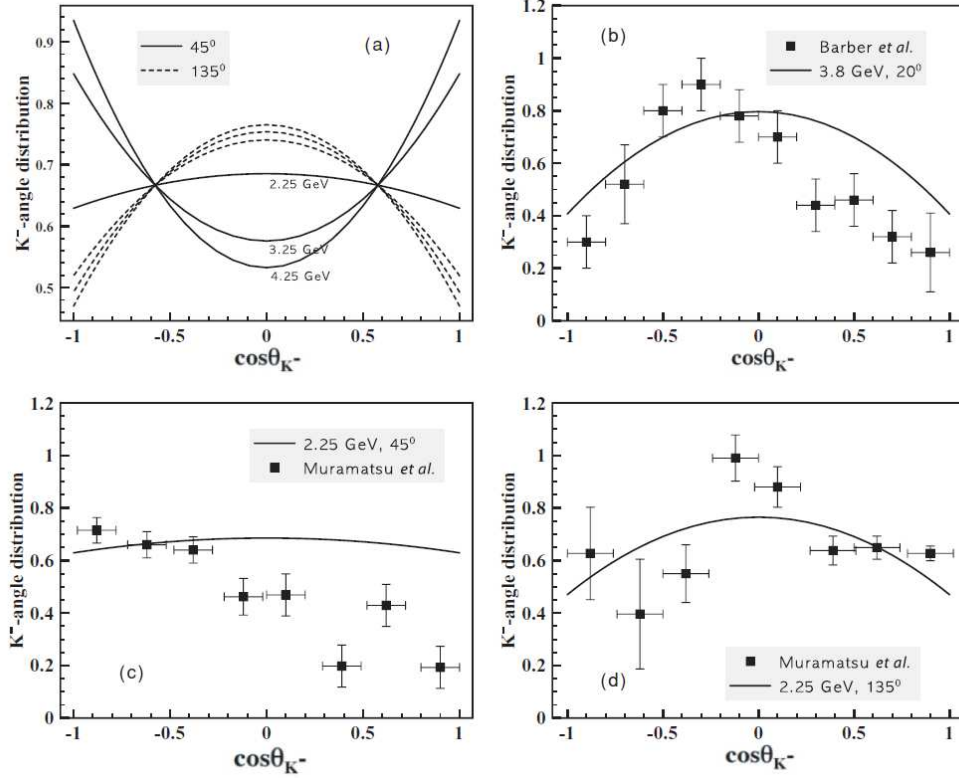
FIGURE 1.9. In (a), $F(\theta_{K^-}^{GJ})$ at different $E_\gamma = 2.25$, 3.25 and 4.25 GeV and t-channel K^+ center of mass angle $\theta_{K^+(CM)} = 45°$ and 135° from Ref. [5]. In (b), the comparison of the numerical result for $E_\gamma = 3.8$ GeV and $\theta_{K^+}^{CM} = 20°$ with the experimental data taken from Ref. [3]. Similarly, in (c) and (d) the comparisons at $E_\gamma = 2.25$ GeV and $\theta_{K^+}^{CM} = 45°$ and 135° respectively with the data taken from Ref. [6]

Some sample projections of the two dimension distributions are shown in (a) of Figure 1.9. (b),(c), and (d) of Figure 1.9 show the comparison between the numerical calculations and the data of LAMP2 at the forward K^+ angle [3] and LEPS at the forward and backward K^+ angles [6]. The numerical calculation can describe the data qualitatively except that the LEPS data at the forward K^+ angle may need some interference term to be taken into account.

Even though the available data from several photoproduction experiments favor a vector meson K^*-exchange-dominance model. However, the data from the electro-production [7] is more likely dominated by a spinless meson K-exchange process as shown in Figure 1.10.
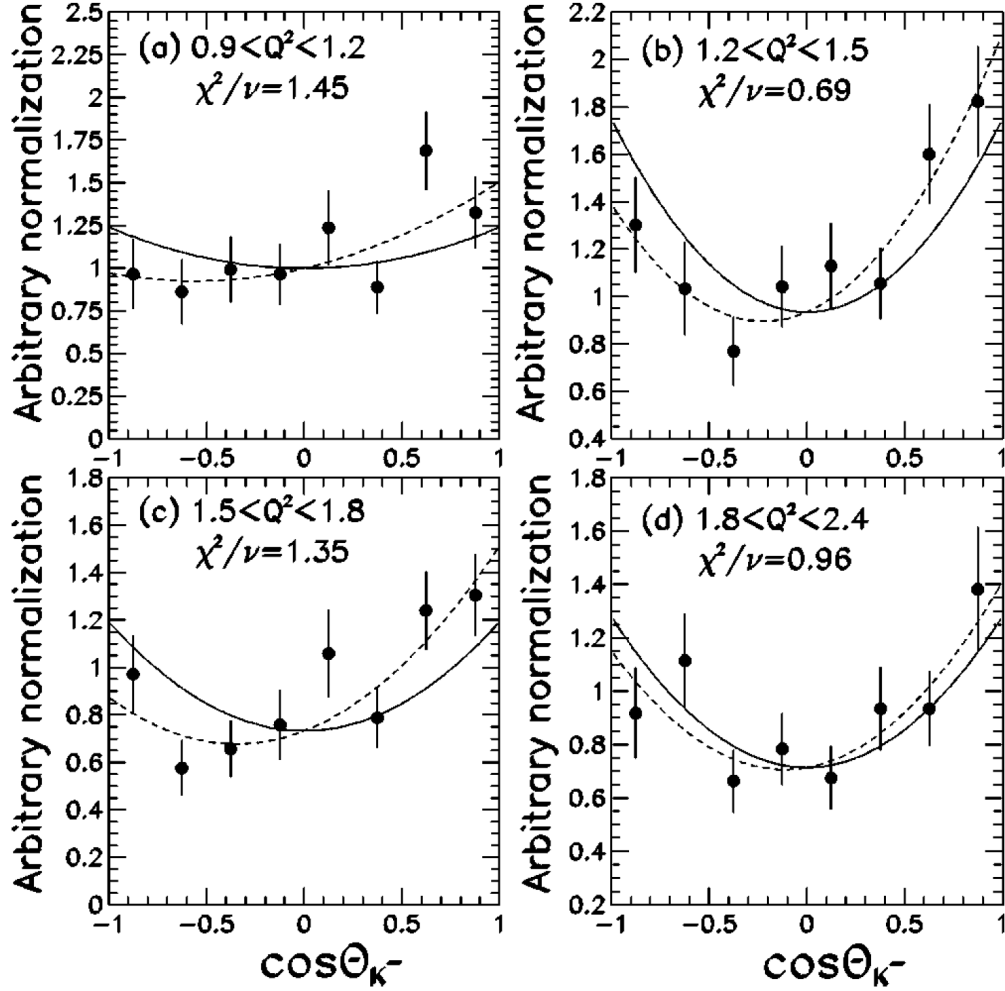
FIGURE 1.10. The decay angle distribution of $\Lambda^*(1520)$ at different Q^2 from the electroproduction study [7]. They are averaged over the region of W from threshold to 2.43 GeV. The dashed lines are the fitting results with the interference term and the solid lines are the fitting results without it.

1.3.3. The Subject of this Study. To better measure the cross section and decay angular distribution of the $\Lambda^*(1520)$, and therefore provide constraints on the model predictions and insights into the production mechanism, we have studied the photoproduction of $\Lambda^*(1520)$ off both the proton and neutron in the deuteron by using the CLAS eg3 run data set. The reactions we analyzed are

1. (**Proton Channel**), $\gamma d \to K^+ \Lambda^*(n)$ with $\Lambda^* \to pK^-$.

2. (**Neutron Channel**), $\gamma d \to K^0 \Lambda^*(p)$ with $\Lambda^* \to pK^-$ and $K^0 \to K_s \to \pi^+\pi^-$.

15

Both channels are identified exclusively by tagging the incident γ and detecting pK^+K^- or $p\pi^+\pi^-K^-$ respectively. The missing nucleons are identified by the missing mass technique. Missing momentum cut is used to enrich quasi-free reactions.

The photon energy range covered in this study is 1.75 GeV $< E_\gamma <$ 5.50 GeV, which is the largest energy coverage up to date. Cross sections and decay angle distributions are studied at various kinematic bins. The proton channel results are compared to those published for the free proton target (hydrogen). We also present the first exclusive measurement of the neutron channel.

Chapter 2

Experiment

2.1. Jefferson Lab

The experiment was carried out in Hall B at Thomas Jefferson National Accelerator Facility (TJNAF), also known as Jefferson Laboratory or JLab, in Newport News, Virginia, USA. A picture of the facility is shown in Figure 2.1. At the lab, the Continuous Electron Beam Accelerator Facility (CEBAF) can deliver a high-intensity electron beam to three experimental halls A, B, and C simultaneously with mostly independent beam parameters. A schematic layout is shown in Figure 2.2. All halls have fixed targets. Hall A and Hall C have fixed-angle detectors dedicated for hadrons and electrons separately, whereas Hall B has a spherical detector of large acceptance covering almost 4π solid angle to detect multiple particles.

2.2. CEBAF

CEBAF uses superconducting radio frequency (SRF) niobium cavities (Figure 2.3) instead of traditional copper cavities to minimize heat accumulation by cavity material electric resistance and thus improves the acceleration gradient. This technical advancement makes it possible to deliver "continuous", high-energy, and high-intensity electron beams.

At the injector, electrons are generated by shining a pulsed laser on a GaAs photocathode every 2.004ns. Then they are accelerated to 45MeV by going through two and a quarter SRF cavities before being recirculated through the linear accelerators (LINACs) of CEBAF.

FIGURE 2.1. Thomas Jefferson National Accelerator Facility.
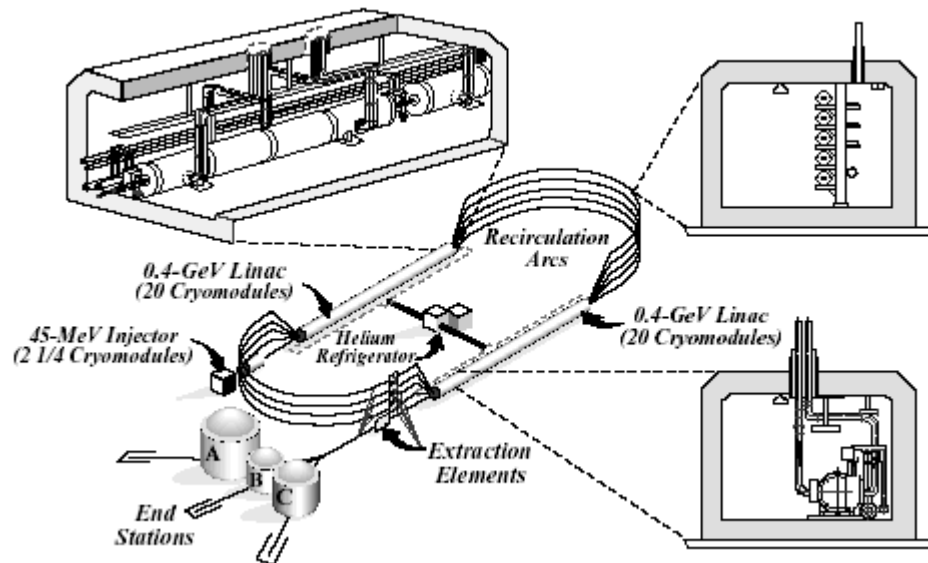
FIGURE 2.2. Layout of Thomas Jefferson National Accelerator Facility, showing injector, linear accelerators, recirculation arcs and three halls.
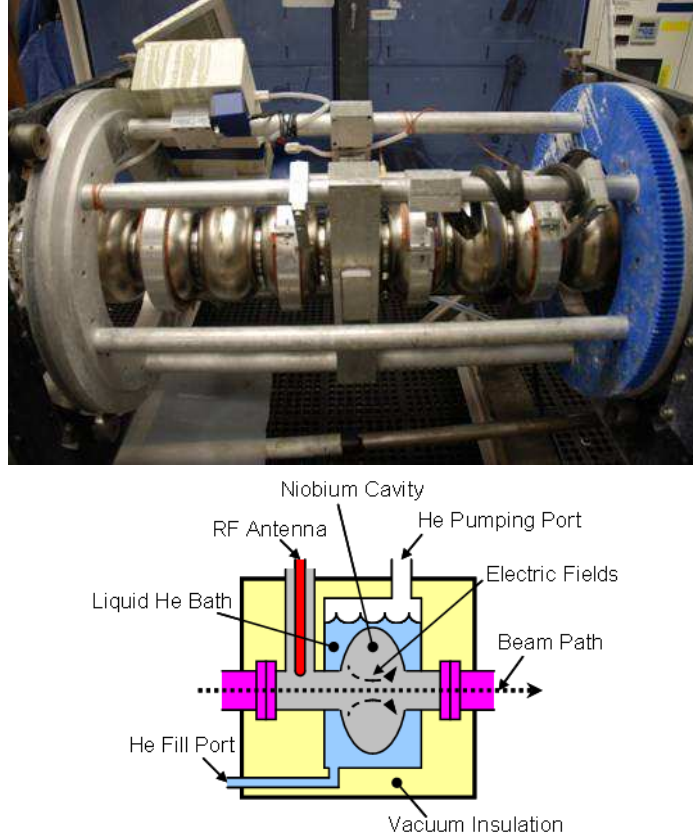
FIGURE 2.3. Picture of CEBAF's SRF cavities and the illustration of how it works inside.

There are two LINACs, and each LINAC has 168 SRF cavities. The cavity temperature is at 2K using liquid helium to maintain its superconducting state. In the cavities, the acceleration of the electron beam by RF electromagnetic standing waves does not depend on the speed of electrons once they have reached the 45 MeV provided by the injector and hence close to the speed of light.

It's counted as one pass for an electron to go through both LINACs after bending by the recirculation arcs. Each LINAC can accelerate electrons by 600 MeV. After one pass, the electrons gain 1.2 GeV. Currently CEBAF can operate at up to 5 passes so electron beam energies can reach 6 GeV before delivery to each experimental hall by extraction elements. The acceleration process was carefully designed to focus electrons into beam buckets, and each bunch has a width of only several picoseconds.

FIGURE 2.4. A picture of CLAS. The drift chamber detectors (DC) are still closed inside, and the time-of-flight detectors (TOF) are opened up and peeled away.

2.3. THE CLAS DETECTOR

The CEBAF Large Acceptance Spectrometer (CLAS) is a spherical, multiple-component detector system as shown in Figure 2.4. It detects charged and neutral particles produced by the interaction of electrons or bremsstrahlung photons with a cryogenic target placed in the beam path near the center of CLAS. For a detailed description of the detector, please refer to Ref. [21].

2.3.1. Main Detector Components. The main components of CLAS include a superconducting torus magnet(Torus), drift chambers (DC), Cerenkov counters (CC), time-of-flight scintillators (TOF or SC), electromagnetic calorimeters (EC) and start counters (ST). An illustration of the main components and a cut view are shown in Figure 2.5.

As near 4π detector, CLAS has each of its components split in 6 sectors as shown in Figure 2.6.

20
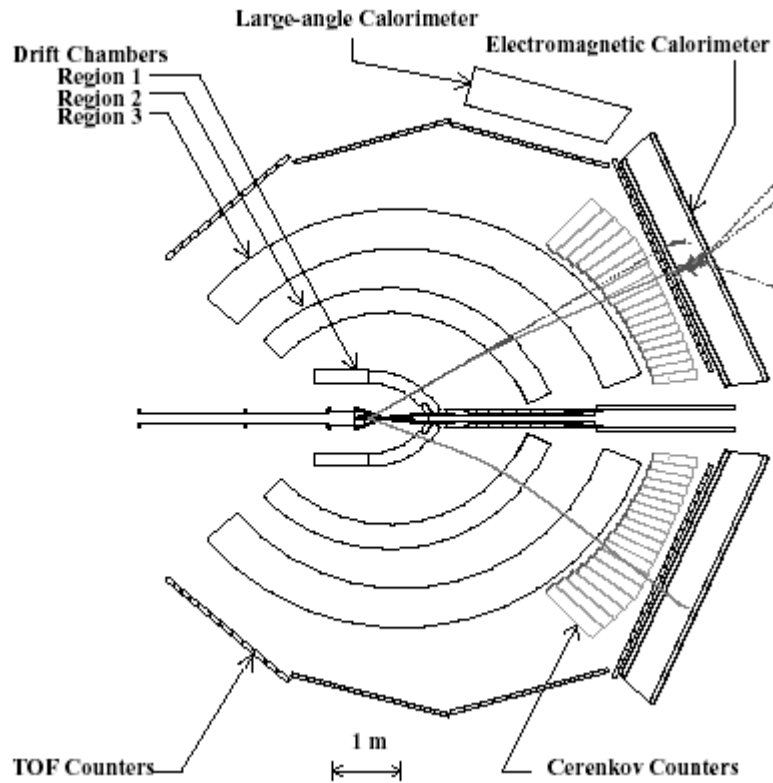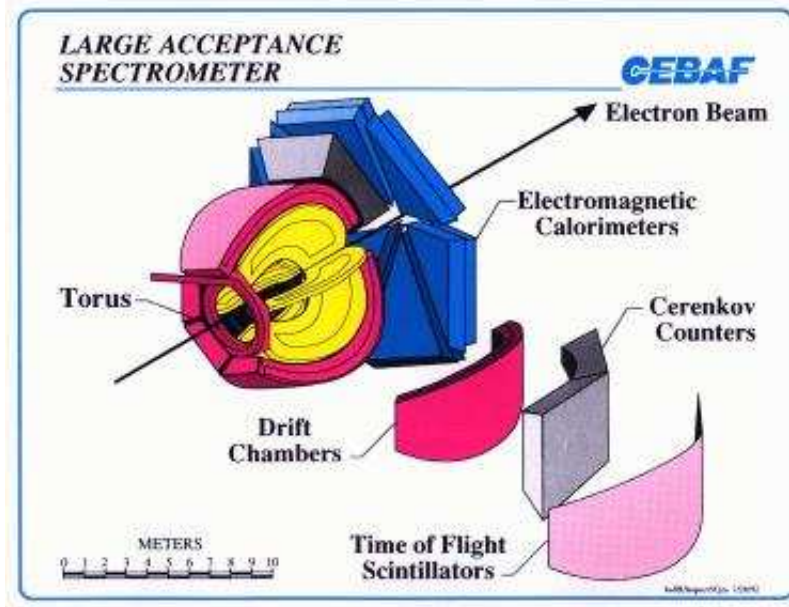
FIGURE 2.5. Illustration of CLAS and its subsystems and a cut view of the CLAS detector. A sample trajectories are shown too.

To detect charged particles like p, e, π, K, first their trajectories are bent in the torus magnetic field and detected by DC via ionization processes. Then TOF and EC
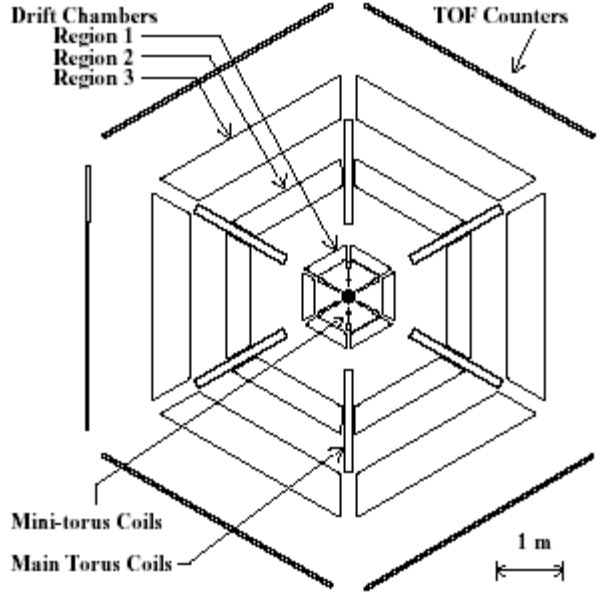
FIGURE 2.6. Azimuthal view of the CLAS detector. The six sectors are shown.

both record the time and energy deposition when charged particles reaches them. The charge type and the momentum of a particle can be derived from its path curvature in DC. Combining its TOF timing (the most precise time of all detector components), the event start time, its flight path calculated from the path in DC and its position information, we can derive the speed of a charged particle. From the speed and momentum, we can calculate its rest mass, which is a distinctive character of final particles in CLAS and essential for particle identification. TOF and EC also have particle energy deposition information to aid particle identification and physical analysis. CC is only used in electroproduction experiments to provide e/π separation. ST is made of scintillator bars around the target cell and only used in photoproduction experiments as part of the trigger system when no electron is present.

Unlike the charged particles, neutral particles like photon γ and neutron n, do not bend in the torus magnetic field. Therefore, there is no direct momentum detection. The speed of a neutral particle can be obtained only from the TOF timing, the event start time, and its position information as its trajectory is simple straight line. γ has
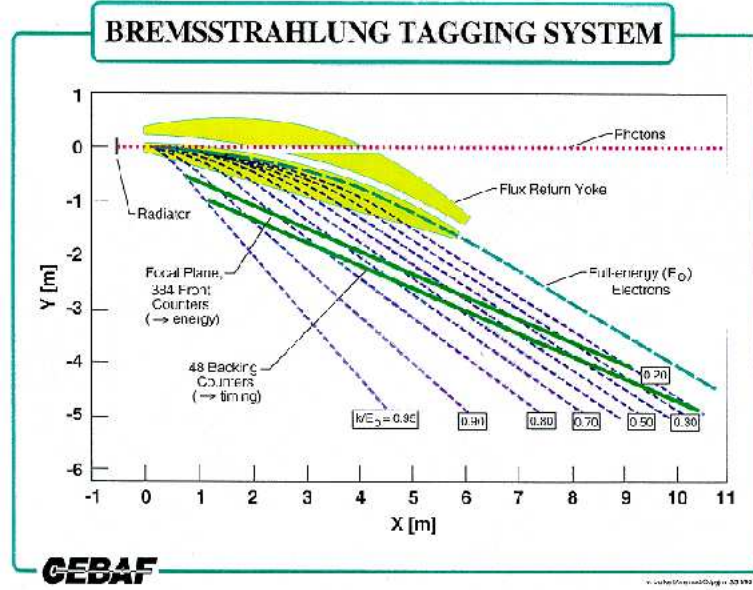
FIGURE 2.7. The schematic diagram of the tagger system in Hall B. The purple dashed line shows the trajectory of photons generated by bremsstrahlung of the electron beam. The cyan dashed lines are paths followed by recoil electrons. Each path corresponds to a fixed momentum of the recoil electrons.

the speed of light and the speed of a n is much lower than speed of light. The form of the energy deposition in EC is an electromagnetic shower for γ in contrast to an hadronic charge exchange reaction for n. Combining the speed and energy deposition, we can distinguish them from each other.

2.3.2. Photon Tagger. In electroproduction experiments, the electron beam directly hit the target. In photoproduction experiments, a bremsstrahlung photon beam is generated by putting a gold foil radiator in the electron beam path [22]. After electrons pass through the radiator, the beam contains primary electrons, recoil electrons and radiated photons. A dipole magnetic field bends all of the electrons out of the beam line, and the photons continue to travel towards the target. The primary electrons are bent into the beam dump, and the recoil electrons are bent on a photon tagger system (Tagger) as shown in Figure 2.7.

The tagger is made of two arrays of scintillation detectors. One set of them, called E-counters, is used to mark the momenta and hence energies of the recoil electrons

simply by the E-counters positions, because the path of electrons in a magnetic field is solely determined by their momenta. There are 384 physical E-counters overlapping with neighboring ones to improve the resolution of electron momenta without increasing the number of scintillators. The total number of logical energy channels becomes 767, rather than 384. The tagging system can detect recoil electrons that correspond to photons ranging from 20% to 95% of the incident electron beam energy. Therefore, the energy resolution of each logical energy channel is about 0.1% of the incident electron beam energy.

The other array of the tagging scintillation detectors, called T-counters, is used to measure the time when the recoil electrons reach them. There are 61 physical T-counters and every T-counter has two photomultipliers (PMT) on each end so the total logic channels are 122. The signals from the T-counters are sent to the Master OR (MOR) and an array of FASTBUS time-to-digital converters (TDC) after passing through discriminators. The TDC array digitizes the photon timing, and the MOR signal can be part of the trigger system for photon runs. The E-counter signals are also sent through a discriminator and then forwarded to a multi-hit TDC. The timing information of both E-counters and T-counters is sent to the data stream. The timing coincidence between them is required for good entries in Tagger.

The most accurate timing signal in CLAS is from the accelerator RF signals. For electron runs, incident electrons can be directly related to RF and used for event start time. For photon runs, the photon time from Tagger is used to find from which beam bunch the recoil electron comes. Then the photon tagger time is synchronized to the RF signals and corrected to the time when the photon reaches the target center in order to serve as the event start time.

2.3.3. Triggering and Data Acquisition. To filter out electronic noise and pick only events of interest, a trigger system is necessary. CLAS has a two level trigger system. The Level-1 trigger can use some or all of the fast information from the TOF, CC, EC, ST, and Tagger. The Level-2 trigger requires additional tracking

information in DC. Only after trigger conditions are satisfied, the data acquisition system (DAQ) will collect the digitized data and send the information to storage media for later off-line analysis.

2.4. EG3 EXPERIMENT

2.4.1. Running Condition. The eg3 experiment or so called eg3 run, where eg3 is the experiment name used within CLAS collaboration, was carried out from December 6th, 2004 to February 1st, 2005 in Hall-B JLab. The electrons were accelerated up 5.7655 GeV in the CEBAF superconductor LINACs and passed through a radiator with a nominal thickness of 5×10^4 radiation length. The recoil electrons were bent into the photon tagging system, where the electron energy was measured. The photon beam from the radiator impinged upon a 40 cm long and 4 cm diameter liquid deuterium target positioned 50 cm upstream of the nominal CLAS center.

For most of the running time, the electron beam current was chosen to be 30 nA, which was limited by the drift chamber performance. The CLAS tagging system tags bremsstrahlung photons with energies ranging from 20% to 95% of the incoming electron energy, which is about 1.15 - 5.50 GeV for eg3. Even though eg3 only triggered on 4.5 - 5.5 GeV, because the experiment was designed to optimize the detection of a possible pentaquark $\Phi^{--}(1862)$ at high energies [23], the photons with energies 1.15 - 4.50 GeV were also recorded as accidentals within the trigger time window.

There were two Level-1 trigger configurations selected as trigger bit 5 and 6. Trigger bit 5 is set as a two track trigger requiring a coincidence in the TOF system and the start counter ST in the same sector for at least two sectors: $(TOF \times ST)^2$. Trigger bit 6 is a three track trigger requiring TOF and ST coincidences for at least three sectors: $(TOF \times ST)^3$. The bit 5 trigger was prescaled with a factor, which varied from run to run to allow for less than 20% DAQ deadtime. The bit 6 trigger is not prescaled. The Level-1 trigger is in coincidence with the Master OR signal

from the photon tagger. For a large portion of the experiment the Master OR also is passed through a coincidence with the start counter before going into the trigger supervisor in order to reduce the trigger background. This experiment did not use the Level-2 trigger capability of CLAS.

For the normal CLAS torus magnetic field, positive charged particles are bent outwards away from the beam line and thus have better detection coverage at forward angles. eg3 used the inverted field to optimize forward negative charged particle detection. The torus magnet current was chosen to be 1980 A which is about half of the peak current 3861 A. This is to optimize the detection in the eg3 kinematic range, because high energetic particles require high fields to have sufficient resolution while stronger fields may bend low energetic particles too much to be detected.

For 29 days of production on LD2 target, the eg3 experiment collected about 4.2 billion physical events, 32 TB of raw data with an average 2.7 tracks per event.

2.4.2. Calibration and Cooking. All of the CLAS detector components have to be carefully calibrated for every run period to make sure the recorded electronic signals can be used to derive meaningful physical observables with reasonable resolutions. A database called CALDB is used to store calibration constants for all CLAS runs. In particular, the set of calibration constants and its corresponding run period is linked by a database table "run index". This gives the flexibility that one can test different sets of constants for different runs.

Once the calibration constants for eg3 are in place, the eg3 data is processed with the standard CLAS "cooking" software package user_ana [24]. It translates electronic signals into physical variables like time, position, energy, momentum, direction, etc. and furthermore combines and interprets them as individual particles from physical reaction events passing through the CLAS detector by the hit-based and time-based tracking algorithms. The default run index "Runindex" is used for eg3 cooking.

Calibration and cooking are like chickens and eggs. They depend on each other to be carried out. It is often a good starting point to use the calibration constant

TABLE 2.1. eg3 Good Runs

Run Range	Beam Current (nA)	Bit 5 prescale	ASYNCH
45548-45556	30	20+1	T1-19
45558-45563	30	20+1	ST*T1-19
45568-45609	30	20+1	T1-19
45612-45614	5	0+1	T1-19
45621-45626	30	20+1	T1-19
45627	30	20+1	ST*T1-19
45804	10	20+1	ST*T1-19
45807-45811	35	20+1	ST*T1-19
45812-45852	30	20+1	ST*T1-19
45859-45937	30	5+1	ST*T1-19
45942-45943	10	1+1	ST*T1-34
45948-45975	30	5+1	ST*T1-19
45976-46113	30	4+1	ST*T1-19

set from the previous run period to do the initial cooking because that is when the detector and electronic equipment status were most closely related. Then after several iterations, a final set of constants are obtained and a final version of cooked data is ready to be used for the physics analysis.

2.4.3. Golden Run List. We usually call a CLAS experiment a run. For example, the eg3 experiment is called eg3 run. It's often a better description because a run or a run period sometimes represents more than one physical experiment. The data taking in CLAS is grouped into runs. Not to be confused with a so called run period, here a run is a continuous data taking process. An experiment operator will end a run once it reaches a certain number of events recorded by DAQ (say 30 M for a eg3 run) or when something goes wrong in the data taking. The purpose of this practice is to split the whole data set into smaller pieces, so that any software or hardware data taking problem can be easily isolated.

For the eg3 run period, 190 good runs without any data taking problem can be used for data analysis. Table 2.1 shows the running condition of these runs. A total of 179 of those runs have beam currents set to 30 nA. We could use good runs

with different beam currents for data analysis, because the photon flux and luminosity calculation will take this difference automatically into account (see Section 6.2). However the CLAS trigger efficiency has a beam current dependency. To simplify the analysis procedure, we eliminate the 6 runs with 5 nA and 10 nA because their trigger efficiency corrections would be very different from those runs with a beam current of 30 nA (see Section 4.9). We keep 5 runs with beam current of 35 nA because their trigger efficiency corrections within error bars are similar to those runs of 30 nA beam currents. Finally, a total of 184 runs are listed in the golden run list and used for data analysis. Here is the list: 45552, 45553, 45554, 45555, 45556, 45557, 45558, 45563, 45566, 45568, 45569, 45570, 45571, 45572, 45576, 45577, 45578, 45579, 45580, 45581, 45582, 45598, 45599, 45600, 45601, 45602, 45603, 45605, 45606, 45607, 45608, 45609, 45621, 45622, 45623, 45624, 45625, 45626, 45627, 45807, 45808, 45809, 45810, 45811, 45812, 45814, 45815, 45816, 45817, 45818, 45847, 45848, 45851, 45852, 45860, 45862, 45863, 45864, 45866, 45868, 45869, 45870, 45872, 45873, 45874, 45876, 45891, 45893, 45894, 45895, 45896, 45897, 45902, 45903, 45904, 45905, 45906, 45907, 45911, 45912, 45913, 45914, 45916, 45917, 45918, 45919, 45920, 45921, 45922, 45923, 45924, 45925, 45926, 45927, 45928, 45929, 45930, 45931, 45932, 45933, 45934, 45935, 45936, 45937, 45938, 45939, 45944, 45945, 45946, 45947, 45948, 45976, 45977, 45978, 45981, 45983, 45984, 45985, 45986, 45987, 45988, 45993, 45995, 45996, 46000, 46001, 46002, 46003, 46004, 46005, 46009, 46011, 46012, 46013, 46014, 46015, 46016, 46017, 46018, 46019, 46020, 46021, 46022, 46023, 46024, 46025, 46028, 46029, 46030, 46035, 46036, 46037, 46038, 46046, 46047, 46057, 46058, 46062, 46063, 46064, 46065, 46066, 46069, 46071, 46072, 46073, 46074, 46077, 46078, 46085, 46086, 46087, 46088, 46089, 46093, 46094, 46096, 46097, 46098, 46099, 46100, 46101, 46104, 46113.

CHAPTER 3

SIMULATION

When an experiment is completed, we only have final state particles as measured by our detectors. To find out how physical reactions have taken place when the beam hits the target, we need to know how our detector behaves. A computer Monte Carlo simulation is the best approach to do so. The step-by-step procedure is described below.

3.1. EVENT GENERATOR

First the physical reactions are generated by the event generator, FSGEN [25], which uses a t-slope adapted phase space distributions and contains Fermi-motion smearing for the spectator nucleon. The reaction $\gamma d \to K^+ \Lambda^*(n)$ with $\Lambda^* \to pK^-$ is generated with final particles $pK^+K^-(n)$ and the reaction $\gamma d \to K^0 \Lambda^*(p)$ with $\Lambda^* \to pK^-$ and $K^0 \to K_s \to \pi^+\pi^-$, is generated with final particles $p\pi^+\pi^-K^-(p)$. The advantage of letting all particles decay in the event generator is, that we only need to process the events of interest and thus save a lot of computing time. The choice affects what branching ratios are used in later cross section calculation (see Section6.3).

To extract cross sections correctly, it is best to simulate kinematic distributions that match the measured distributions of the real experiment. For the two reactions that we studied, only two independent kinematic variables are needed according to momentum and energy conservations to describe the kinematics completely. An obvious choice of two variables is E_γ and $t^* = -(t - t_0)$ where $t = (p_\gamma - p_{K^+/K^0})^2$ is the Lorentz-invariant four momentum transfer from photon to K^+/K^0 and t_0 is the

29

minimum of absolute value of the t [1]. Thus in simulation, to match the eg3 run conditions, the bremsstrahlung photon energy is set to 1.5 GeV - 5.5 GeV, and a constant t-slope $\beta = 2 GeV^{-2}$ is chosen after a couple iterations confirming that the differential cross section distribution over t^* shows an exponential behavior (a typical t-channel reaction characteristic) with an average slope of the same value. The $\Lambda^* \to pK^-$ and $K^0 \to K_s \to \pi^+\pi^-$ decays are simulated with homogeneous phase space distributions.

3.2. SIMULATION OF CLAS

After the reactions are generated, every event passes through GSIM [26], the standard Monte Carlo simulation package for the CLAS detector, which is based on the simulation frame work GEANT3 package from CERN. Generated particles fly into simulated CLAS detector components and simulated digital output are collected just like in a real experiment. There are several things that need to be noted here.

1. Energy losses are simulated when particles pass through material. Thus energy loss corrections need to be applied just like for the experimental data.

2. The photon tagger is not simulated. The photon energy information comes directly from the event generator filling E-counter and T-counter entries accordingly.

3. The eg3 trigger condition is not simulated. The trigger condition will be applied to the simulated data later in the analysis process (see Section 4.10).

4. The inefficiency and resolution of detector components are not fully simulated. They will be compensated for in the next step.

3.3. POST SIMULATION PROCESSING

The standard CLAS post-simulation processing package, GPP [27] is used in this step. It smears SC and DC values and applies a DC wire efficiency correction in order to mimic the actual CLAS detectors. Most of SC counters have very high efficiency (i.e. close to 100%), so SC efficiency correction is not implemented in GPP. Only some

problematic SC channels are identified by comparing the real data and the simulation data and they are cut away in both data sets (see Section 4.6).

3.4. Cooking and Analysis

The simulated data is cooked using the same version of user_ana [24] with the same configuration as the experimental data. However, the cooking of simulated data does not need all the calibration constants from the real data because the GSIM uses perfect detectors to simulate CLAS. The only things it needs to know are the target and start counter geometry configuration in the calibration database. So a special runindex "calib_user.RunindexEG3Sim" is used for the cooking.

After final reconstruction of the simulated data, the same analysis code that is used for the experimental data, is executed on the simulated data. Then acceptance is calculated as the ratio of the number of reconstructed events over the number of generated events in all analyzed kinematic bins.

Chapter 4

Corrections and Cuts

There are a series of corrections and cuts that must be applied to the experimental and/or simulated data before we can proceed to the event selection of the two physical reaction channels of interest.

4.1. Beam Trip Cut

The electron beam is intended to be delivered at a constant current. However, due to CEBAF running condition, the beam can have bursts and trips from time to time. The events collected by DAQ are sent to scaler readouts to monitor the beam condition. Any event from an unstable beam interval is cut away.

4.2. Energy Loss Correction

When product particles from the photon and liquid deuterium interaction pass through any materials like target materials, start counter scintillators and an air gap (up to the drift chambers), they may lose part of the energy due to ionization. The amount of energy loss depends on the charge and the velocity of the particle as well as the type and amount of the material it traverses. In order to account for these effects, energy loss corrections are applied to all particles using to Eloss software package [28].

4.3. Momentum Correction

Even after energy loss corrections are performed, systematic shifts still remain in the particle momentum determination by CLAS using the standard reconstruction software. These shifts can be due to the misalignment of the torus magnet with

respect to the CLAS drift chambers, energy loss of particles in the drift chamber regions not accounted for in the Eloss package, or software and calibration shortcomings. These shifts in the momentum determination can lead to shifts of the masses of detected or missing particles and widening of their mass peaks. To determine these shifts in the reconstruction of track momenta, the exclusive $\gamma d \rightarrow pp\pi^-$ reaction was kinematic fitted requiring four-momentum conservation [29]. The resulting momentum corrections were applied to only the experimental data, not the simulated data. They are as small as 10 MeV or less even for low momentum charged particles in the eg3 data and they do not affect any related resolution much.

4.4. Photon Energy Correction

Due to gravity, there is slightly a sag in the tagger scintillator paddles and thus a mismatch between the energy of a deflected electron and the paddle it hits. A correction has be included in the calibration database and applied during cooking [30, 29].

During the study of $\gamma d \rightarrow pp\pi^-$ reaction, it was discovered that the reconstructed eg3 photon energy has been too low by 7.71 MeV [29]. It is likely that the magnetic field strength in the tagger has been underestimated. This would again cause an energy mismatch between the deflected electron energy and the E-counter it struck. The correction is applied to the photon energy obtained from Tagger.

4.5. Fiducial Cuts

The geometrical fiducial cuts are applied in order to select regions of relatively uniform detector response, which could be reproduced by the Monte Carlo simulation. The study was performed sector by sector for the $\gamma d \rightarrow pp\pi^-$ reaction [29] to investigate how it depends on particle charge and particle creation vertex within the 40 cm eg3 target. A particle's trajectory depends on its momentum. Therefore, these cuts select angular ranges in the laboratory frame for various values of momentum.
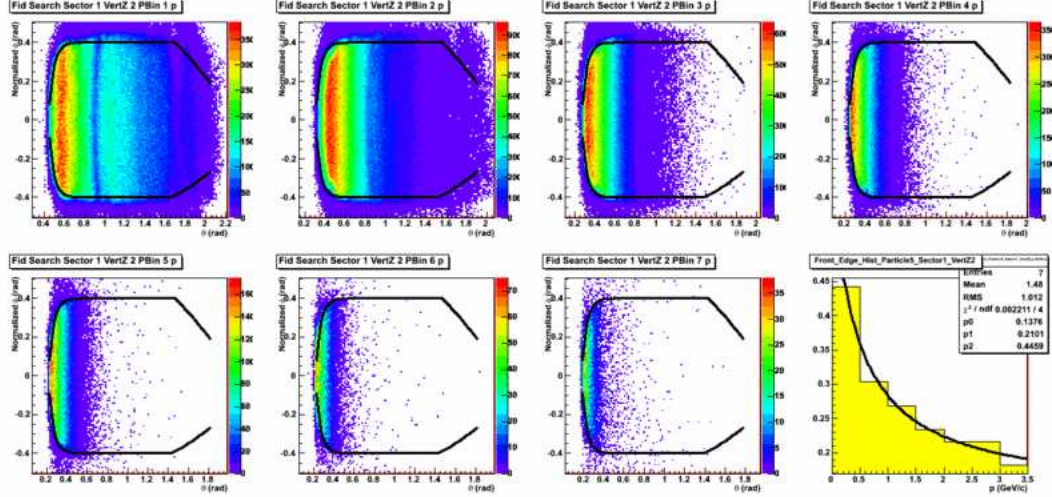
FIGURE 4.1. An example of the fiducial study for protons in sector 1 for middle vertex position. Top left to bottom right is the order of increasing proton momentum. Each histogram shows the distribution of ϕ versus θ in the sector frame and the black lines are the fiducial cuts applied. The last plot shows the minimum θ cut value versus momentum.

Overall, the study has four independent variables: charge (positive or negative), three groups of vertex positions, six sectors, and momentum. Particles are grouped according to these variables. For each group, the ϕ versus θ distribution is plotted, and a cut is produced according to the distribution. One example is shown in Figure 4.1. It shows the fiducial study of protons in sector 1 for the middle vertex position. Each histogram shows the distribution of ϕ versus θ for protons, and the black lines are the fiducial cut applied in each kinematic region. The bottom right histogram shows the lowest angle cut, corresponding to the forward-most angle protons of different momentum can be detected efficiently. A similar study is done for π^-, which is not shown here. The study can be further extended to any positive charged particles, by using the proton cuts, and to any negative charged particles, by using the π^- cuts. The reason is that a particle's trajectory does not depend on its mass. Please note that fiducial cut needs to be performed after the energy loss correction and momentum correction because the cut replies on correct particle momenta.
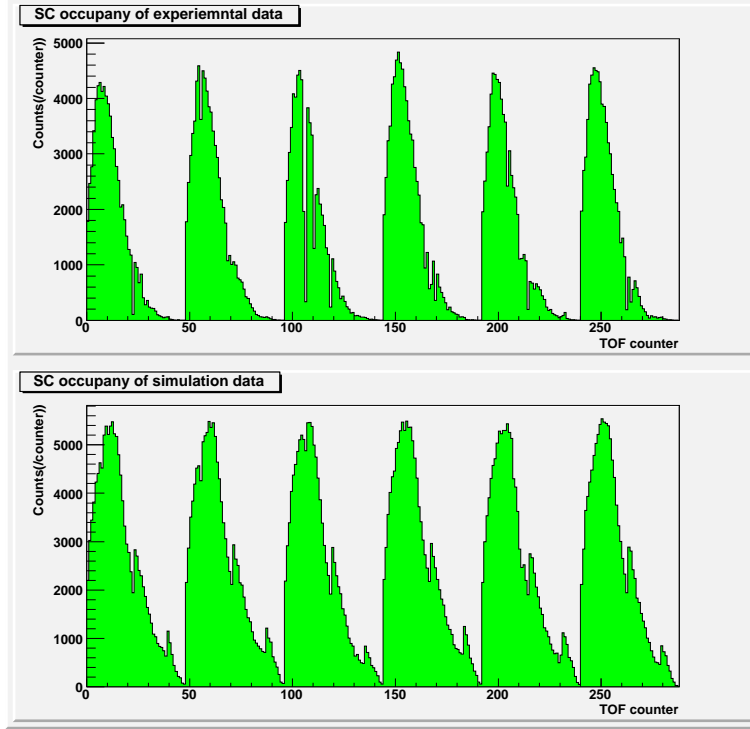
FIGURE 4.2. The occupancy of 287 SC channels, for the experiment (top) and simulation (bottom). Peaking structure in the bottom plot, reflects the distinct geometry of the TOF paddles. The boundaries are more subdued in the experimental data.

4.6. SC Occupancy Cut

Most of the SC counters have near 100% efficiency. But as shown in Figure 4.2 the comparison of the eg3 experiment and simulation reveals that the TOF counters (22,105,106,110,118,214,262) had lower than normal occupancies during the eg3 run period. The TOF counter inefficiency was not considered during the GPP procedure in our simulation. Therefore the events with particles related to those TOF counters were simply cut away for the experimental and simulated data.

4.7. DC Wire Efficiency Correction

The DC wire efficiencies have been studied by comparing the measured occupancy of a wire to its expectation value which is taken as the average of its neighboring wires [31]. The DC conditions during the eg3 run period had two major changes, thus three

efficiency maps are made for three sub run periods, which are run 45548 - 45627, 45804 - 45915 and 45916 - 46113. The data ratio from the three sub run periods is 21:26:53. All maps are put into CALDB and used by GPP in the simulation according to this ratio.

4.8. UNTRIGGERED TAGGER T-COUNTER CORRECTION

As discussed in Section. 2.4.1, only the first 19 T-counters in the tagger system were included in the eg3 trigger system, although all T-counters were recorded in the output data stream. Thus, events caused by photons associated with recoil electrons hitting counters 20 - 61 were only recorded when there was at least one recoil electron hitting one of the first 19 T-counters within the trigger time window . This causes a discontinuity around 4.5 GeV for any distribution over photon energy E_γ. The photon flux calculation software package, GFLUX [32] uses "out-of-time" photons, which are not affected by this trigger condition. Therefore, the result from GFLUX could not account for this discontinuity, and additional corrections need to be applied (see Section 6.2).

We use a practical approach for the correction. The photon flux normalized yield of the proton and neutron channel exclusive events which satisfy the event selection conditions mentioned in Section 5, are plotted against E-counter numbers as shown in Figure 4.3. The reason we plot the distributions over E-counters is because they are the basic units of Tagger energy detection. And E-counter and T-counter correspondence is shown in Figure 4.4. The photon energy E_γ rises almost linearly when E-counter/T-counter number increases. The discontinuity at E_γ 4.5 GeV is between E-counter ID 187 and 188.

To estimate how large the drop is, both histograms are fitted with a step function to ensure a scaling factor can match the yield at the edge of the drop and also the linear slope before and after the drop. The resulting factors are 4.4 for the proton
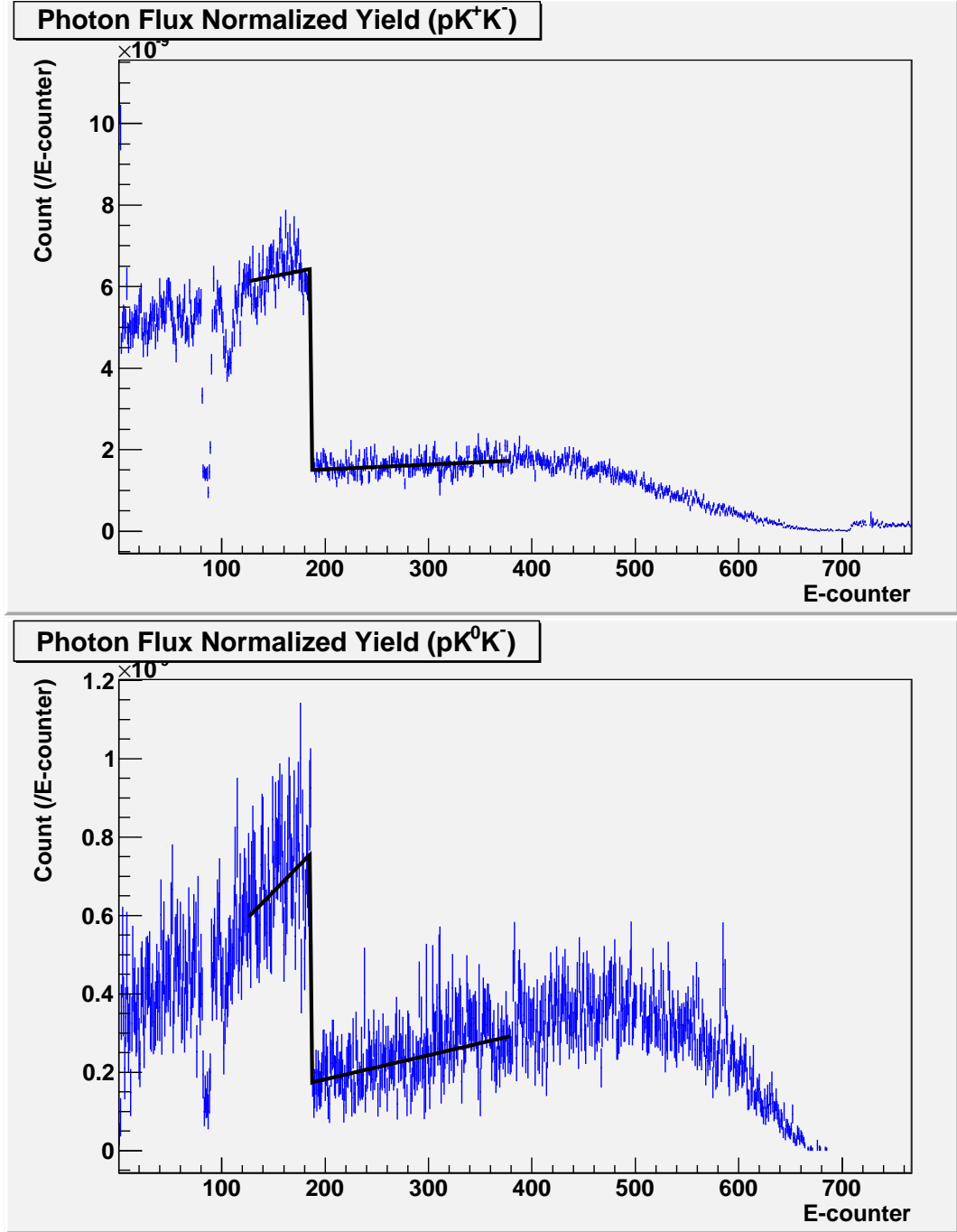
FIGURE 4.3. Normalized yield of the proton (upper) and neutron channel (lower) exclusive events versus E-counter logic paddles. The drop happens at the edge of the triggered to untriggered region. A linear step function with a scaling factor is used to fit the histogram.

channel and 5.2 for the neutron channel. The estimated relative errors are about 15% in both channels.
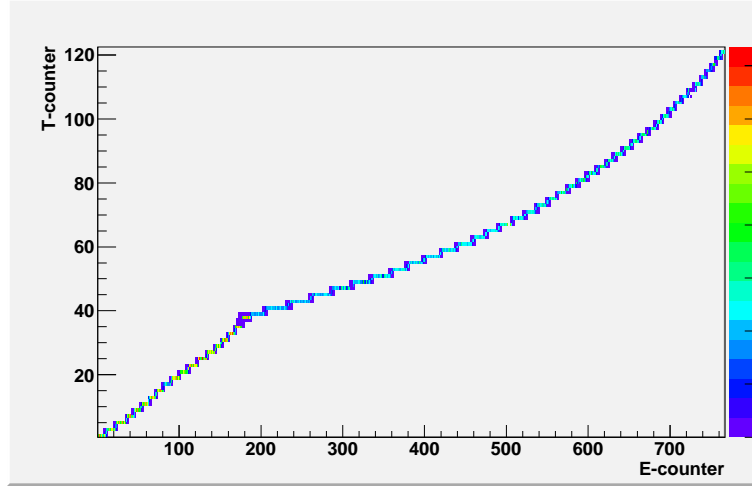
FIGURE 4.4. E-counter, T-counter correspondence. They are arranged so that each E-counter covers approximately the same energy range. Please note each T-counter has two IDs for two photo-multiplier (PMT) at both ends of its scintillator bar.

4.9. Trigger Efficiency Correction

To optimized multiple final particles detection, eg3 used two Level-1 trigger bit 5 and 6. Trigger bit 5 is set as a two track trigger requiring a coincidence in the TOF system and the start counter ST in the same sector for at least two sectors: $(TOF \times ST)^2$. Trigger bit 6 is a three track trigger requiring TOF and ST coincidences for at least three sectors: $(TOF \times ST)^3$. The bit 5 trigger was prescaled with a factor varying from run to run and the trigger bit 6 trigger is not prescaled. Trigger bit 5 and 6 are set independently, so one event can have bit 5 or bit 6 or both. We call an event trigger bit 5 event whenever the bit 5 is set and trigger bit 6 event whenever the bit 6 is set. Both trigger bit 5 and bit 6 have some efficiency issue depending on the number of final state particles. For an event with 3 (e.g. the proton channel) or 4 (e.g. the neutron channel) final state particles in at least three sectors of CLAS, both trigger bits should be registered if they are 100% efficient. However, the photon-flux-normalized yields of both trigger bits show difference and the bit 5 yield is higher than the bit 6 yield because bit 5 should better efficiency than bit 6.

The Level-1 trigger is in coincidence with the Master OR signal from the first 20 of T-counters of the photon tagger. For a large portion of the experiment, the Master OR also is passed through a coincidence with the start counter before going into the asynchronous input of the trigger supervisor in order to reduce the trigger background. The bit 5 prescale factor and with-or-without start counter coincidence of all good runs are shown in Table 2.1). The eg3 experiment ran with a higher photon beam intensity than any previous CLAS experiment. The counting rates in Hall B tagger T-counters and the CLAS start counter exceeded their optimal values. There is no evidence for significant tagging inefficiencies, but the analysis of the data suggests that there are trigger inefficiencies associated with the CLAS start counter.

A study has been done for the normalized yields of the events containing a well identified $\Lambda(p\pi^-)$ and two other time-based tracks in the CLAS detector [33]. Each event contains at least four time-based tracks in at least three sectors. For each event,
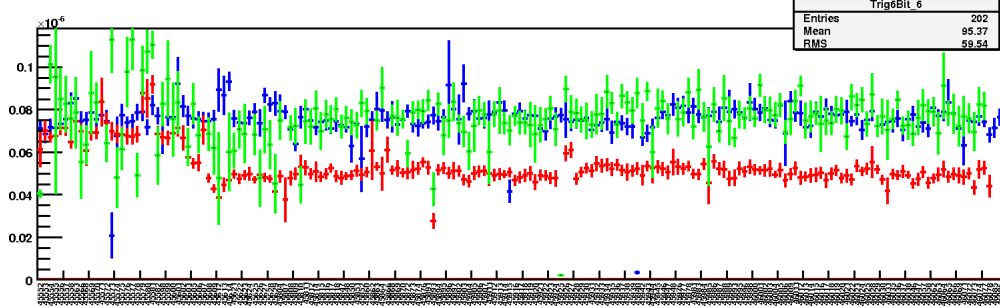
FIGURE 4.5. Comparison of normalized rates of inclusive Λ production with different trigger bits. Events of at least four particles are selected. Prescale factor corrected rates of events with bit 5 are plotted in blue. Normalized rates of events with bit 6 are plotted in red. Where the discrepancy starts to appear corresponds to the change of run condition around ST is added in the asynchronous input of the trigger supervisor. Data points in green represents normalized rate of bit 6 but corrected by a factor to match data points in blue.

a photon in the triggered tagger range (T-counters from 1-19) is required to match in time with the reconstructed particles in CLAS. The photon flux normalization for these studies was done by integrating the number of photons in the tagger within the same energy range. The normalized yields of the trigger bit 5 and bit 6 versus the run number are shown in Figure 4.5. The yields for the trigger bit 5 are corrected for the prescale factor on a run-by-run basis. The yields of trigger bit 6 with ST (early runs) are higher than the yields of trigger bit 6 without ST (later runs), but the yields of trigger bit 5 with or without ST show overall similar height.

Furthermore, Figure 4.6 shows the dependence of the event rates on the current for various number of final state particles, and the linear fits to the points. The trigger efficiency drops as the current increasing. The trigger bit 5 shows larger efficiency than the trigger bit 6 and the trigger with ST shows larger efficiency than the trigger without ST. And the trigger efficiency depends on the physical channel of interest. For a single event, its trigger condition can one of four kinds: bit 5 with ST, bit 5 without ST, bit 6 with ST, bit 6 without ST. The one with highest rate is bit 5 without ST. If we assume it has near 100% efficiency, all other three kinds of event can be corrected to this. After the correction, either bit 5 or bit 6 events will give the
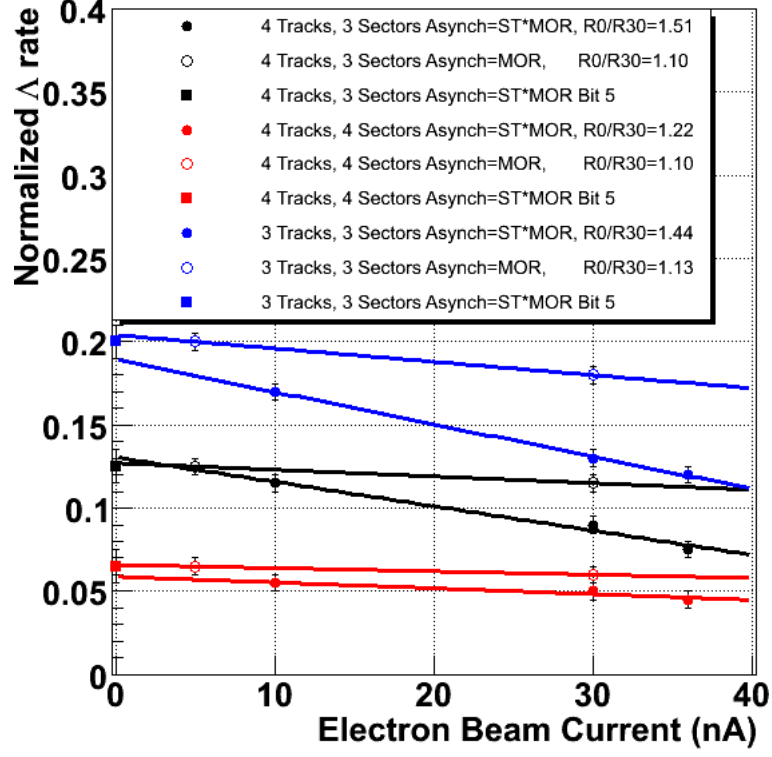
FIGURE 4.6. Normalized rate of events containing Λ versus electron beam current. Black lines are fits to the data with 4-track events in four different sectors. Red lines are fits to the data with 4-track events in three different sectors. Blue lines are fits to the data with 3-track events in three different sectors.

correct yield. The number of bit 5 events prior being multiplied by prescale factors (6 or 21) is only about 10% of the number of bit 6 events. Therefore the bit 5 events after being multiplied by prescale factors has much larger statistic error than the bit 6 events. We can not combine bit 5 and bit 6 events to enhance the statistics because there are events with both bit 5 and bit 6 set which can not be corrected. Considering all facts, we decide to use corrected bit 6 events for the analysis of physical reactions.

To verify the correction method, the normalization procedure was checked using $d(\gamma, \pi^- \Delta^{++})n$ reaction with the detection of the π^+ $\pi^- p$ final state [34]. The cross sections of this process is expected to be mostly dominated by the photoproduction on a quasifree proton $\gamma p \to \pi^- \Delta^{++}$. Although final state interactions contribute to this process, we do not expect their impact to be significant within the precision which we are interested. We compared the total cross sections of $\gamma p \to \pi^- \Delta^{++}$ from the CLAS

TABLE 4.1. Trigger efficiency correction

	bit 5 without ST	bit 5 with ST	bit 6 without ST	bit 6 with ST
proton channel	1	0.875	0.75	0.625
neutron channel	1	0.375	0.5	0.458

g11 run to $d(\gamma, \pi^-\Delta^{++})n$ cross sections from eg3. The resulting cross sections of the two data sets are in a good agreement within 20% of systematic error, and they are also compatible with the SAPHIR data [35] as well.

For the proton and neutron channel of $\Lambda^*(1520)$ photoproduction, we studies the normalized yields of $\Lambda^*(1520)$ of all four kind of trigger conditions. Limited the statistics of the reactions, we can not do a run-by-run analysis, but combining the all runs of the trigger without ST or trigger with ST, we can still have corrections as shown in Table 4.1. The total photon flux for all runs of the trigger without ST is 1.24256e+13 and the total photon flux for all runs of the trigger with ST is 6.69736e+13. They are 15.6% and 84.4% of the total photon flux in eg3. The overall correction of bit 6 events is calculated as $0.156 \times (1/0.75) + 0.844 \times (1/0.625) = 1.56$ for the proton channel and $0.156 \times (1/0.5) + 0.844 \times (1/0.458) = 2.15$ for the neutron channel.

4.10. TRIGGER CONDITION CUT

We did not employ any trigger in the simulation. To match the eg3 experimental trigger bit 6, we select only simulated events with particles in at least three sectors. Please note that those particles are all time-based tracks, while actual CLAS trigger bit 6 is based on low level electronic signals. To make sure the better match between the experiment and simulation, all particles in at least three sectors are also required for the experimental data.
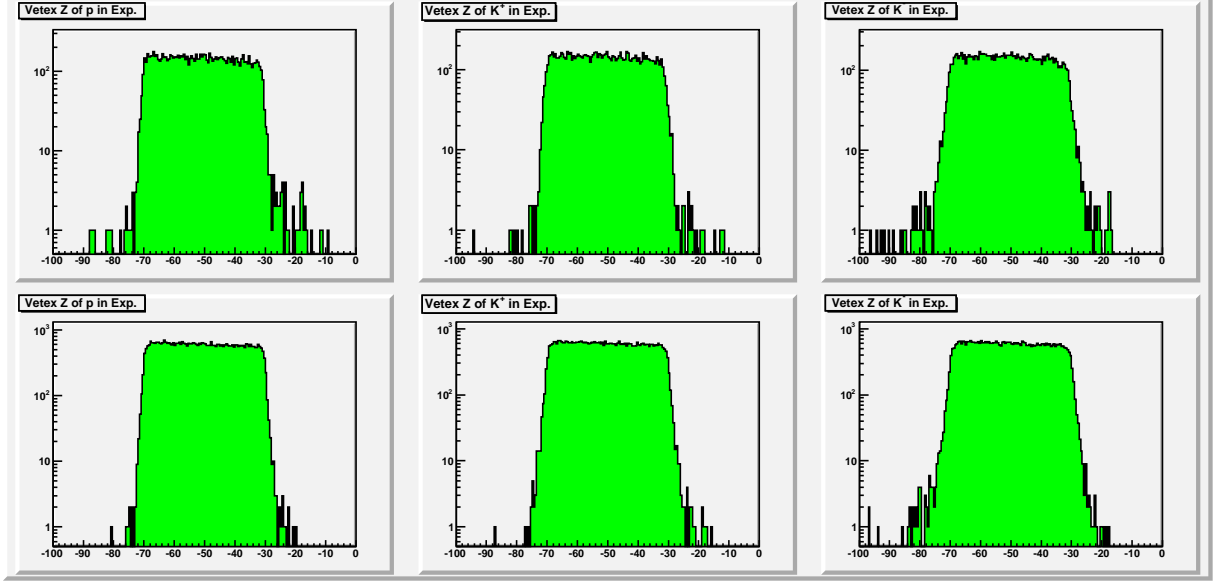
FIGURE 4.7. (**Proton Channel**), vertex Z of p, K^+, and K^- distributions for the experiment (top) and simulation (bottom).

4.11. VERTEX Z CUT

To determine the vertex of a particle, we extrapolate its trajectory in DC to the beam line and looking for where the distance of closest approach is. The vertex Z of all final state particles are examined after the exclusive selection (Section 5.6), quasi-free selection (Section 5.7), and a very loose $\Lambda^*(1520)$ mass cut of $1.45 < M(pK^-) < 1.6 GeV$. The results of the two channels are shown in Figure 4.7 and Figure 4.8 for the experimental and simulated data. Except the weak $K_s \to \pi^+\pi^-$ with a small decay length $c\tau = 2.7cm$, there are no weak process in either of the two reaction channels. Therefore, we can safely cut at $-75 < vertexZ < -25cm$ which is 5 cm larger than the actual target range $-70 \sim -20cm$ to allow the CLAS vertex resolution.

4.12. MOMENTUM CUT

Most of the CLAS detector components have detection thresholds for the minimum momentum of a particle passing through. The thresholds depends electronic status and particle properties. To match the detection thresholds between the experiment and simulation, the momenta of all final state particles are examined after the
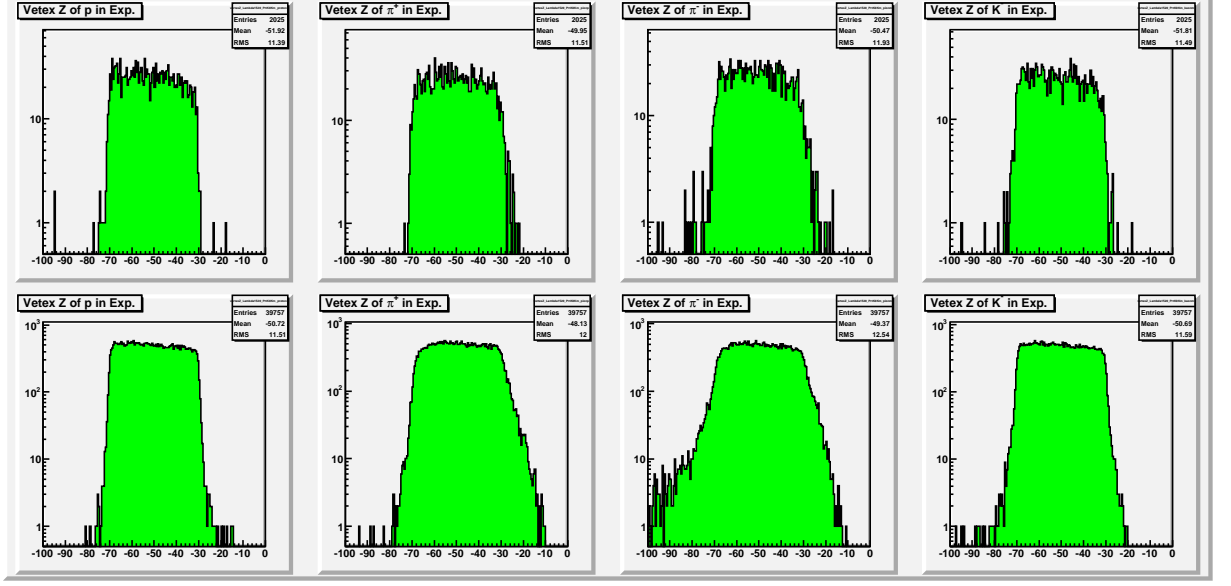
FIGURE 4.8. (**Neutron Channel**), vertex Z of p,π^+,π^- and K^- distributions for the experiment (top) and simulation (bottom).

exclusive selection (Section 5.6), quasi-free selection (Section 5.7), and a very loose $\Lambda^*(1520)$ mass cut of $1.45 < M(pK^-) < 1.6GeV$. The results of the two channels are shown in Figure 4.7 and Figure 4.8 for the experimental and simulated data. After comparing the distributions between the experiment and simulation, the cuts for the proton channel are chosen to be $Mom_p > 0.4GeV$, $Mom_{K+} > 0.4GeV$, and $Mom_{K-} > 0.4GeV$ and the cuts for the neutron channel are chosen to be $Mom_p > 0.4GeV$, $Mom_{\pi+} > 0.1GeV$, $Mom_{\pi-} > 0.1GeV$, and $Mom_{K-} > 0.2GeV$.

4.13. SUMMARY

All of the corrections and cuts above are essential to establish physically meaningful events for the later analysis process. We summarize how they apply on the experimental and/or simulated data in Table 4.2.
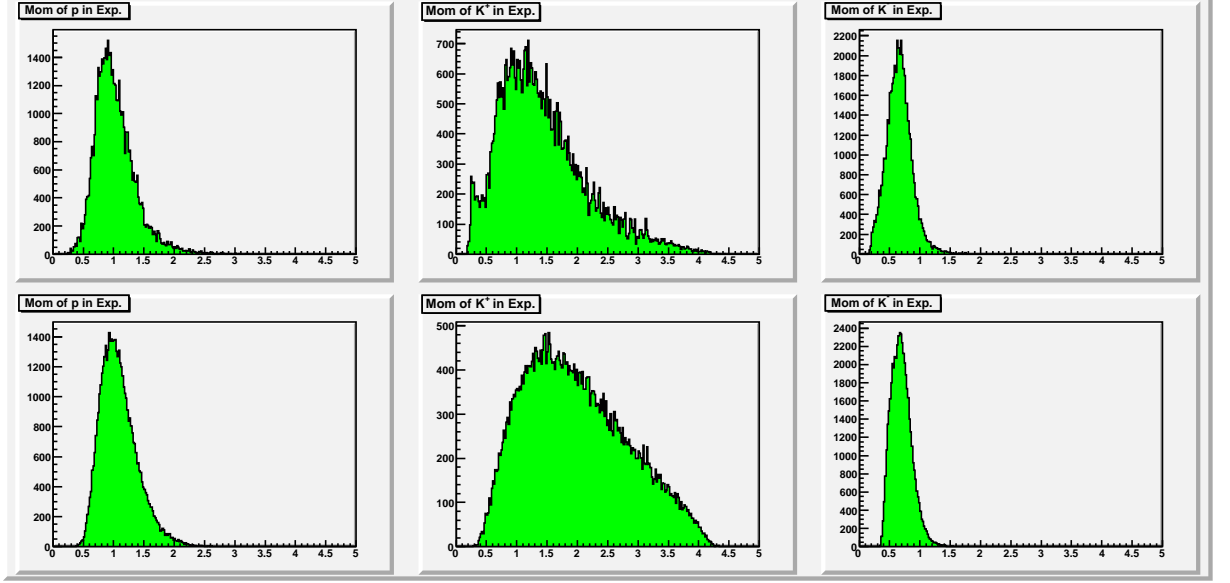
FIGURE 4.9. (**Proton Channel**), momentum of p,K^+, and K^- distributions for the experiment (top) and simulation (bottom).
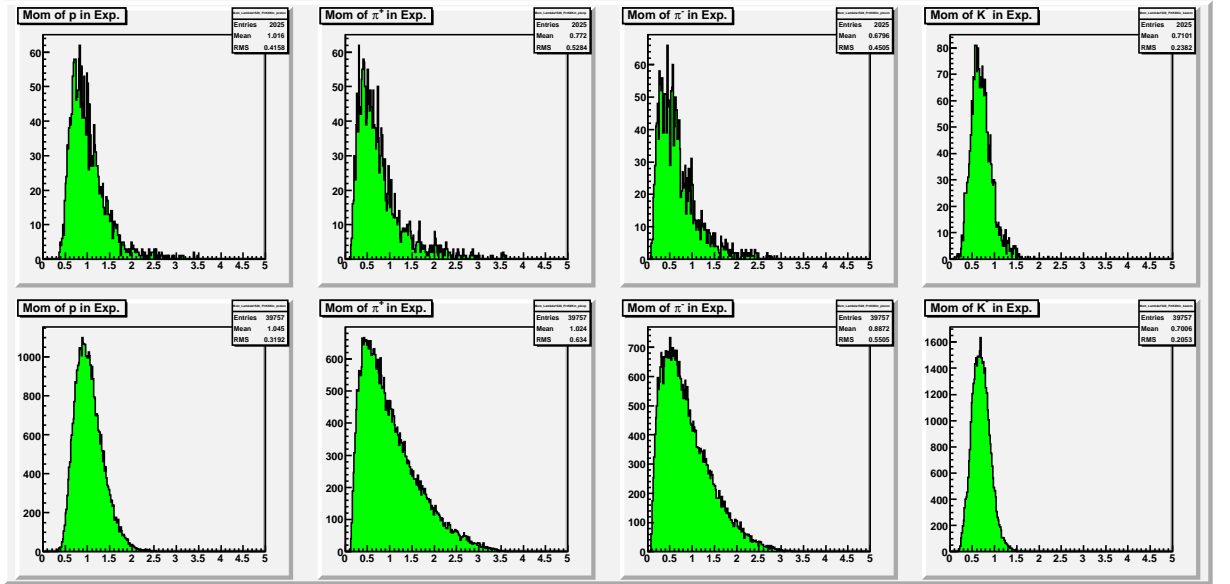
FIGURE 4.10. (**Neutron Channel**), momentum of p,π^+,π^- and K^- distributions for the experiment (top) and simulation (bottom).

TABLE 4.2. Applied corrections and cuts

Correction and cut name	experiment	simulation
Beam trip cut	Y	N
Eloss correction	Y	Y
Momentum correction	Y	N
Photon energy correction	Y	N
Fiducial cut	Y	Y
SC occupancy cut	Y	Y
DC wire efficiency correction	N	Y
Untriggered tagger T-counter correction	Y	N
Trigger efficiency correction	Y	N
Trigger condition cut	Y	Y
Vertex Z cut	Y	Y
Momentum cut	Y	Y

CHAPTER 5

EVENT SELECTION

To select the events for the proton and neutron channels in the experimental and simulated data, we studied each steps of the selection conditions in detail. They are presented here in same order as they are applied.

5.1. CHARGED PARTICLES

For the experimental and simulated data, only the events with 2 positive and 1 negative final state particle are selected for the proton channel pK^+K^- and only the events with 2 positive and 2 negative final state particles are selected for the neutron channel $p\pi^+\pi^-K^-$. All charged particles are required to have good time-based tracking (see Section2.4.2).

5.2. EVENT PHOTON SELECTION

There are two reasons that we need to know the photon causing an event. First, the energy of the event photon is needed to guarantee the exclusivity of a reaction. Second, we need to know the time of the event photon, which is used as the event start time to identify the final state particles.

For the simulated data, there's only one photon in the tagger which is given by the event generator. Hence no event photon selection is needed.

For the experimental data, we need to pick out the event photon from all photons recorded for an event. Because the high luminosity and the use of the multi-hit pipeline TDCs in Tagger, eg3 has on average about 30 photons in Tagger per event. The number is higher than in previous CLAS experiments and the cooking program

could not find the corrected event photon for most of events. We have to redo the event photon selection in the data analysis process and tailor it to different reaction channels.

The photon time in Tagger was synchronized to the RF signals of the accelerator and calibrated to the eg3 target center. These photons are 2 ns apart from each other. The event photon time should be the same as the event start time when a physical event happens, which is again the same as the particle vertex time when the resulting particles leave the event vertex. The particle vertex time can be calculated by

$$t_{vtc} = t_{TOF} - \frac{l_{track}}{\beta c} - \frac{Z_{vt} - Z_{target}}{c} \tag{5.1}$$

where t_{vtc} is the particle vertex time shifted to the target center, t_{TOF} is the TOF time of the particle, l_{track} is the trajectory path length from the particle vertex to the TOF counter which the particle hits, $\beta = \frac{p}{\sqrt{p^2+m^2}}$ is calculated from the DC momentum and mass hypothesis from the particle data group (PDG) mass of the particle [1], Z_{vt} is the vertex position and Z_{target} is the target center position, which is -50 cm for eg3. All the information above can be obtained from CLAS except the particle mass since we have not done any particle identification yet. Hence we have to assume the particle's identity first.

5.2.1. Neutron Channel. For the neutron channel $p\pi^+\pi^-K^-$, there are two pions in each event and they come from the $K_s \to \pi^+\pi^-$ decay with a very narrow width. So we loop through all combinations of 1 positive and 1 negative particle and assume their masses to be the PDG pion mass. During the looping, we do the following step by step:

1. Only pairs with invariant masses within 0.05 GeV of the K_s mass peak of 0.5 GeV are kept for initial candidates. This is a very loose cut since the K_s invariant mass peak resolution is about $3\sigma = 0.02 GeV$.

2. A valid vertex time difference, $t_{vtc}(\pi^+) - t_{vtc}(\pi^-)$ should be around 0. Any pair is required to be within the two dimensional 3σ cuts as shown in Figure 5.1.
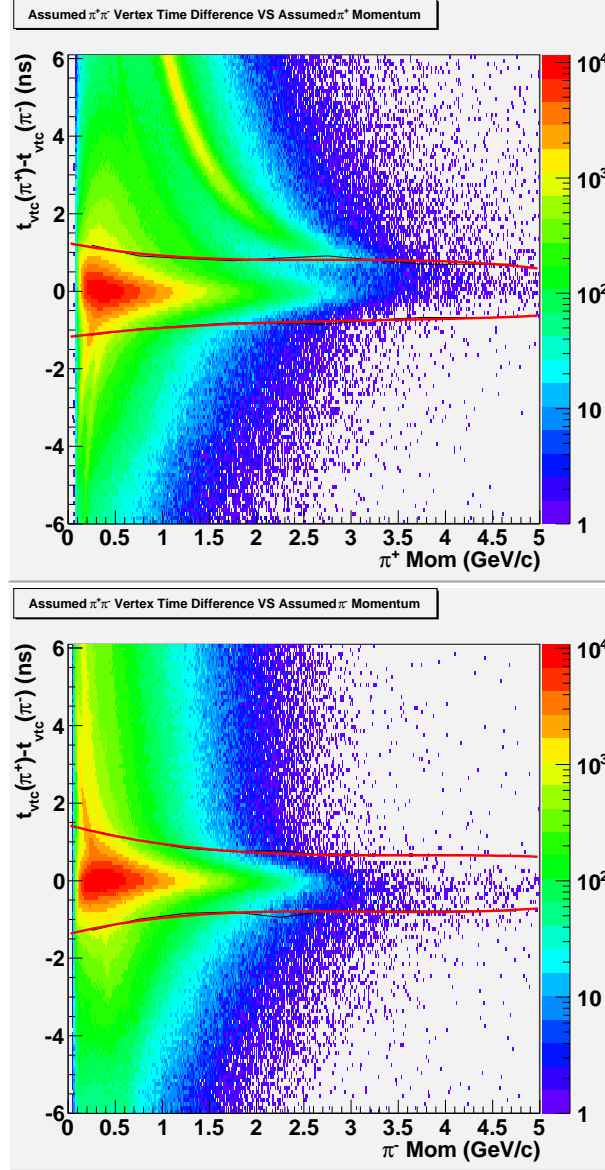
FIGURE 5.1. $t_{vtc}(\pi^+) - t_{vtc}(\pi^-)$ VS π^+ momentum (left) or π^- momentum (right). The 3σ cut line in red is obtained by fitting the projections at different momenta.

3. Then if there are still more than one pair left, we will choose the pair with the least $\chi^2_{K_s}$ as defined by.

$$\chi^2_{K_s} = \left(\frac{M(\pi^+\pi^-) - M(K_s)}{0.02}\right)^2 + \left(\frac{t_{vtc}(\pi^+) - t_{vtc}(\pi^-)}{2}\right)^2 \qquad (5.2)$$

Where 0.02 GeV is chosen to represent the width of invariant mass M_{K_s} distribution and 2 ns represents the width of $t_{vtc}(\pi^+) - t_{vtc}(\pi^-)$ distribution.

4. After the three steps above, we have a good candidate pair of $\pi^+\pi^-$. Even though the two pions are from a weak decay, the K_s decay length $c\tau p/m$ is only a couple of centimeters because, $c\tau$ is 2.7 cm and the average momentum p for the eg3 run is of the same order as the mass 0.5 GeV. Considering the CLAS particle vertex resolution from DC is also a couple of centimeters, the vertices of the $\pi^+\pi^-$ from a K_s decay match the event vertex within their resolution and the average vertex time of the $\pi^+\pi^-$ pair can be regarded to even higher accuracy as the event vertex time t_{vtc}. Then we loop through all photons of an event to find the photon with the closest time to the t_{vtc}. We call this photon $\gamma - closest$ and plot its time difference with the event vertex time, $t_{\gamma-closest} - t_{vtc}$ in Figure 5.2. The 2 ns photon time structure in Tagger is clearly seen. Only the events with their $\gamma - closest$ photons staying within the peak at 0 are good events where Tagger detects the event photons. All other events are bad events with the tagger failed to detect the event photon or misidentified due to our selection method, and they are excluded by a ± 1 ns cut. After the cut, the good events are kept, and their $\gamma - closest$ photons are their event photons with the event start time known from the $\gamma - closest$ photon time.

5.2.2. Proton Channel. For the proton channel pK^+K^-, there is neither a pion nor any narrow baryon resonance in the event which could be used to help identify the event vertex time. We have to make assumptions for all three charged particles at the same time. The negative one is assumed to be K^- and the two positive ones are assumed to be p, K^+ and vice versa. Then the following steps are carried out:

1. For the two possible combinations caused by different pK^+ assumptions, we want to choose the one with the vertex time of all three particles closer to each other. To do this, we calculate the maximum particle vertex time difference within each combinations. Then we compare the two maxima from the two combinations. The combination with the lower maximum is the one where the vertex time of all three particles is closer to each other.

2. We apply a 2 ns cut on the maximum particle vertex time difference of the selected
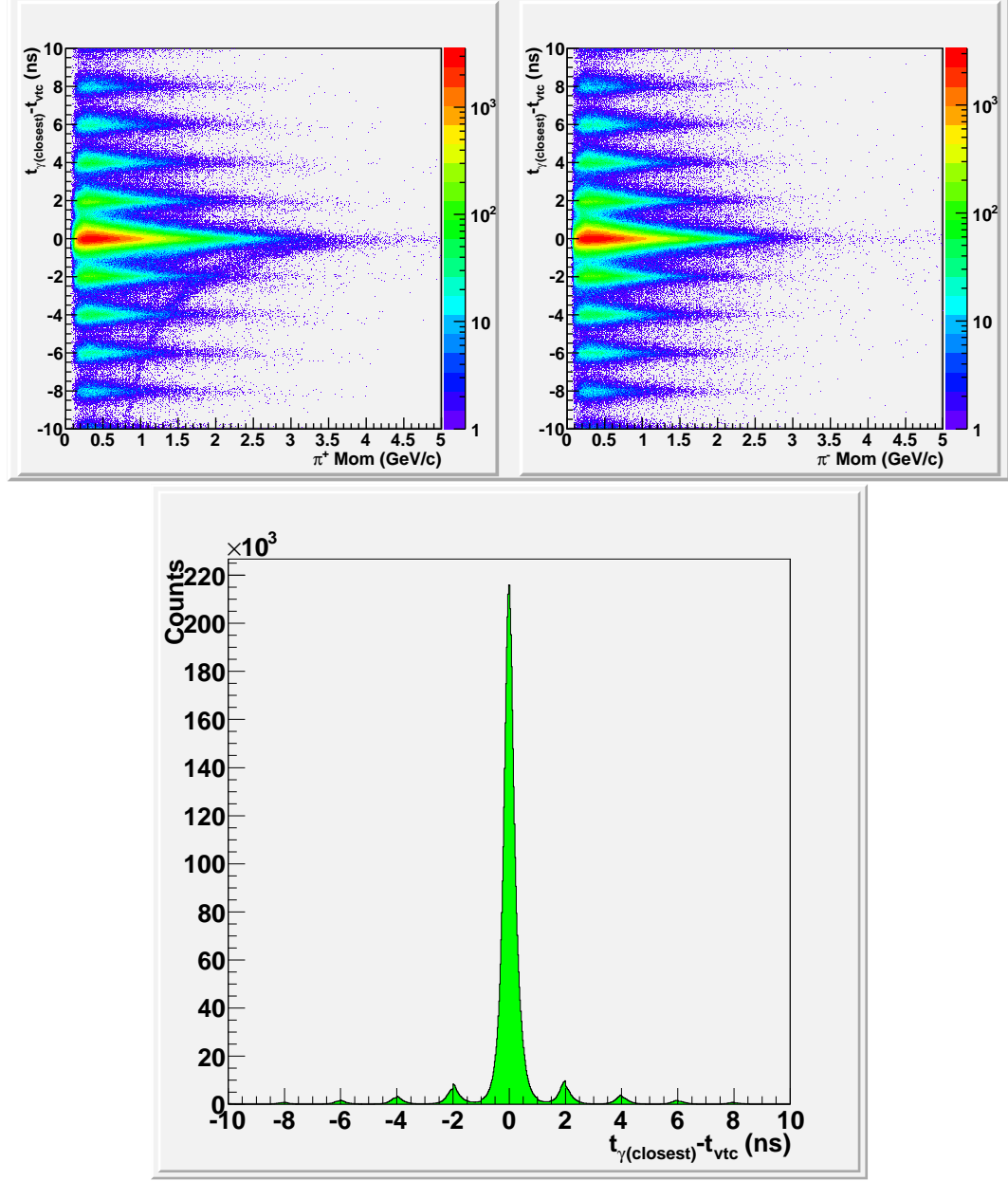
FIGURE 5.2. (**Neutron Channel**),$t_{\gamma-closest} - t_{vtc}$ VS π^+ momentum (left) or π^- momentum (right). The good events are within ± 1 ns of the peak at 0. The bad events have only photons detected from the neighboring beam bunches. $t_{\gamma-closest} - t_{vtc}$ is projected in the one dimensional plot, and we can see that the number of bad events is only a few percent of the number of good events.

combination. This is because if pK^+K^- are really in an event and thus from one event vertex, the difference should not be too large. The selection of the cut value 2 ns is based on the consideration of that the photon times in Tagger are 2 ns apart so to
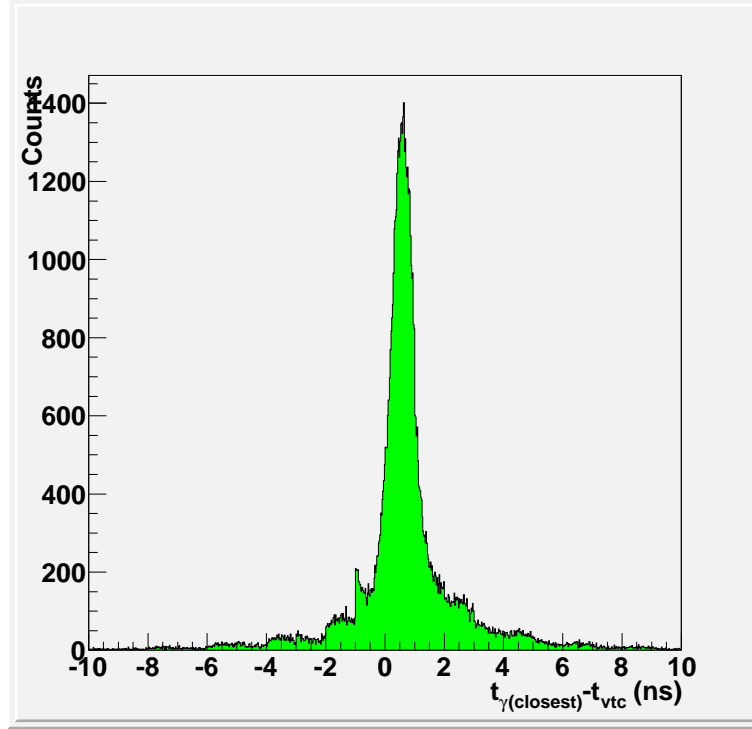
FIGURE 5.3. (**Proton Channel**), $t_{\gamma-closest} - t_{vtc}$. Our conservative approach of event photon selection conditions results in a large number of contaminations

compare the particle vertex time with a photon time, so we need the particle vertex time not spreading larger than that.

3. Finally, the average pK^+K^- vertex time is regarded as the event vertex time t_{vtc}. Then the procedure is very similar to the neutron channel. After looping through all photons in Tagger to find the photon with the closest time to the t_{vtc}. We call this photon $\gamma-closest$ and plot its time difference with the event vertex time, $t_{\gamma-closest} - t_{vtc}$ in Figure 5.3. As we can see, the good events are not that well localized around 0. This is expected because there are still large contaminations from the main background channel $p\pi^+\pi^-$. We widen the cut to ± 2 ns to pick the event photon and leave the task of cleaning the background to Section 5.5 later.

5.2.3. Multi-Hit Photon Selection. In both the neutron and proton channels, after the event photon selection procedure based on timing, about 80% of surviving events have only 1 photon selected, about 15% have 2 photons, and for the remaining

52

5%, the number of photons are larger than 2. This is because in each single electron beam bucket every 2 ns, there can be more than one electron having radiated a photon and thus more than one photon detected by Tagger. For one electron beam bucket, all these radiated photons are very close in time within the order of pico-seconds, but their energies can be very different. There can only be one true event photon per physical event, the event photon selection method by timing is not sufficient to distinguish these multi-hit photons within one electron beam bucket. To pick out the true event photon, we examine whether an event photon conserves the momentum and energy of the exclusive reaction. Later in Section 5.6, all of the multi-hit photons in an event are tested by missing nucleon mass cuts and only the photon with the right energy is identified as the true event photon.

5.3. PARTICLE IDENTIFICATION

After an event photon is selected, its time is regarded as the event start time t_0. We use the event start time, particle TOF time, flight path and momentum to calculate the particle TOF mass as defined by

$$\tau = \frac{1}{\beta} = \frac{t_{TOF} - t_0 - (Z_{vt} - Z_{target})/c}{l_{track}/c} \tag{5.3}$$

$$m_{TOF}^2 = p^2(\tau^2 - 1) \tag{5.4}$$

This quantity is always distributed around the PDG particle mass and broadened with increasing momentum when the CLAS time resolution starts to decrease. Protons are easily identified as their TOF mass distribution are well separated from those of kaons and pions. But the kaon mass is very close to the pion mass and their distributions become harder to separate at higher energies.

5.3.1. Neutron Channel. Figure 5.4 shows that all particles can be easily separated from each other by the red cut lines. The remaining K/π misidentification will be handled in Section 5.4
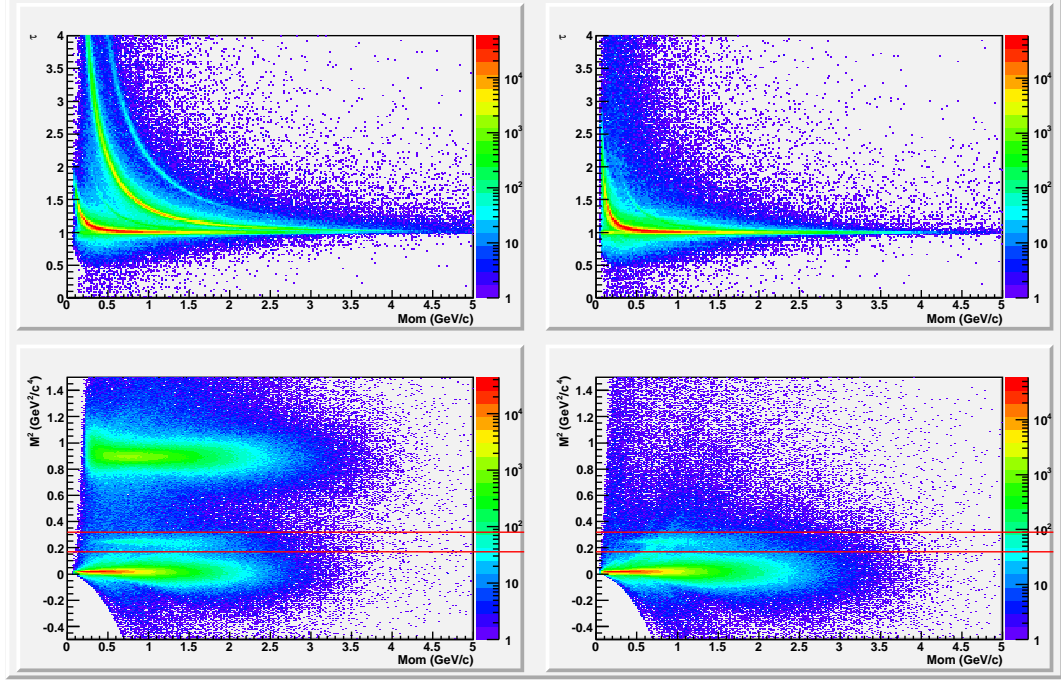
FIGURE 5.4. (**Neutron Channel**) with the final state particles $p\pi^+\pi^-K^-$, both τ (upper) and m^2_{TOF} (lower) VS momentum are plotted for the positive (left) and negative charged particles (right). The red cut lines separate p, K, π

5.3.2. Proton Channel. Figure 5.5 shows the side bands with wrong event photon selections due to our loose timing cuts and the limitation of the method involving particle assumptions. Because kaons are usually much fewer than pions, to optimize the kaon selection of the final state particles, we assign a particle as kaon whenever it could be either kaon or pion. The kaon/pion misidentification will be cleaned up later in Section 5.5.
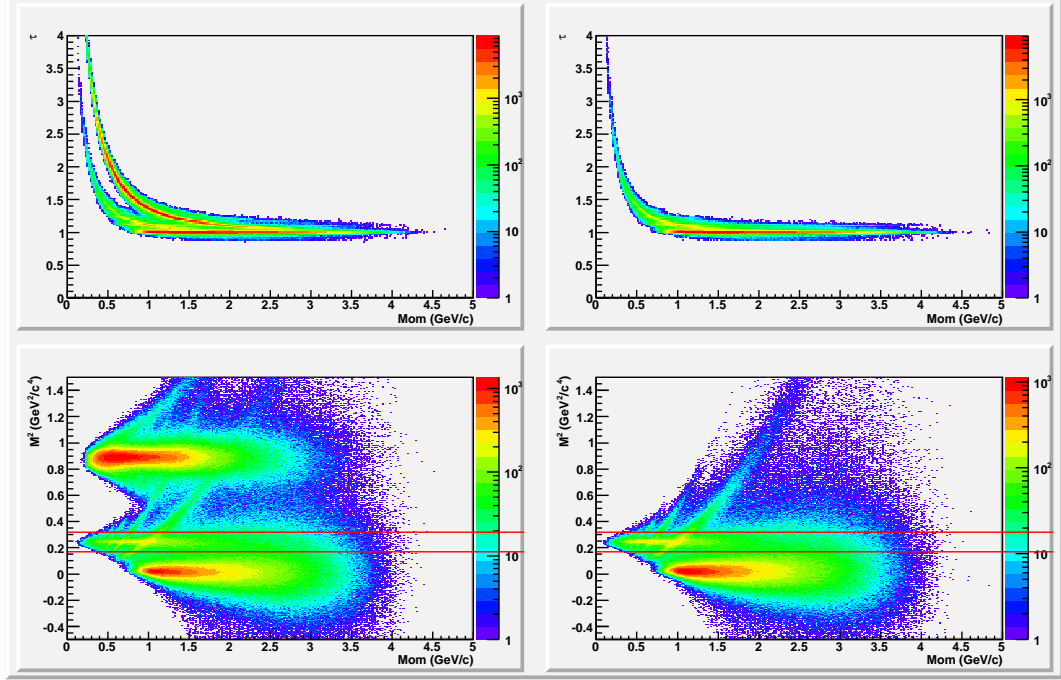
FIGURE 5.5. (**Proton Channel**) with the final state particles pK^+K^-, both τ (upper) and m^2_{TOF} (lower) VS momentum are plotted for the positive (left) and negative charged particles (right).
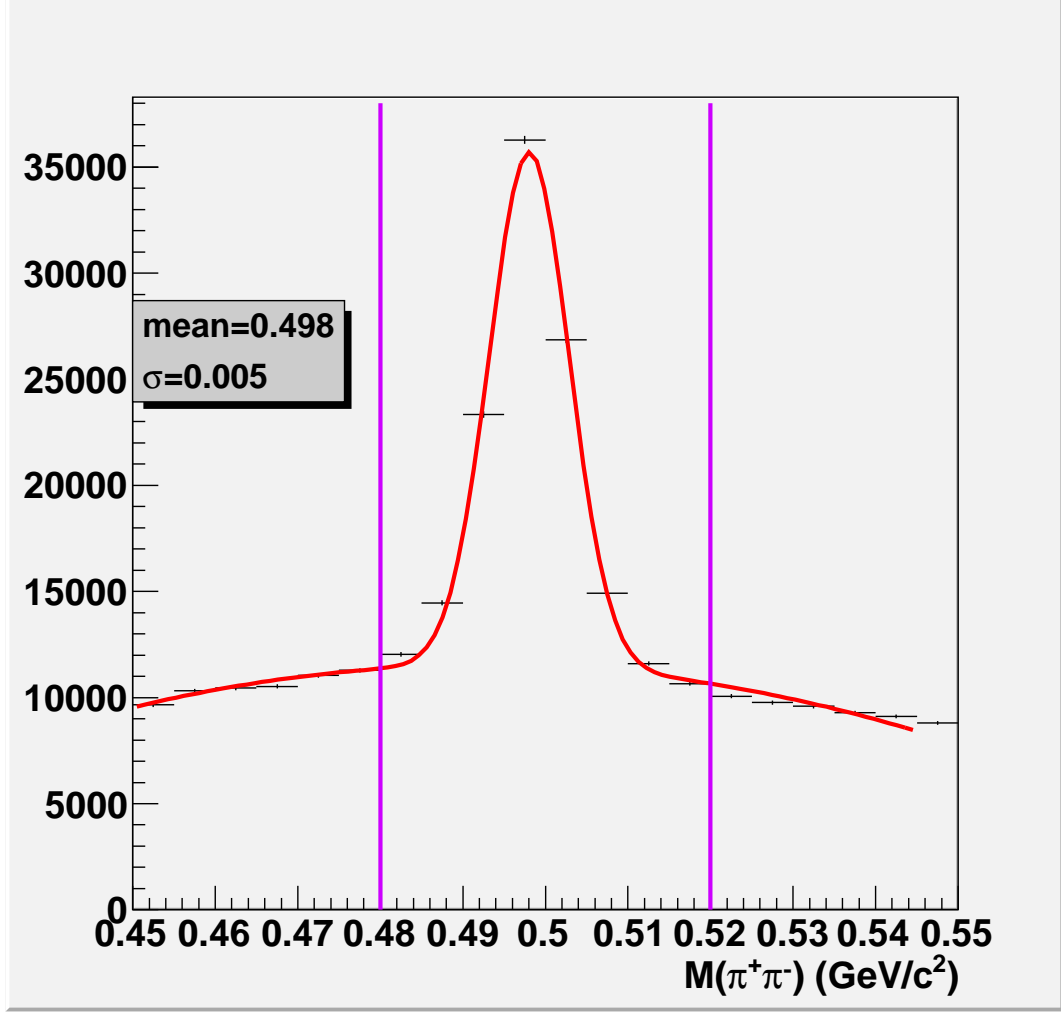
FIGURE 5.6. $M(\pi^+\pi^-)$ showing the 4σ cut after fitting by a Gaussian plus polynomial background.

5.4. K^0 SELECTION AND K/π MISIDENTIFICATION FOR THE NEUTRON CHANNEL

The K^0 is reconstructed by measuring its two decay pions from K_s. We use a very loose 4σ cut in the invariant mass $M(\pi^+\pi^-)$ spectrum to select the events of interest as shown in Figure 5.6.

The dominant background in this channel is the $\gamma d \to p\pi^+\pi^-\pi^-(p)$ reaction with $K^-/\pi-$ misidentification. If the K^- is indeed a K^-, the missing mass squared $MM_p^2(p\pi^+\pi^- K^-)$ should have a peak centered around the proton PDG mass squared $0.884~GeV^2$. If the K^- is actually a π^-, by the particle has a pion mass, we can

56
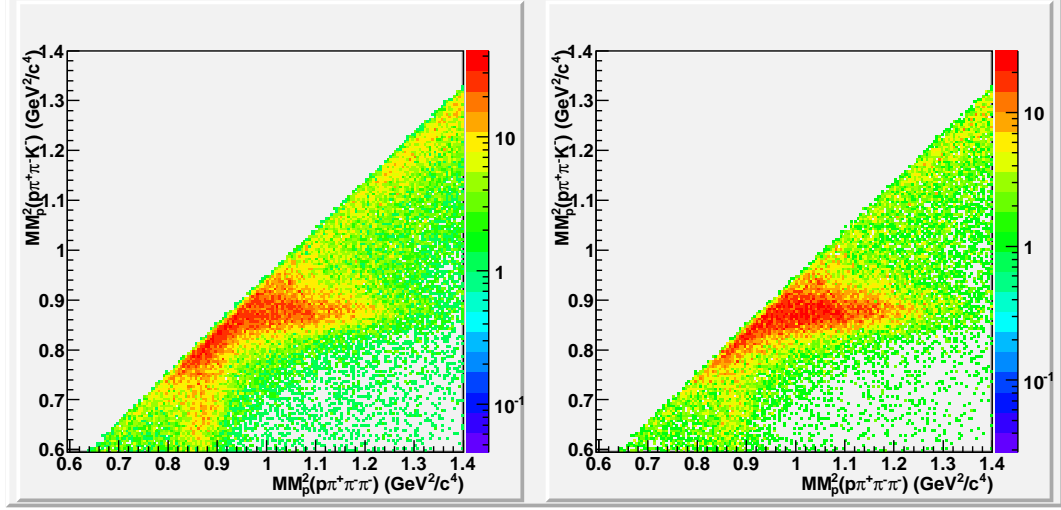
FIGURE 5.7. $MM_p^2(p\pi^+\pi^-K^-)$ VS $MM_p^2(p\pi^+\pi^-\pi^-)$ before (left) and after K_s selection cut (right). The K^-/π^- misidentification has been mostly removed by the cut.

calculate that the missing mass squared $MM_p^2(p\pi^+\pi^-\pi^-)$ should resulting in a peak centered at $0.884\ GeV^2$ as well. Plotting these two quantities against each other in Figure 5.7, one can see that in the left picture two peaks are entangled before the K_s selection cut, but in the right picture, after the K_s selection cut, the peak of $MM_p^2(p\pi^+\pi^-\pi^-)$ is mostly gone. The missing proton mass cut in Section5.6) will further eliminate the misidentified K^-/π^-.

To see how the K_s cut affects $MM_p^2(p\pi^+\pi^-K^-)$ distribution, we plot it one-dimensionally before and after the cut in Figure 5.8. The signal under the missing proton peak has been preserved and the background is reduced by the cut effectively.
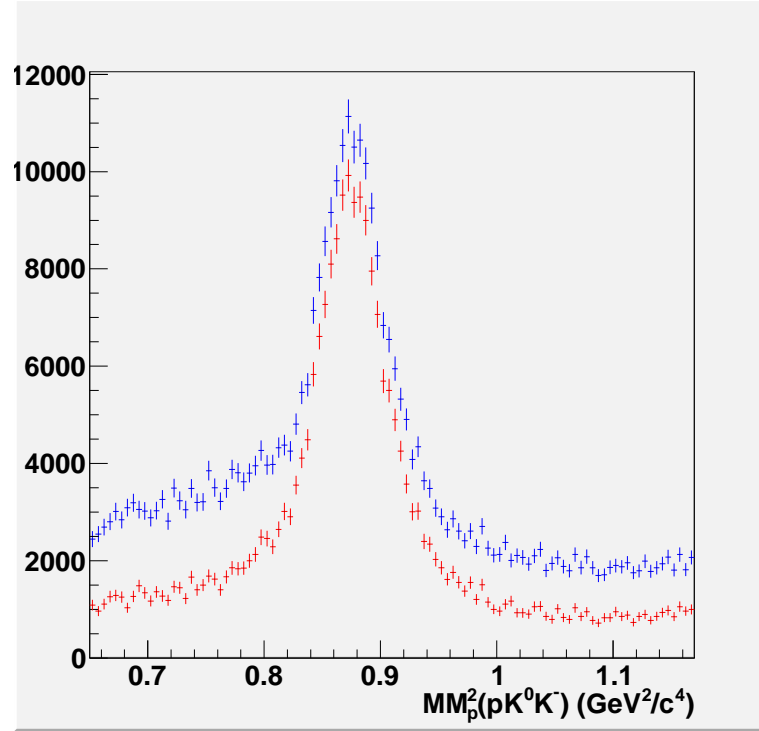
FIGURE 5.8. $MM_p^2(p\pi^+\pi^-K^-)$ before (blue) and after the K_s cut (red).
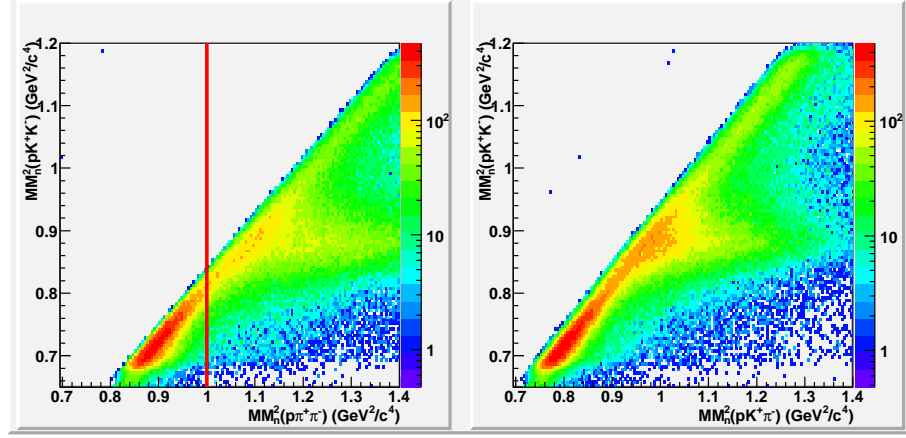
FIGURE 5.9. $MM_n^2(pK^+K^-)$ versus $MM_n^2(p\pi^+\pi^-)$ on the left where $MM_n^2(p\pi^+\pi^-)$ events can be cut out at the red line. $MM_n^2(pK^+K^-)$ versus $MM_n^2(pK^+\pi^-)$ on the right where there is no obvious indication of exclusive $MM_n^2(pK^+\pi^-)$ events.

5.5. K/π MISIDENTIFICATION FOR THE PROTON CHANNEL

In the proton channel, the dominant background channel is the $\gamma d \to p\pi^+\pi^-(n)$ reaction where K^+/π^+ and K^-/π^- are both misidentified. In the left figure of Figure 5.9, we assume that those two kaons have pion mass and compare the missing mass squared $MM_n^2(pK^+K^-)$ to $MM_n^2(p\pi^+\pi^-)$. The events with misidentified pions can be cut away effectively by requiring $MM_n^2(p\pi^+\pi^-) > 1$.

Another possible background is the $\gamma d \to pK^+\pi^-(n)$ reaction with only K^-/π^- misidentification. From the comparison of the missing mass squared $MM_n^2(pK^+K^-)$ with $MM_n^2(pK^+\pi^-)$ as shown in the right figure of Figure 5.9, one can see that this background is negligible because there is not $MM_n^2(pK^+\pi^-)$ peak at the right missing neutron mass squared of 0.884 GeV. The peak around 0.8 GeV is due to the background channel $\gamma d \to p\pi^+\pi^-(n)$, but shifted by the K^+/π^+ misidentification. There is no need to cut on this plot.

The $MM_n^2(p\pi^+\pi^-)$ cut removes the shoulder of the missing neutron mass squares peak of $MM_n^2(pK^+K^-)$ as shown in Figure 5.10.
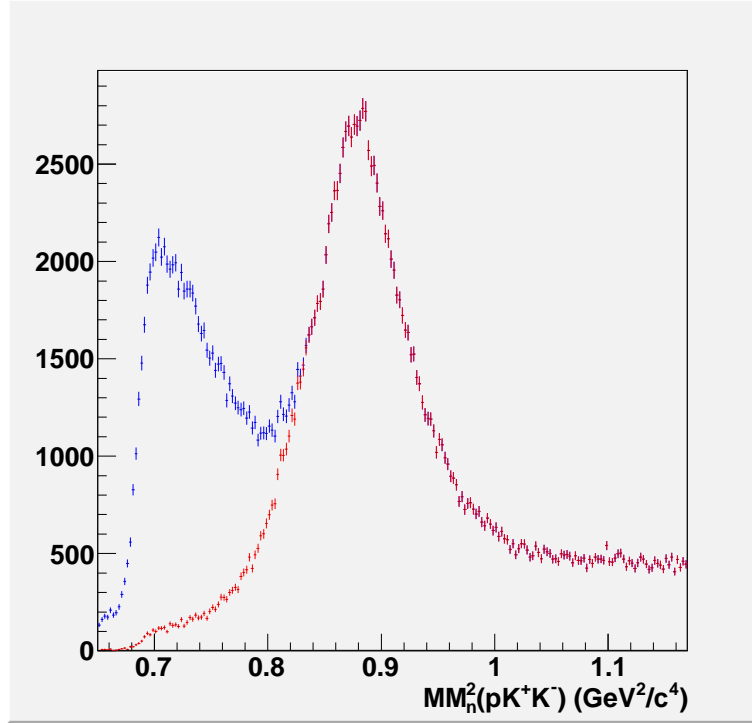
FIGURE 5.10. $MM_n^2(pK^+K^-)$ before (blue) and after the $MM_n^2(p\pi^+\pi^-)$ cut (red).

5.6. Missing Nucleon Mass Cut

The exclusivity of our two reactions is then ensured by cutting on their missing nucleon mass squared. 3σ cuts are applied in different photon energy bins to accommodate the decreasing CLAS resolution at high energies.

There are 6 energy bins for the neutron channel and 16 energy bins for the proton channel. Each of their missing nucleon mass square histograms (after a very loose $\Lambda^*(1520)$ mass cut of $1.45 < M(pK^-) < 1.6GeV$) is fitted by a Gaussian plus a polynomial background. The fitting functions and resulting means and widths with errors are plotted in Figure 5.11 for the neutron channel and Figure 5.13 for the proton channel. It is clearly that the peaks become wider when the photon energy increases.

The same quantities for the simulated data are fitted by the same functions. The results are shown in Figure 5.12 for the neutron channel and Figure 5.14 for the proton channel. The resolution of the simulated data follows the same trend of the experimental data. The peaks also widen at higher energies.

In calculating the missing nucleon mass square, the event photon energy information is needed. As mentioned before in Section5.2.3, there are about 20% of events in the eg3 data having more than one event photon candidate in Tagger according to our event photon selection method by timing. Therefore, we loop through all of the event photon candidates in an event and test their energy matching in the missing nucleon mass cut. A surviving event has at least one event photon candidate satisfying the cut. For most of these multi-hit events, there is one and only one event photon candidate surviving the cut, and we keep the exclusive event and assign that photon as the event photon. In some rare situations, like a few percent, there are are more than one event photon candidate satisfying the cut, we still keep the exclusive event and the event photon is picked randomly. We do not have any other way to distinguish them in these cases, but this will not create much background because their energies are very close to each other.
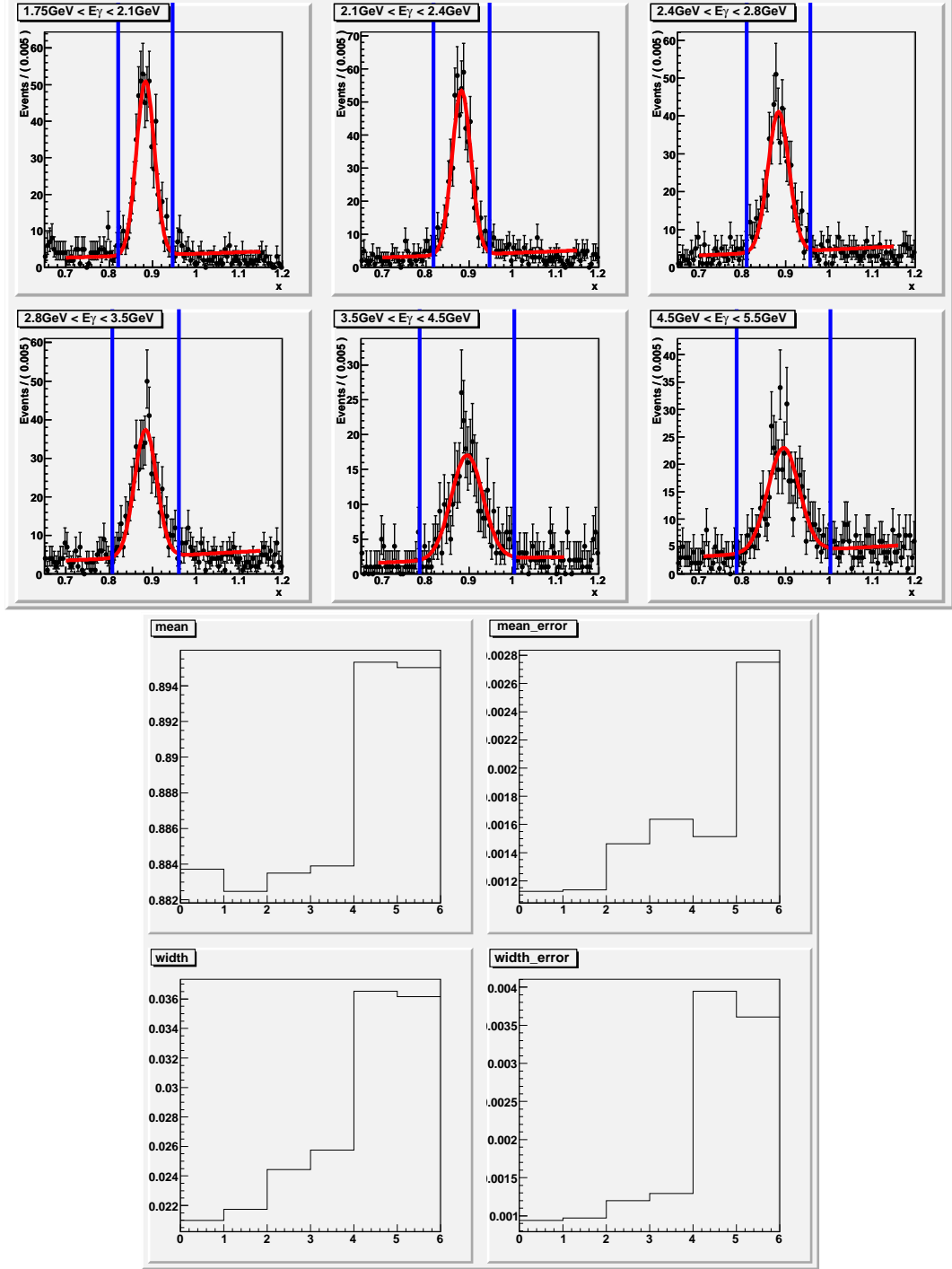
FIGURE 5.11. (**Neutron Channel**) of the experimental data, the fits of $MM_p^2(p\pi^+\pi^-K^-)$ are shown in the upper pad. The resulting means and widths with errors are shown in the lower pad.
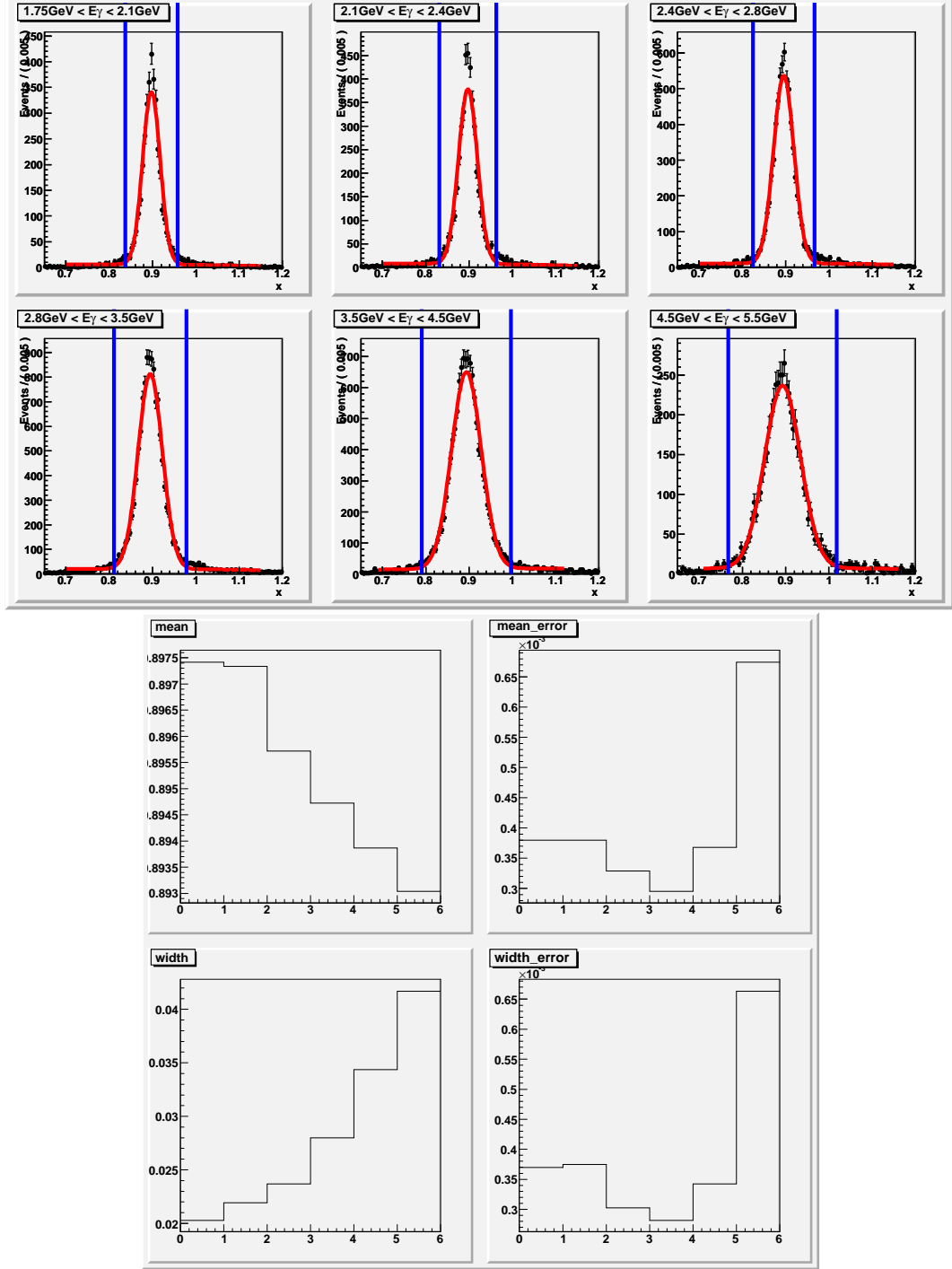
FIGURE 5.12. (**Neutron Channel**) of of the simulated data, the fits of $MM_p^2(p\pi^+\pi^-K^-)$ are shown in the upper pad. The resulting means and widths with errors are shown in the lower pad.

FIGURE 5.13. (**Proton Channel**) of the experimental data, the fits of $MM_n^2(pK^+K^-)$ are shown in the upper pad. The resulting means and widths with errors are shown in the lower pad.
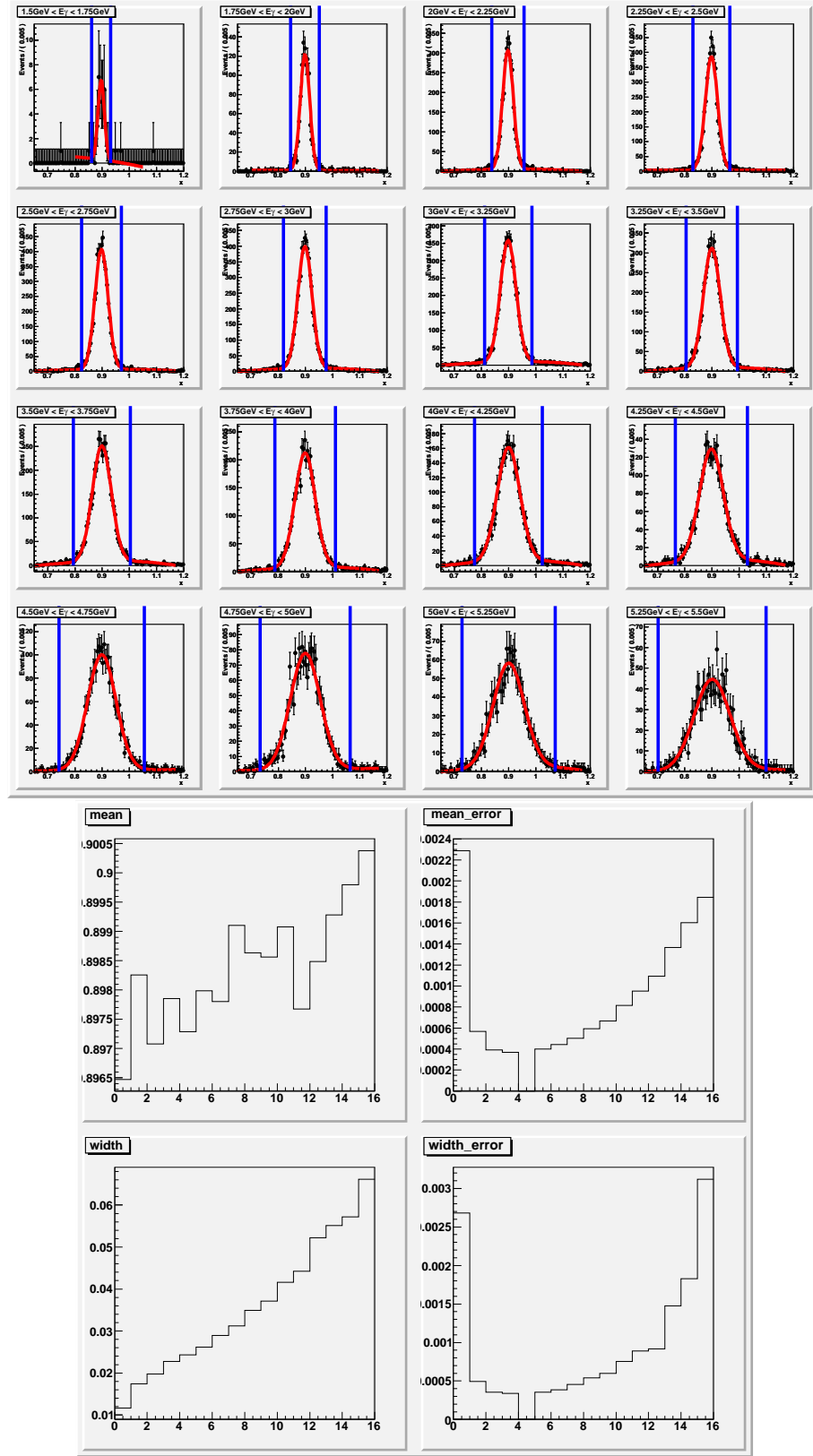
FIGURE 5.14. (**Proton Channel**) of the simulated data, the fits of $MM_n^2(pK^+K^-)$ are shown in the upper pad, The resulting means and widths with errors are shown in the lower pad.

5.7. Missing Nucleon Momentum Cut

To enrich the reactions off quasi-free nucleon, the missing nucleon momenta are required to be small. The corresponding cut is chosen to be 0.2 GeV/c after comparing the experimental and simulated data as shown in Figure 5.15, where they start to deviate from each other.
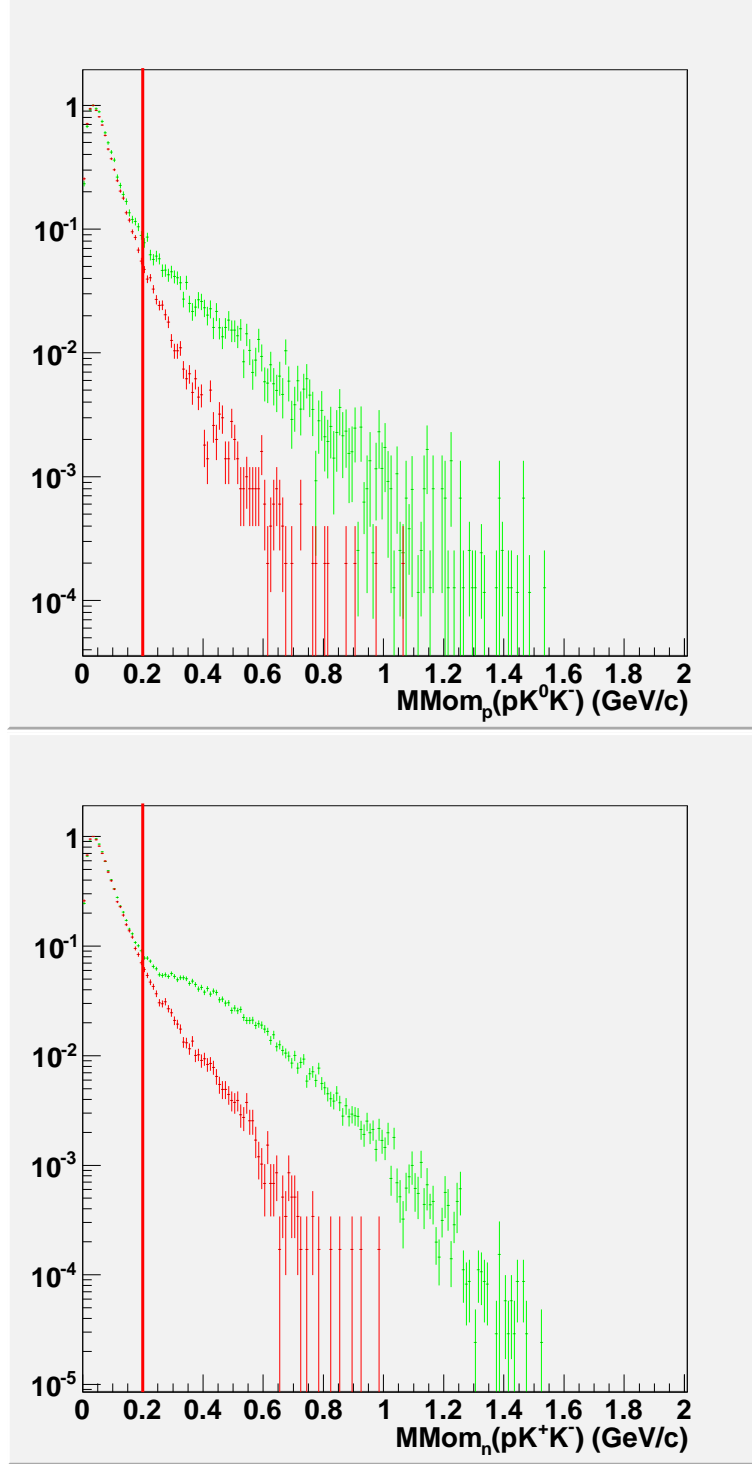
FIGURE 5.15. $MMom_p(pK^0K^-)$ and $MMom_n(pK^+K^-)$ of the experiment (green) and simulation (red). The simulated data are normalized to the experimental data for the comparison. The red lines show where the cuts are.
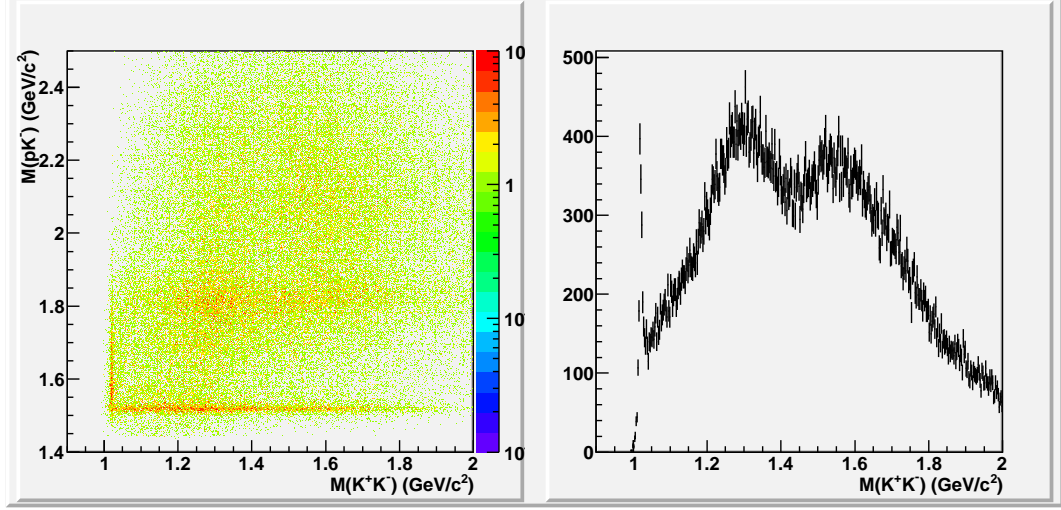
FIGURE 5.16. $M(K^+K^-)$ versus $M(pK^-)$ is shown in the left pad, the mass bands of $\phi(1020)$ and $\Lambda^*(1520)$ are overlapping. $M(K^-K^+)$ is shown in the right pad.

5.8. $\phi(K^+K^-)$ FOR THE PROTON CHANNEL

$\gamma d \to \phi p(n)$ with $\phi(1020) \to K^-K^+$ has the same final state particles as $\Lambda^*(1520)$ production on protons. The $M(K^-K^+)$ after pK^+K^- event selection is shown in the right pad of Figure 5.16. A narrow $\phi(1020)$ resonance is clearly seen. It could be easily cut away if the events with $\phi(1020)$ has no relation with $\Lambda^*(1520)$ production. However, the $\phi(1020)$ production is not necessary a background channel. In the left pad of Figure 5.16, one can see that the $\phi(1020)$ and $\Lambda^*(1520)$ mass distributions are overlapping with each other, which implies that those two narrow resonance may have some interfering effects. We have further investigated the effect and found that it only happens at $E_\gamma < 2.5 GeV$. To test how much $\phi(1020)$ can affect $\Lambda^*(1520)$ yield, we plot $M(pK^-)$ before and after $M(K^+K^-) > 1.05$ cut in Figure 5.17. The $\Lambda^*(1520)$ yield only changes 6% so we decide not cutting any $\phi(1020)$ event away for this study due to the limited statistics at the low energy range.
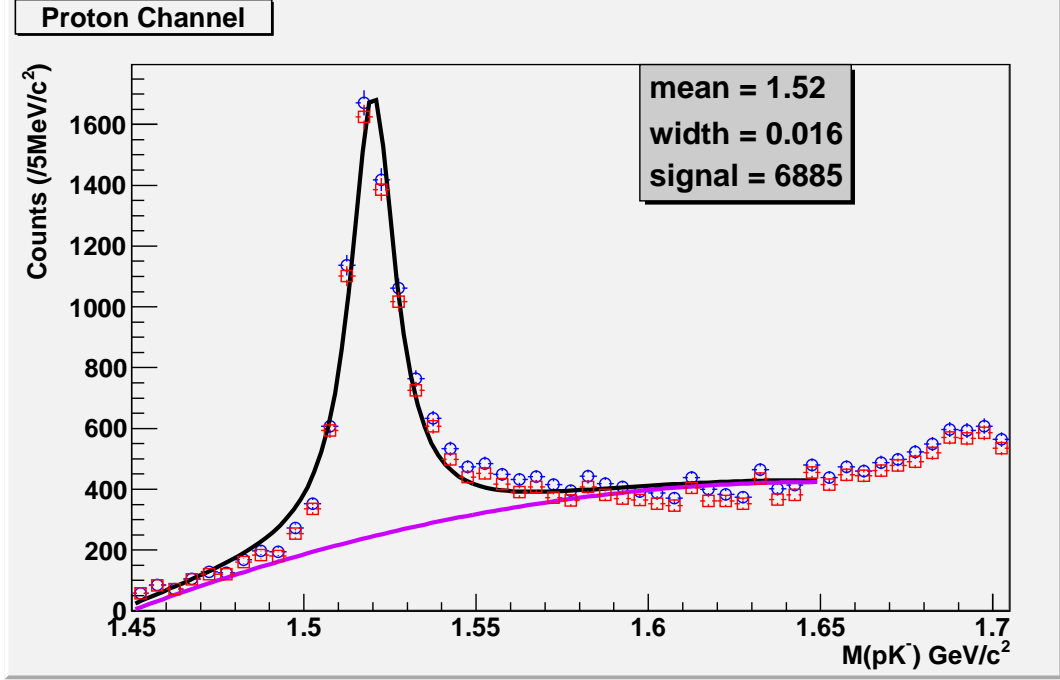
FIGURE 5.17. (**Proton Channel**), invariant mass of $M(pK^-)$ without (blue) and with (red) $\phi(1020)$ cut. The $\Lambda^*(1520)$ yield is estimated by fitting with a Breit-Wigner function as signal plus a polynomial function as background.

5.9. SUMMARY

After analyzing the series of event selection conditions as described above, we have finally isolated the exclusive and quasi-free enriched events of $\gamma d \to pK^+K^-(n)$ for the $\Lambda^*(1520)$ proton channel and $\gamma d \to pK^0K^-(p)$ for the $\Lambda^*(1520)$ neutron channel.

Then $\Lambda^*(1520)$ resonance can be identified by the invariant mass of pK^- as shown in Figure 5.17 for the proton channel and Figure 5.18 for the neutron channel. The two plots show full statistics of the eg3 data set with total $\Lambda^*(1520)$ yields about 6900 and 1100 respectively. The $\Lambda^*(1520)$ mass peaks are around the PDG mass 1.52 GeV with a width of about 16 MeV.
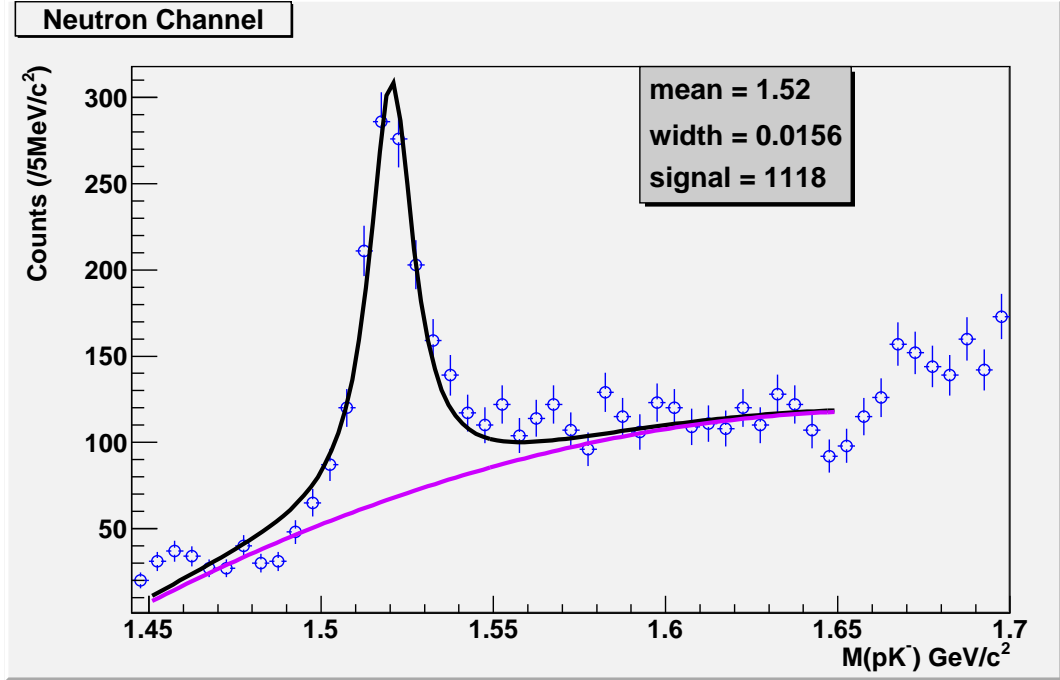
FIGURE 5.18. (**Neutron Channel**), invariant mass of $M(pK^-)$. The $\Lambda^*(1520)$ yield is estimated by fitting with a Breit-Wigner function as signal plus a polynomial function as background.

CHAPTER 6

CROSS SECTION AND DECAY ANGLE

6.1. INTRODUCTION

In scattering theory, the likelihood of a particular reaction happening is defined as the cross section. The name originates from classical theory, where the probability of a reaction is simply the ratio between the total cross-sectional area of all incoming objects and that of the target. It can be generally written as

$$\sigma = \frac{N_{reaction}}{N_{incoming} \cdot \frac{N_{target}}{A}} \tag{6.1}$$

where σ is the reaction cross section, $N_{reaction}$ is the number of reactions , $N_{incoming}$ is the number of incoming particles and $\frac{N_{target}}{A}$ is the target particle area density.

Practically, in a subatomic particle scattering experiment, the cross section evaluation involves much more than counting the number of reactions. First, the reaction events of interest need to be extracted when all kinds of backgrounds are present. Second, the detector acceptance needs to be fully understood, so that the acceptance corrected $N_{reaction}$ can be obtained. Third, the very large number of incoming particles and thus the high luminosity are not easy to be determined with the demanded precision.

Generally the cross sections of a reaction can depend on the reaction mechanism as well as the internal structures of both incoming particles and target particles. Furthermore the cross sections can also depend on the kinematic regions where individual events occur. eg3 used an unpolarized photon beam and unpolarized target. For both of the reactions of interest, $\gamma d \to K^+ \Lambda^*(n)$ and $\gamma d \to K^0 \Lambda^*(p)$, the kinematics can

be described by two independent variables based on the momentum and energy conservations. We have chosen two different pairs in this study.

1. The photon energy E_γ and $t^* = -(t - t_0)$, where $t = (p_\gamma - p_{K^+/K^0})^2$ is the Lorentz-invariant four momentum transfer from photon to K^+/K^0 and t_0 is the minimum of absolute value of t [1].

2. The photon energy E_γ and $\theta_{K^+}^{CM}$ or $\theta_{K^0}^{CM}$, which are the meson polar angles in the center of mass frame of the $\gamma + nucleon$ system for the proton and neutron channels respectively.

When considering the Λ^* decay, one more variable is needed to describe the full kinematics. We use the decay K^- polar angle in the Gottfried-Jackson frame $cos\theta_{K^-}^{GJ}$ as the third one. Ideally, we should investigate our data in three kinematic variables, but due to the limited statistics, we choose to bin data only in $E(\gamma)$ and $cos\theta_{K^-}^{GJ}$ bins.

At a single kinematic bin, the differential cross section of a particular reaction is given by

$$\frac{d\sigma_{ij}}{dA} = \frac{1}{L_i} \frac{Y_{ij}}{a_{ij} f_{br}} \frac{1}{\Delta A_j} \tag{6.2}$$

where A is the other kinematic variable besides E_γ, L_i is the luminosity in the E_γ bin i, f_{br} is the branching ratio, Y_{ij} and a_{ij} are the experimental yield and the Monte Carlo acceptance in the photon energy bin i and the A bin j and ΔA_j is A_j bin size. Please note that the assumption here is that in such a single kinematic bin, the simulation can mimic the experiment very well. This is usually not a hard requirement as long as we choose the binning to be small enough, so that neither the experimental data nor simulated data varies a lot within the bin.

For the E_γ bin i, the total cross section can be obtained from the formula similar to a differential cross section above only if the simulation can mimic the experiment well in all ranges of the kinematic variable A. This is usually a much harder requirement and needs much more delicate Monte Carlo tuning. An alternative way to obtain the total cross section is to fit the differential cross sections $\frac{d\sigma_{ij}}{dA}$ in the E_γ bin i with a

function f_i and integrate over A to get the total cross section by

$$\sigma_i = \int f_i(\frac{d\sigma_{ij}}{dA})dA \tag{6.3}$$

6.2. LUMINOSITY

The integrated luminosity per photon energy bin $E_{\gamma i}$ is given by

$$L_i = \frac{N_i \, \rho_D \, L_T \, N_A}{A_D} \tag{6.4}$$

where N_i is the integrated number of photons on target in a given photon energy bin, $\rho_D = 0.169g/cm^3$ is the density of liquid deuterium, $L_T = 40cm$ is the length of the eg3 target, $N_A = 6.02 \times 10^{23} deuterons/mole$ is Avogadro's number, and $A_D = 2.014g/mole$ is the molar mass of deuterium [1].

The photon flux N_i is obtained with the GFLUX package [32]. The idea of the method is to use the out-of-time photons, which do not produce the recorded events, to calculate the rate corresponding to each T-Counter. This rate is then corrected by a factor which is determined during test runs and accounts for the photon loss between the tagger and the target. Then the rate is multiplied with the live time, the sum of small intervals during which the rates are consistent with each other within statistical errors. Figure 6.1 shows the number of the photons per photon energy bin corresponding to the data set analyzed. The typical uncertainties reported by GFLUX package for a single energy bin is on the order of $\sim 2\%$.

The tagger counter efficiency correction, detector livetime correction, and beam trip cut are automatically taken care of by applying the GLFUX result to the experimental data, because their algorithms in the GLFUX and cooking/analysis procedure are the same.
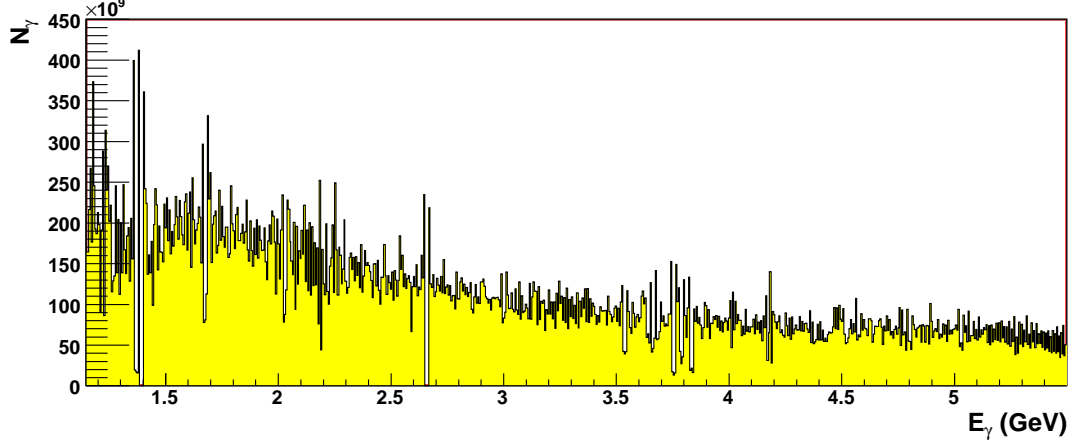
FIGURE 6.1. Number of photons per tagger energy bin versus corresponding photon energy.

6.3. BRANCHING RATIO

The branching ratio f_{br} depends on what topology is studied and how the simulation is carried out (see Section 3). For the proton channel, $f_{br} = 0.225$ is from $\Lambda^* \to pK^-$. For the neutron channel, $f_{br} = 0.225 \times (0.5 \times 0.69)$, where 0.225 is from $\Lambda^* \to pK^-$ and (0.5×0.69) is from $K^0 \to K_s \to \pi^+\pi^-$ [1].

6.4. KINEMATIC BINNING

The actual kinematic binning is determined by examining the statistical distribution of event candidates over various kinematic variables. The event candidates are selected by the cut 1.45 GeV $< M(pK^-) <$ 1.59 GeV. They are close to the actual $\Lambda^*(1520)$ yields because the background contribution is relatively small.

The binning should ensure that each bin is small enough so that the data does not vary much and large enough so that there are enough events per bin to enable the $\Lambda^*(1520)$ yield extraction by fitting. The final binning is shown with all bin edges in Table 6.1. Both the event candidate distribution in the experimental and simulated data are shown in the Figures 6.1 - 6.6 as indicated in Table 6.2. Generally the simulation has similar kinematic distributions to those of the experiment. This indicates that the simulation conditions match the experiment reasonably well.

TABLE 6.1. Edge of kinematic binning

kinematic variable	proton channel
E_γ	from 1.75 GeV to 5.50 GeV, 0.25 GeV bin width, 16 bins
t^*	$\{0.25,0.35,0.55,0.95,1.3,1.8,3.0\}(GeV^2/c^4)$, 6 bins
$\theta_{K^+}^{CM}$	$\{40,50,60,70,80,100,120\}$(deg), 6 bins
$cos\theta_{K^-}^{GJ}$	$\{-0.8,-0.5,-0.2,0.1,0.4,0.6,0.9\}$, 6 bins
kinematic variable	neutron channel
E_γ	$\{1.75,2.1,2.4,2.8,3.5,4.5,5.5\}$(GeV), 6 bins
t^*	$\{0.0,0.25,0.5,0.8,1.2,1.8,3.0\}$(GeV^2/c^4), 6 bins
$\theta_{K^0}^{CM}$	$\{20,40,50,60,80,100,120\}$(deg), 6 bins
$cos\theta_{K^-}^{GJ}$	$\{-0.8,-0.5,-0.2,0.1,0.4,0.6,0.9\}$, 6 bins

TABLE 6.2. Kinematic binning plots

	E_γ (proton)	E_γ (neutron)
t^*	Figure 6.2	Figure 6.3
θ_{K^+/K^0}^{CM}	Figure 6.4	Figure 6.5
$cos\theta_{K^-}^{GJ}$	Figure 6.6	Figure 6.7

For the proton channel, most of the reactions happen at low energies around 2 GeV which is just above the threshold $E_\gamma = 1.7$ GeV. The t^* distribution has largest contribution below 1 GeV^2 and can only reach 0.25 GeV^2 because a very forward K^+ going through the CLAS front hole is not detected. The $\theta_{K^+}^{CM}$ distribution only covers from 40° to 120° and mostly focuses at forward angles. Here the 40° is the most forward angle in the center of mass frame where the K^+ can be detected. The $cos\theta_{K^-}^{GJ}$ has a relatively even distribution over all angles.

For the neutron channel, most of the reactions also happen at low energies around 2 GeV. The t^* distribution has largest contribution below 1 GeV^2 and can only reach 0 GeV^2 because the forward K^0 going toward the CLAS front hole can be reconstructed by the detected $\pi^+\pi^-$ which are not going through the hole. The $\theta_{K^0}^{CM}$ distribution covers from 20° to 120° and mostly focuses at forward angles. Here the 20° is most forward angle in the center of mass frame where the K^0 can be reconstructed. The $cos\theta_{K^-}^{GJ}$ has a relatively even distribution over all angles.
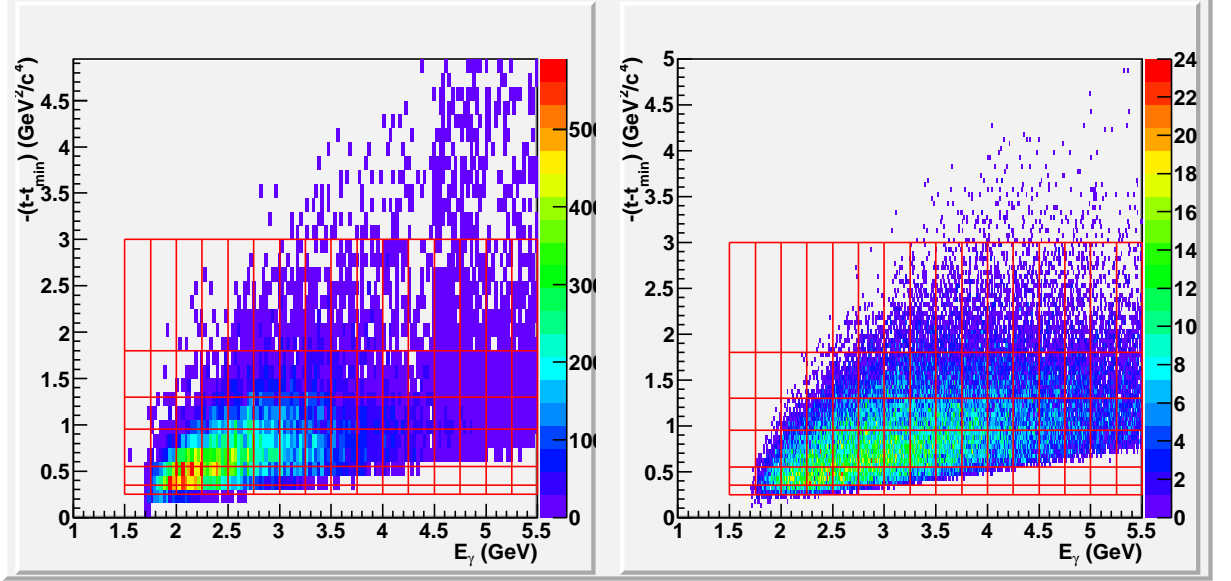
FIGURE 6.2. (**Proton Channel**), $\Lambda^*(1520)$ candidate distribution over E_γ and t^* for the experiment (left) and simulation (right). The red boxes show where the binning boundaries are.
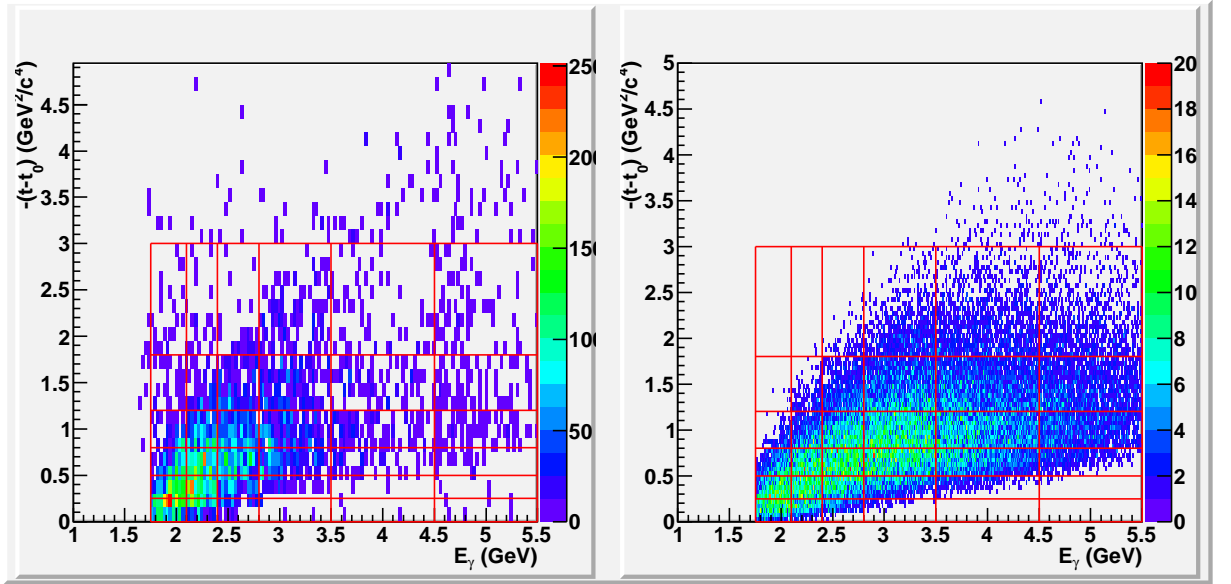
FIGURE 6.3. (**Neutron Channel**), $\Lambda^*(1520)$ candidate distribution over E_γ and t^* for the experiment (left) and simulation (right). The red boxes show where the binning boundaries are.
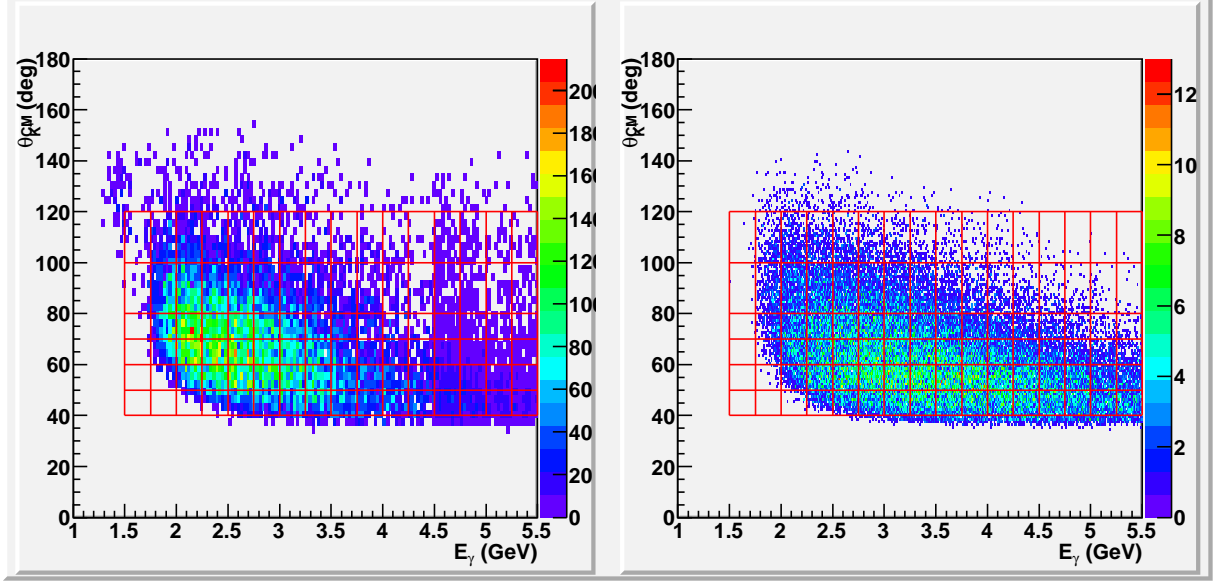
FIGURE 6.4. (**Proton Channel**), $\Lambda^*(1520)$ candidate distribution over E_γ and $\theta_{K^+}^{CM}$ for the experiment (left) and simulation (right). The red boxes show where the binning boundaries are.
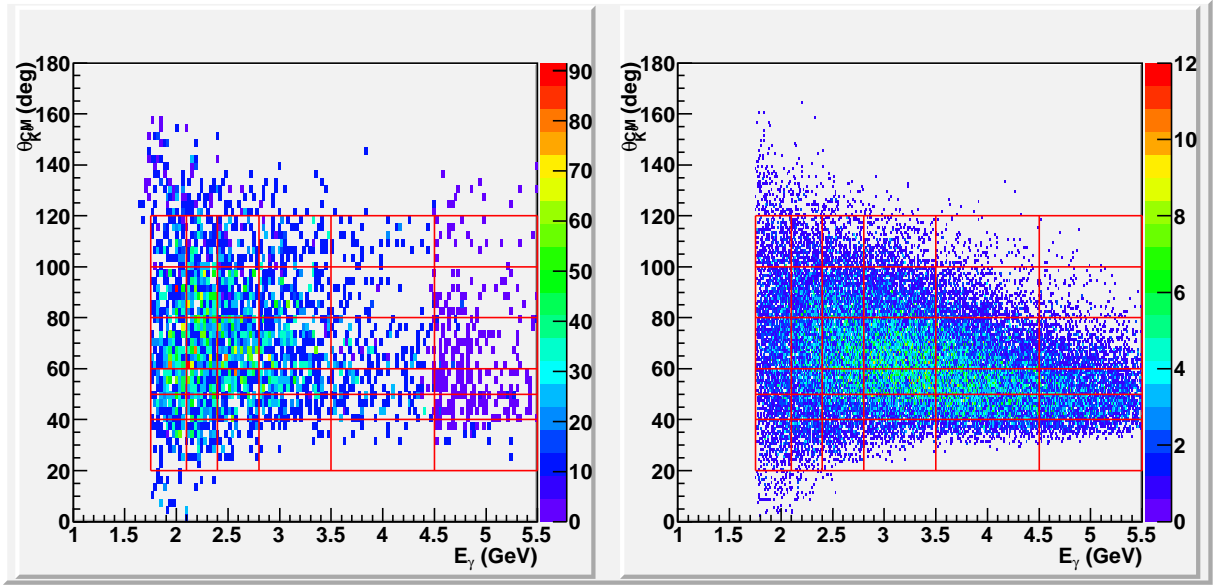
FIGURE 6.5. (**Neutron Channel**), $\Lambda^*(1520)$ candidate distribution over E_γ and $\theta_{K^0}^{CM}$ for the experiment (left) and simulation (right). The red boxes show where the binning boundaries are.

FIGURE 6.6. (**Proton Channel**), $\Lambda^*(1520)$ candidate distribution over E_γ and $cos\theta^{GJ}_{K^-}$ for the experiment (left) and simulation (right). The red boxes show where the binning boundaries are.

FIGURE 6.7. (**Neutron Channel**), $\Lambda^*(1520)$ candidate distribution over E_γ and $cos\theta^{GJ}_{K^-}$ for the experiment (left) and simulation (right). The red boxes show where the binning boundaries are.
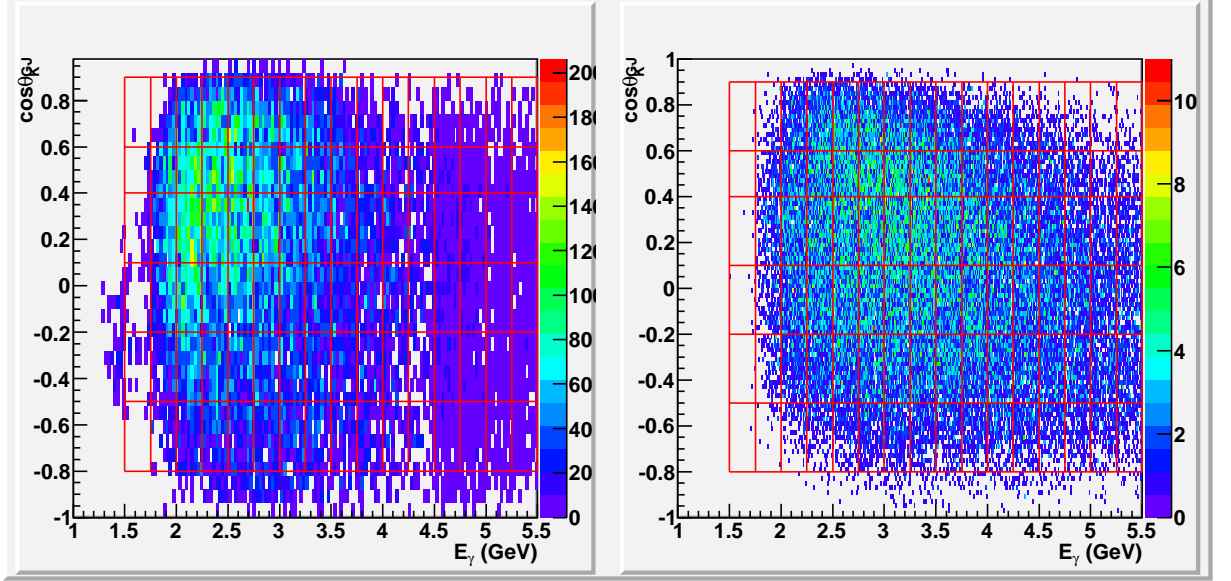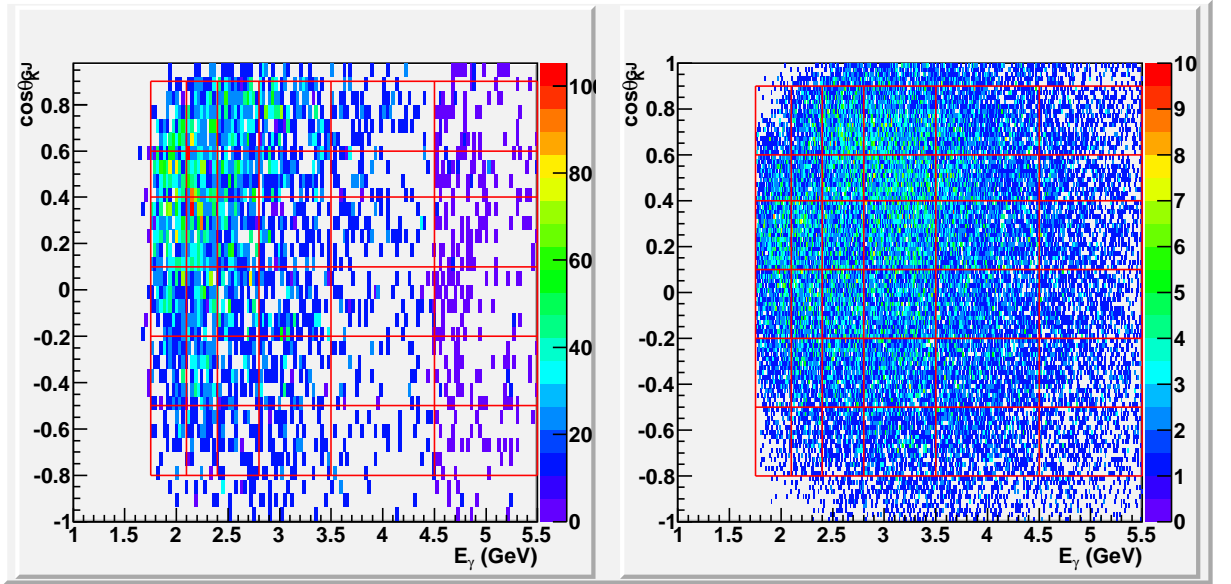
TABLE 6.3. Yield extraction plots

kinematic binning (proton)	$M(pK^-)$	yield vs. A at E_γ	yield vs. E_γ at A
E_γ and t^*	Figure 6.8	Figure 6.9	Figure 6.10
E_γ and $\theta_{K^+}^{CM}$	Figure 6.14	Figure 6.15	Figure 6.16
E_γ and $cos\theta_{K^-}^{GJ}$	Figure 6.20	Figure 6.21	Figure 6.22
kinematic binning (neutron)	$M(pK^-)$	yield vs. A at E_γ	yield vs. E_γ at A
E_γ and t^*	Figure 6.11	Figure 6.12	Figure 6.13
E_γ and $\theta_{K^0}^{CM}$	Figure 6.17	Figure 6.18	Figure 6.19
E_γ and $cos\theta_{K^-}^{GJ}$	Figure 6.23	Figure 6.24	Figure 6.25

6.5. YIELD EXTRACTION

In every kinematic bin, the invariant mass $M(pK^-)$ histogram is fitted to extract the $\Lambda^*(1520)$ yield. For the experimental data, the fitting function is chosen to be a Breit-Wigner function as signal plus a polynomial function as background. For most of the kinematic bins, the statistics are fairly low and we use maximum likelihood as the fit method without any parameter fixed. The $M(pK^-)$ histograms with fit functions and $\Lambda^*(1520)$ yields from fitting are shown in the Figure. 6.7 - 6.24 as indicated in Table 6.3 for various combinations of kinematic variables. For the simulated data, only a Breit-Wigner function is used because we did not simulate any background. The fitting of the simulated data is not shown because they are well described distributions with high statistics and have small fitting errors.
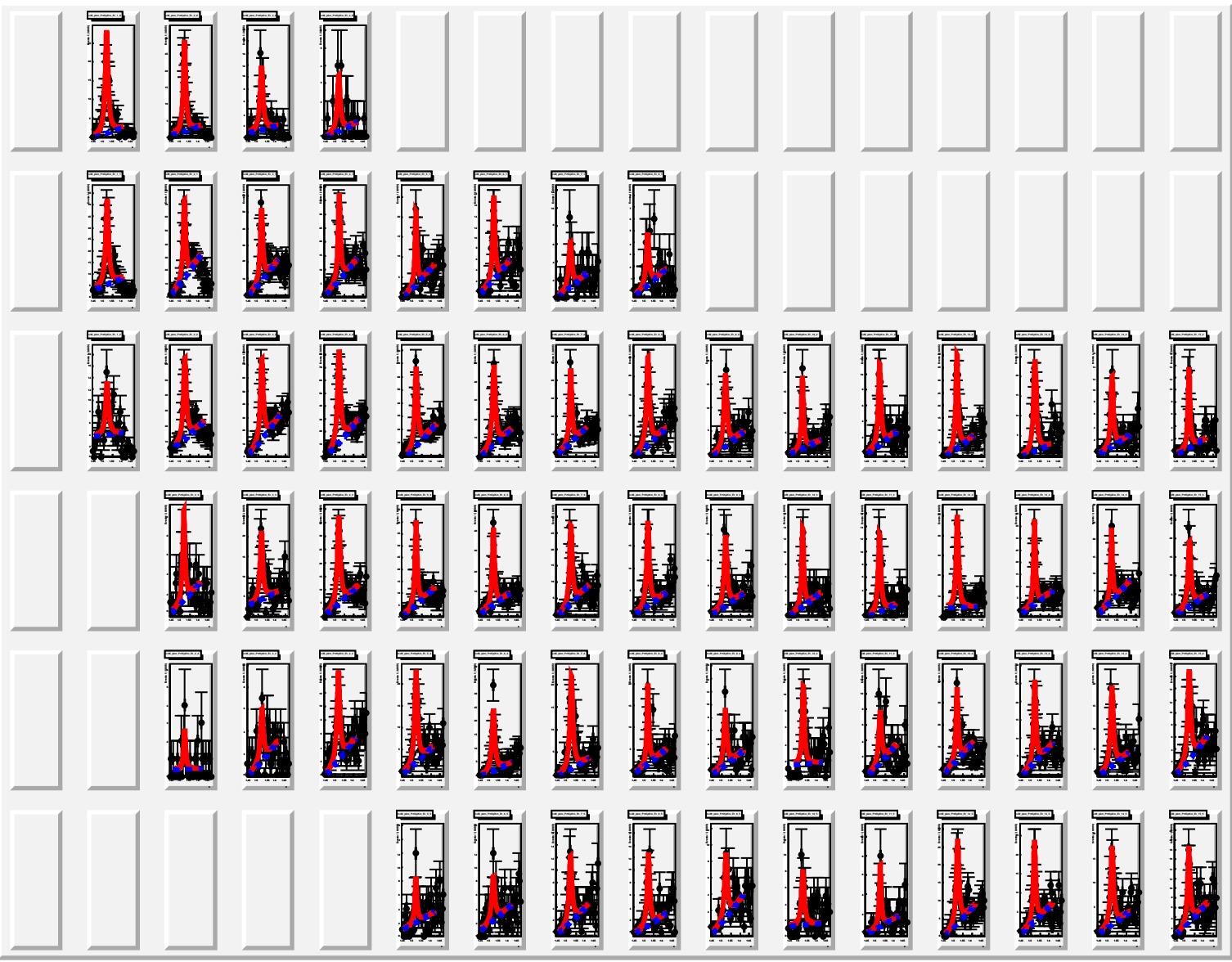
FIGURE 6.8. (**Proton Channel**), $M(pK^-)$ at different E_γ and t^* bins with fitting functions. E_γ rises from left to right pads and t^* increases from top to bottom pads.
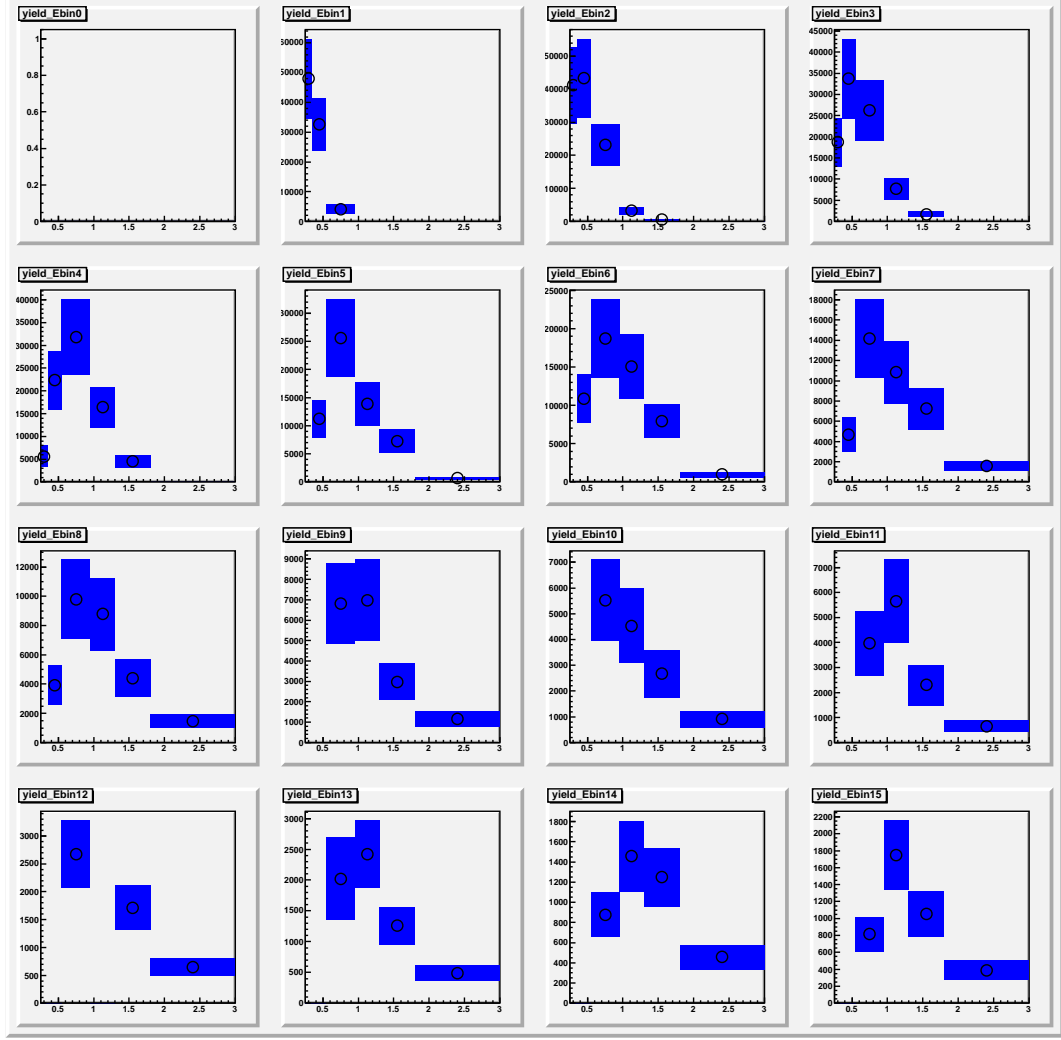
FIGURE 6.9. (**Proton Channel**), $\Lambda^*(1520)$ yield distribution over t^* at different E_γ bins. E_γ rises from left to right pads.
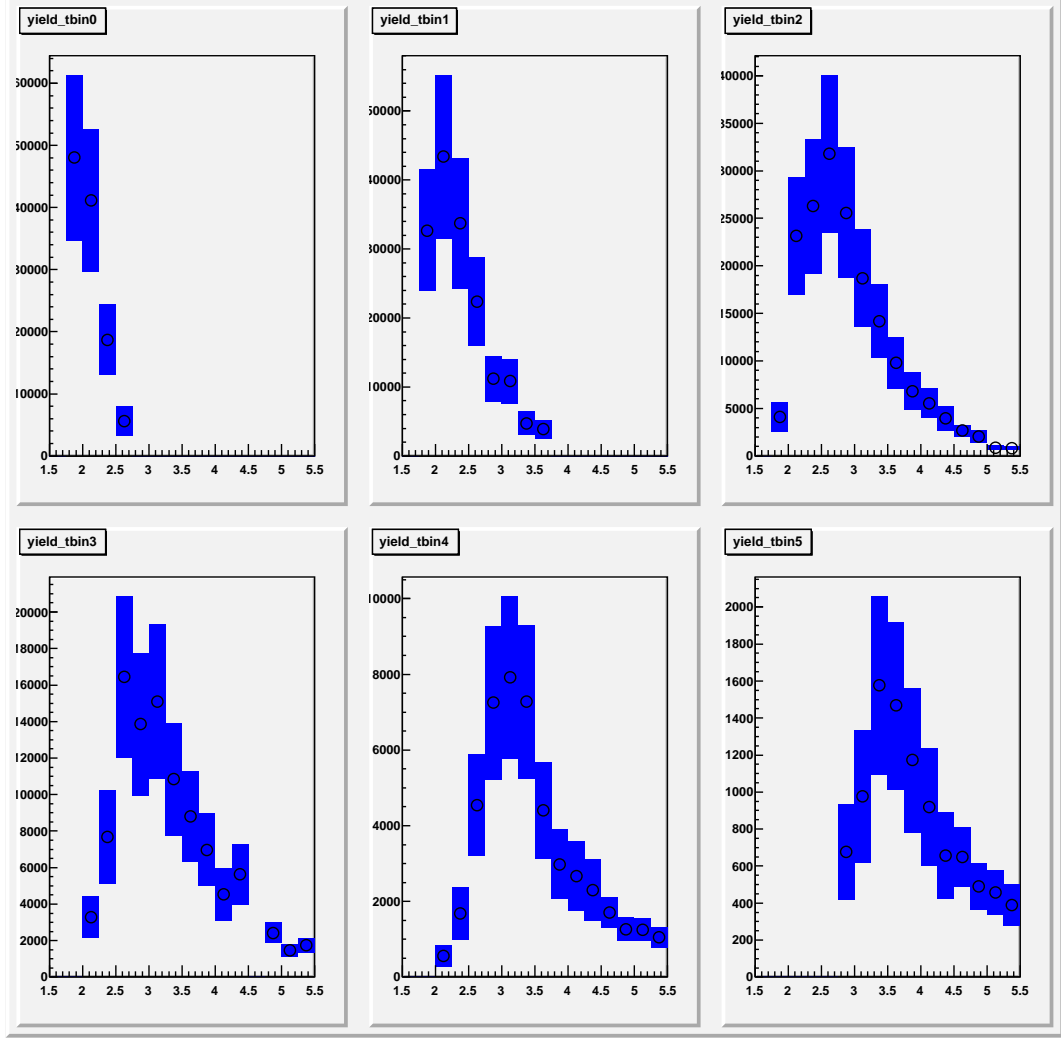
FIGURE 6.10. (**Proton Channel**), $\Lambda^*(1520)$ yield distribution over E_γ at different t^* bins. t^* increases from top to bottom pads.

FIGURE 6.11. (**Neutron Channel**), $M(pK^-)$ at different E_γ and t^* bins with fitting functions. E_γ rises from left to right pads and t^* increases from top to bottom pads.
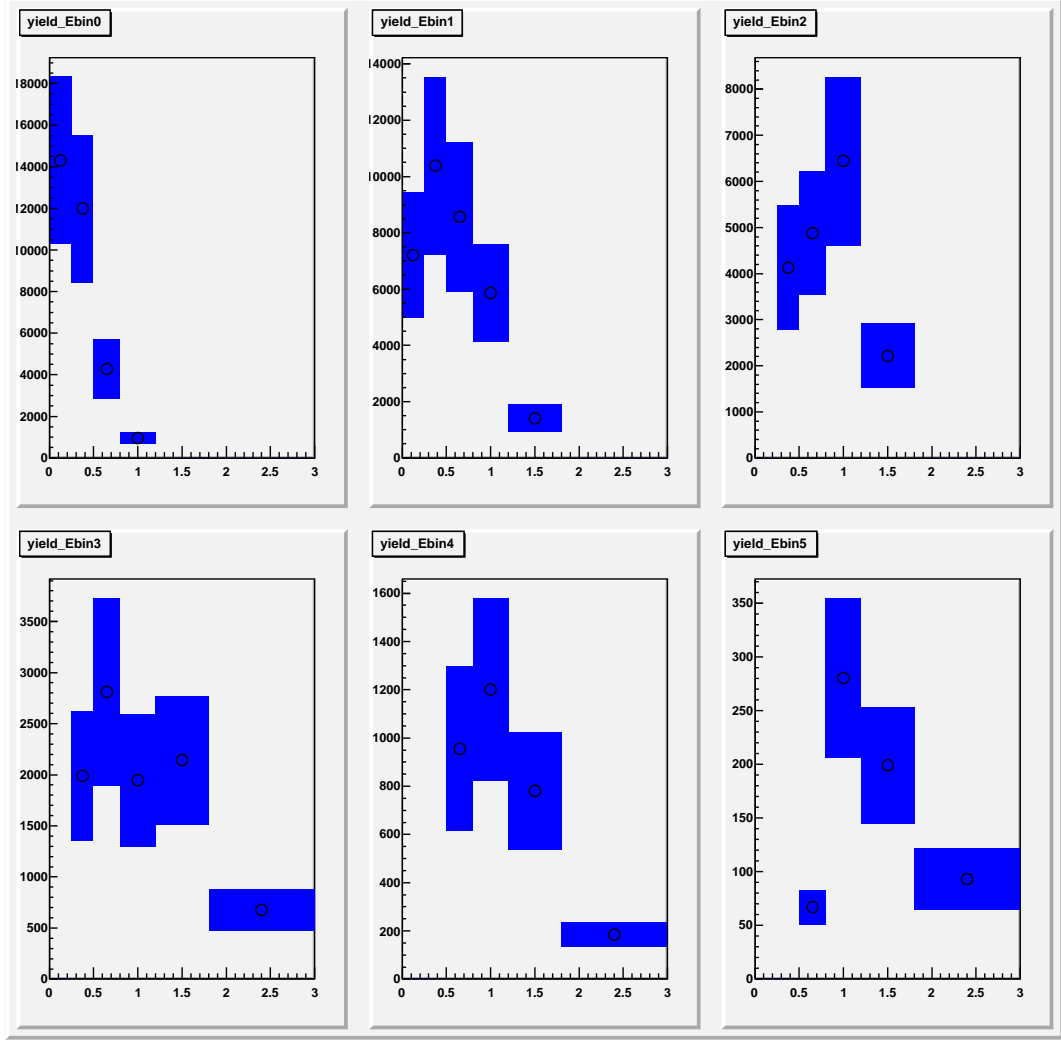
FIGURE 6.12. (**Neutron Channel**), $\Lambda^*(1520)$ yield distribution over t^* at different E_γ bins. E_γ rises from left to right pads.
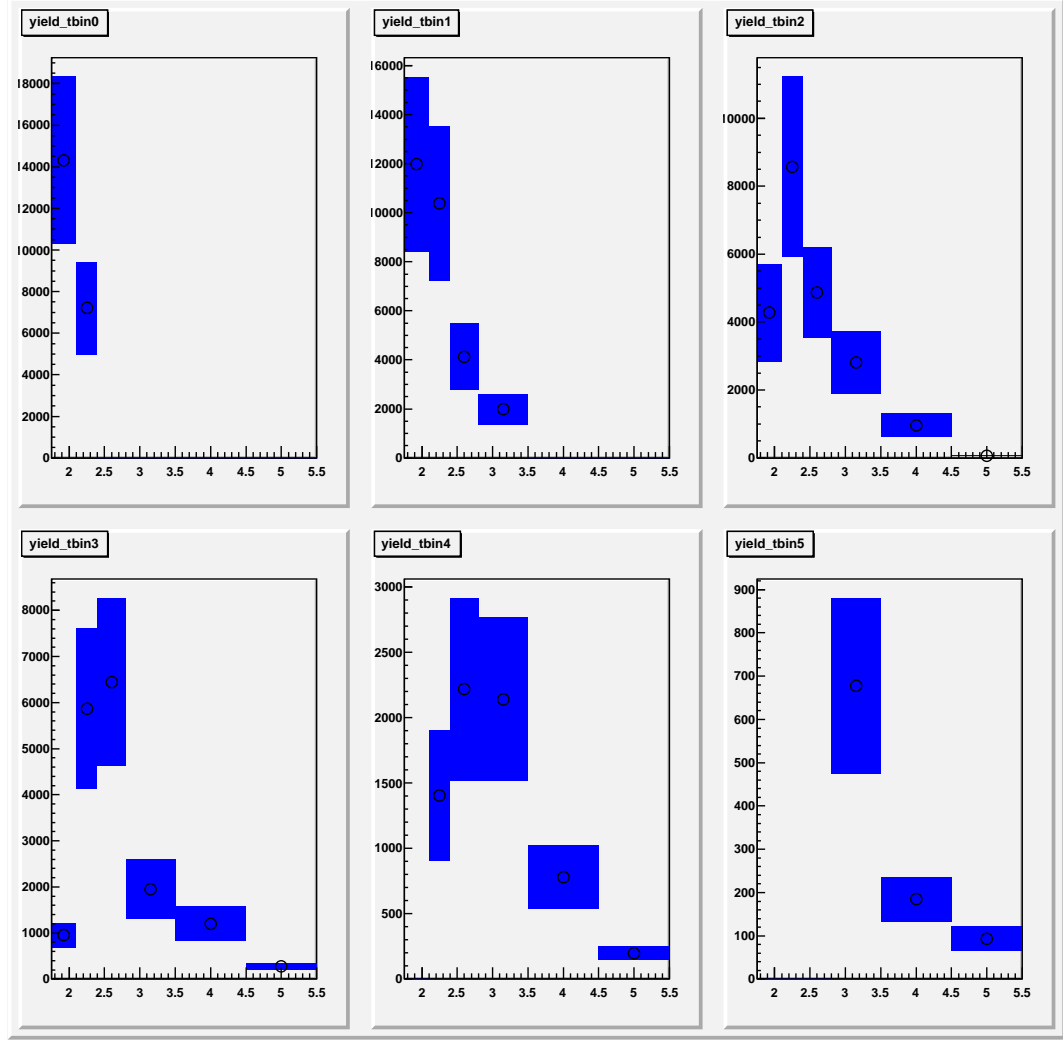
FIGURE 6.13. (**Neutron Channel**), $\Lambda^*(1520)$ yield distribution over E_γ at different t^* bins. t^* increases from top to bottom pads.
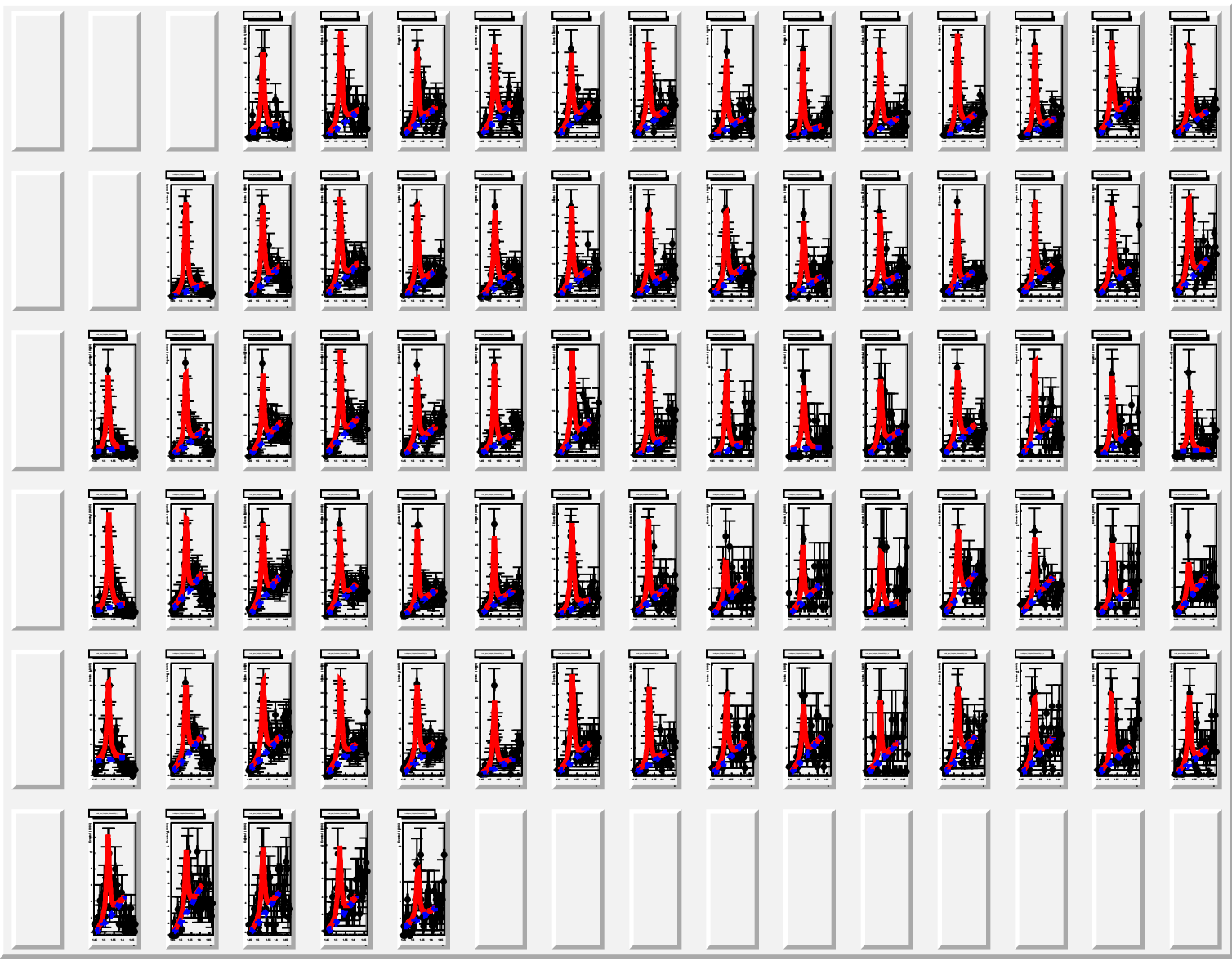
FIGURE 6.14. (**Proton Channel**), $M(pK^-)$ at different E_γ and $\theta_{K^+}^{CM}$ bins with fitting functions. E_γ rises from left to right pads and $\theta_{K^+}^{CM}$ increases from top to bottom pads.

FIGURE 6.15. (**Proton Channel**), $\Lambda^*(1520)$ yield distribution over $\theta_{K^+}^{CM}$ at different E_γ bins. E_γ rises from left to right pads.

FIGURE 6.16. (**Proton Channel**), $\Lambda^*(1520)$ yield distribution over E_γ at different $\theta_{K^+}^{CM}$ bins. $\theta_{K^+}^{CM}$ increases from top to bottom pads.
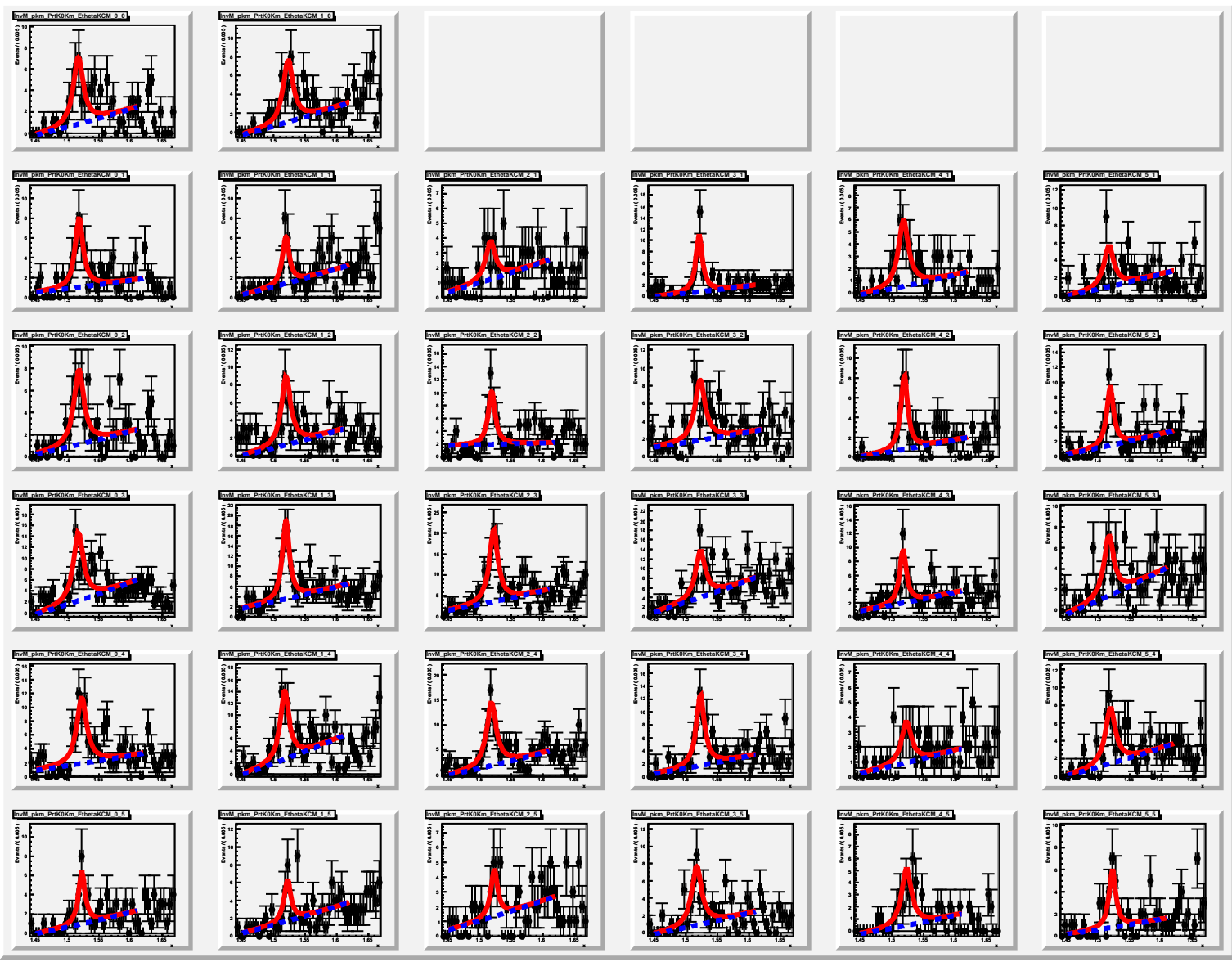
FIGURE 6.17. (Neutron Channel), $M(pK^-)$ at different E_γ and $\theta_{K^0}^{CM}$ bins with fitting functions. E_γ rises from left to right pads and $\theta_{K^0}^{CM}$ increases from top to bottom pads.
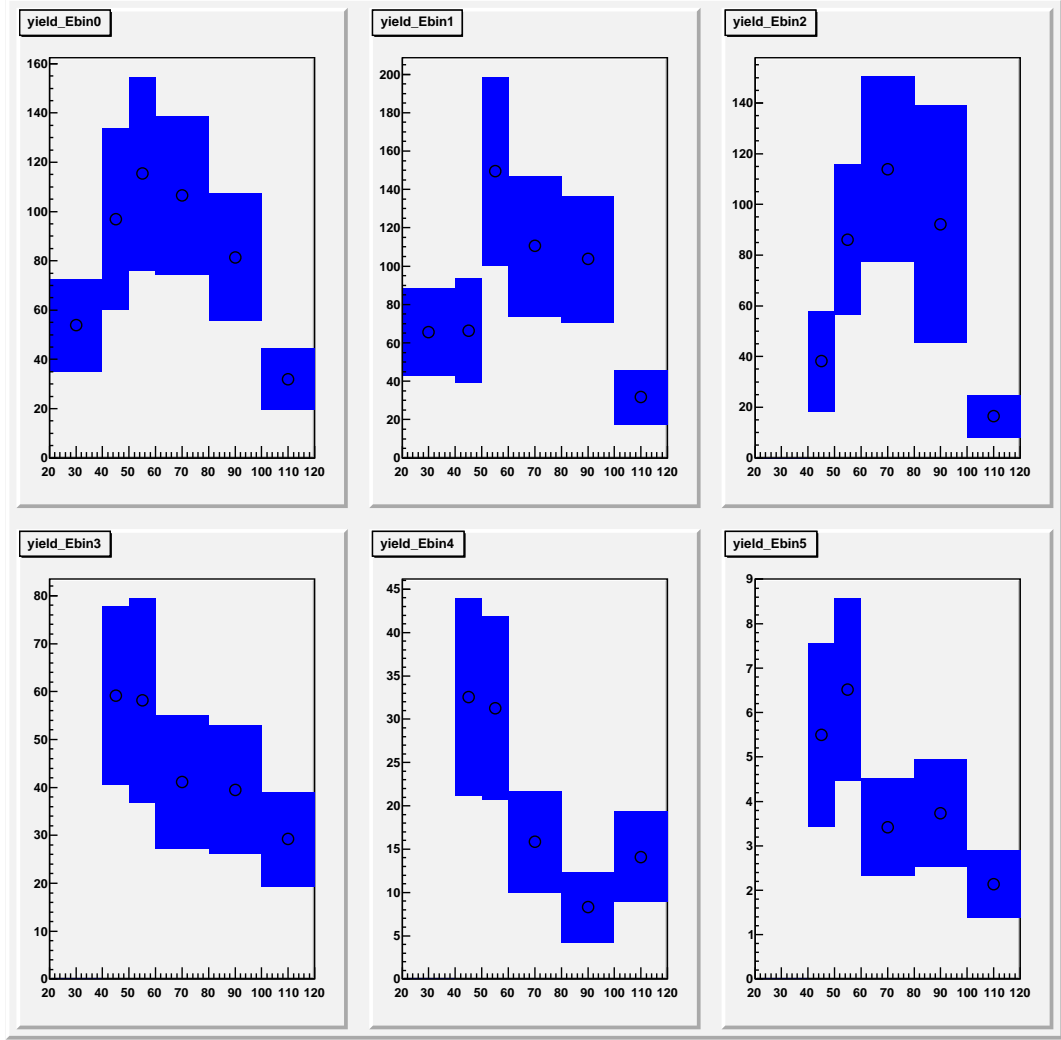
FIGURE 6.18. (**Neutron Channel**), $\Lambda^*(1520)$ yield distribution over $\theta_{K^0}^{CM}$ at different E_γ bins. E_γ rises from left to right pads.
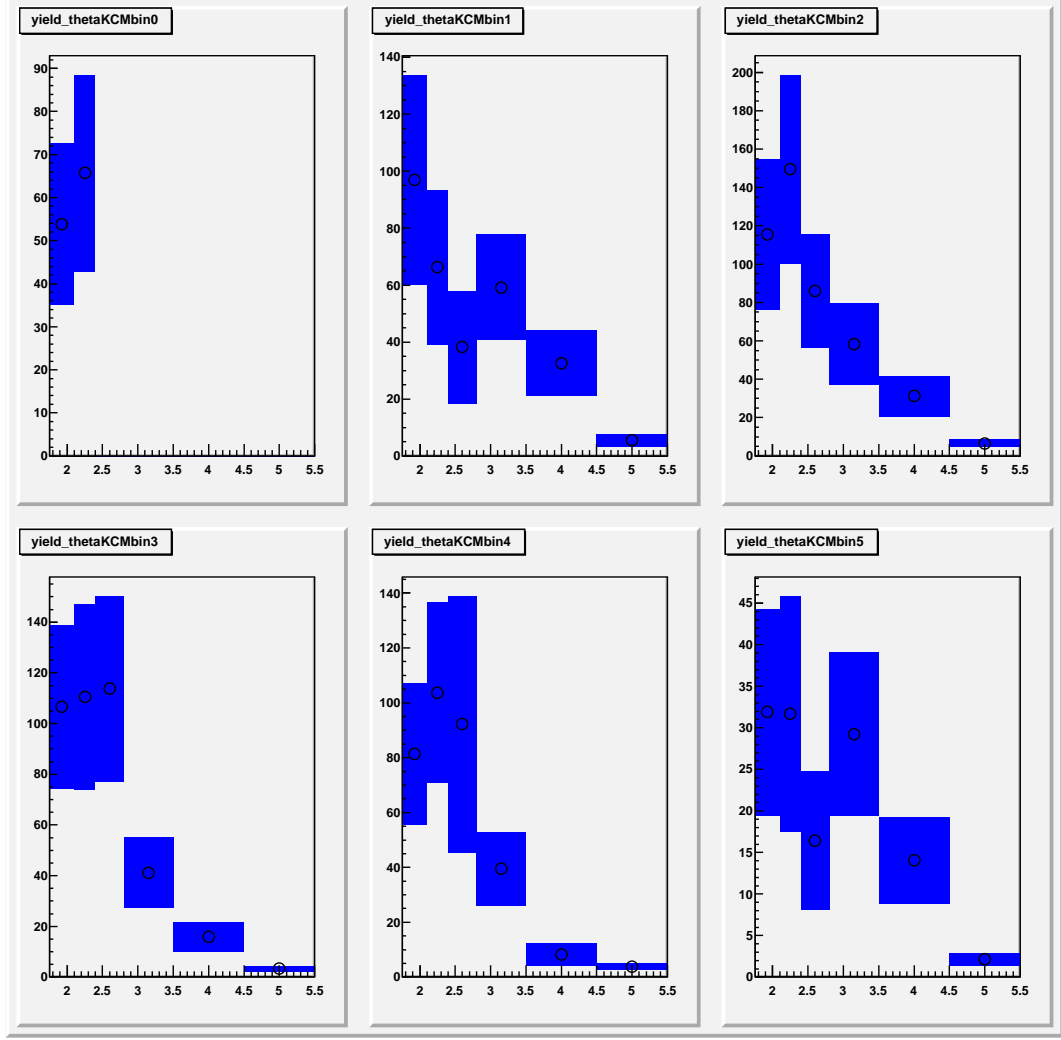
FIGURE 6.19. (**Neutron Channel**), $\Lambda^*(1520)$ yield distribution over E_γ at different $\theta_{K^0}^{CM}$ bins. $\theta_{K^0}^{CM}$ increases from top to bottom pads.
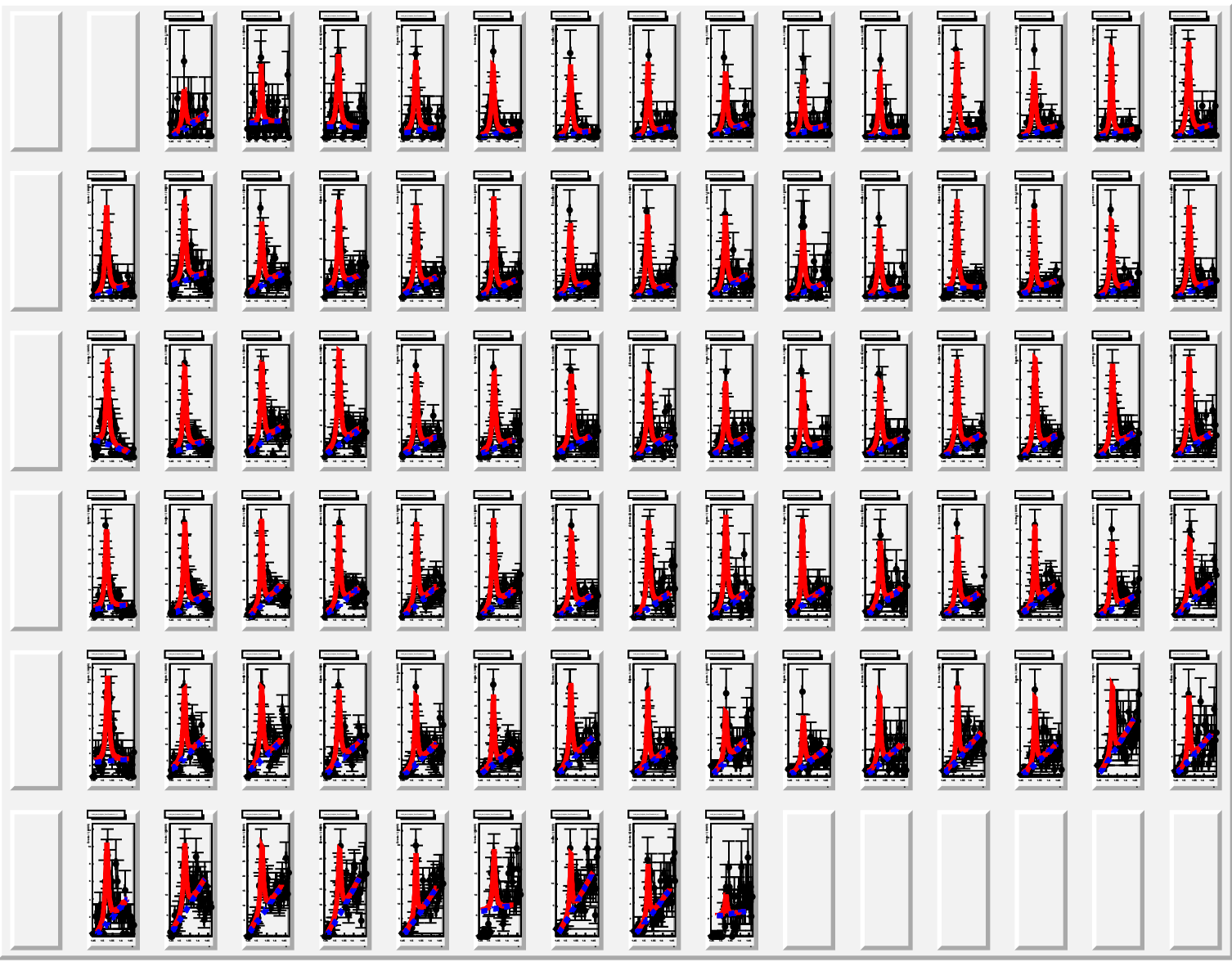
FIGURE 6.20. (**Proton Channel**), $M(pK^-)$ at different E_γ and $cos\theta_{K^-}^{GJ}$ bins with fitting functions. E_γ rises from left to right pads and $\theta_{K^-}^{GJ}$ increases from top to bottom pads.
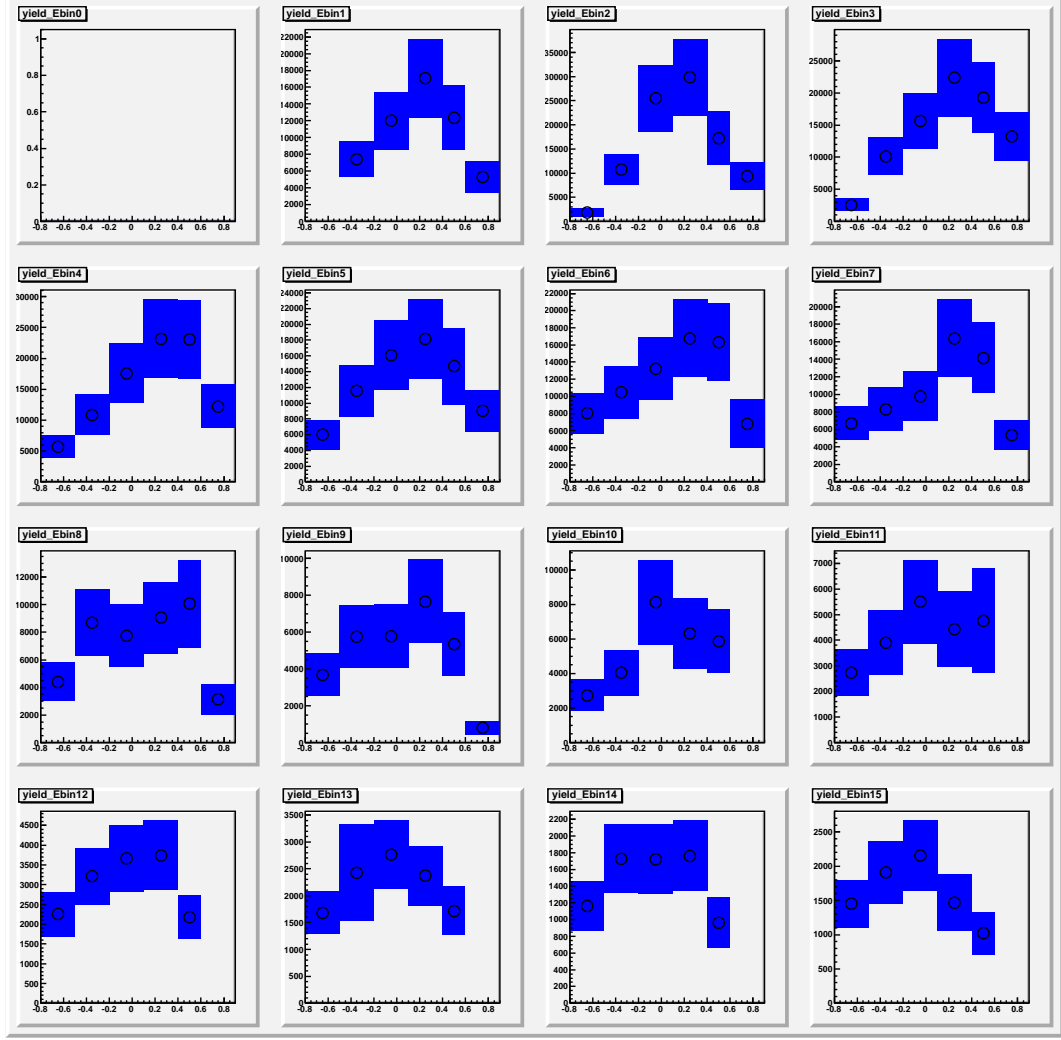
FIGURE 6.21. (**Proton Channel**), $\Lambda^*(1520)$ yield distribution over $cos\theta_{K^-}^{GJ}$ at different E_γ bins. E_γ rises from left to right pads.
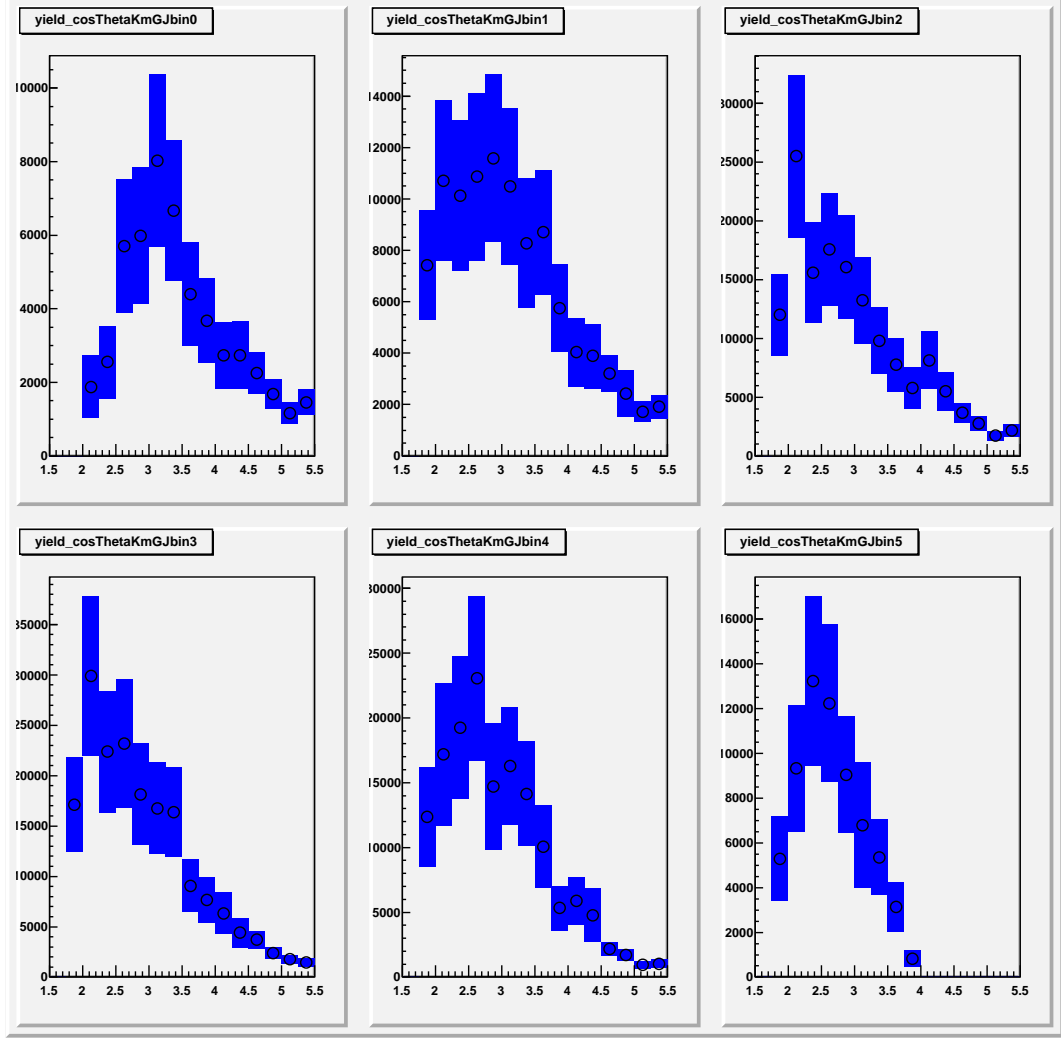
FIGURE 6.22. (**Proton Channel**), $\Lambda^*(1520)$ yield distribution over E_γ at different $cos\theta_{K^-}^{GJ}$ bins. $\theta_{K^-}^{GJ}$ increases from top to bottom pads.

94
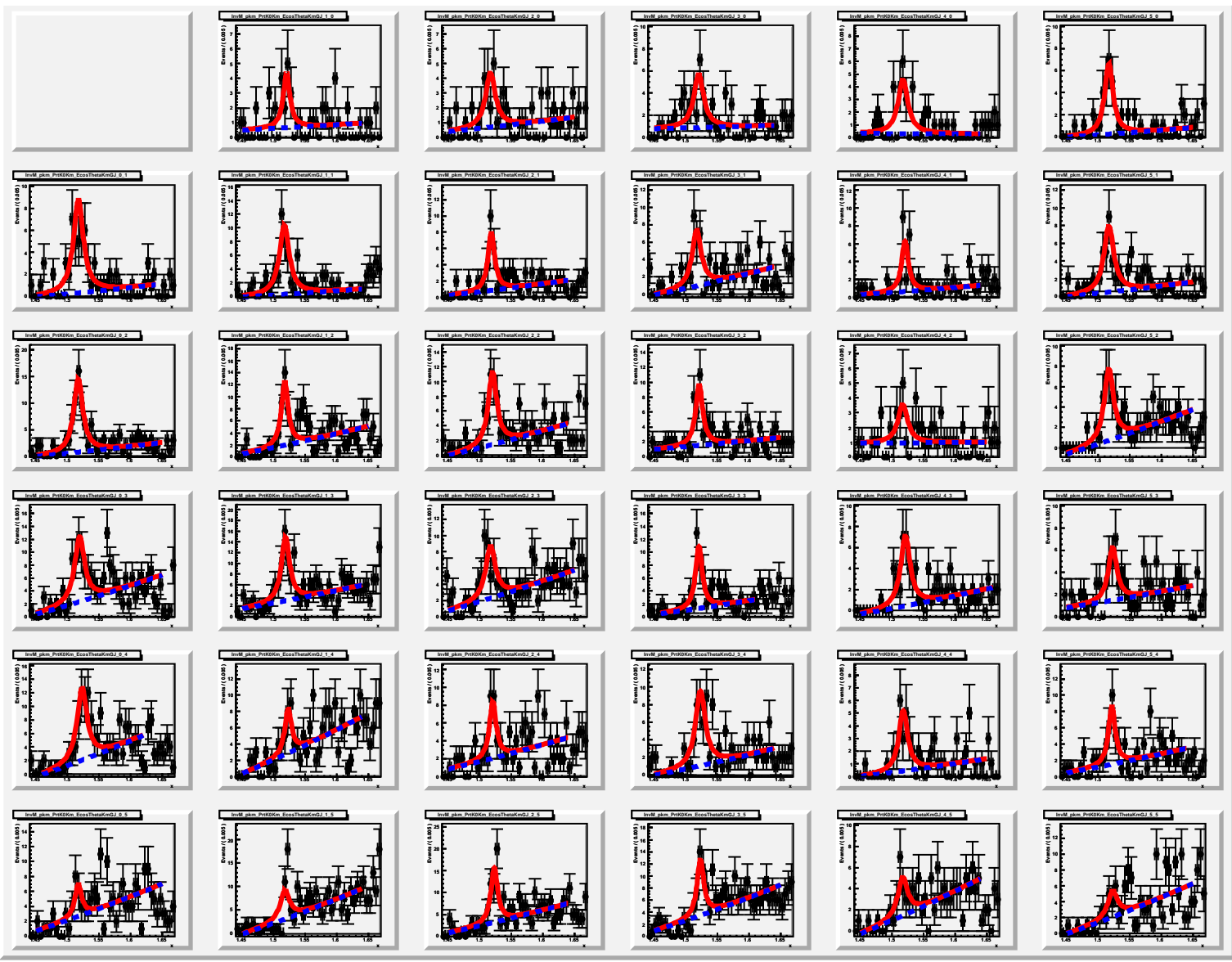
FIGURE 6.23. (Neutron Channel), $M(pK^-)$ at different E_γ and $cos\theta_{K^-}^{GJ}$ bins with fitting functions. E_γ rises from left to right pads and $\theta_{K^-}^{GJ}$ increases from top to bottom pads.
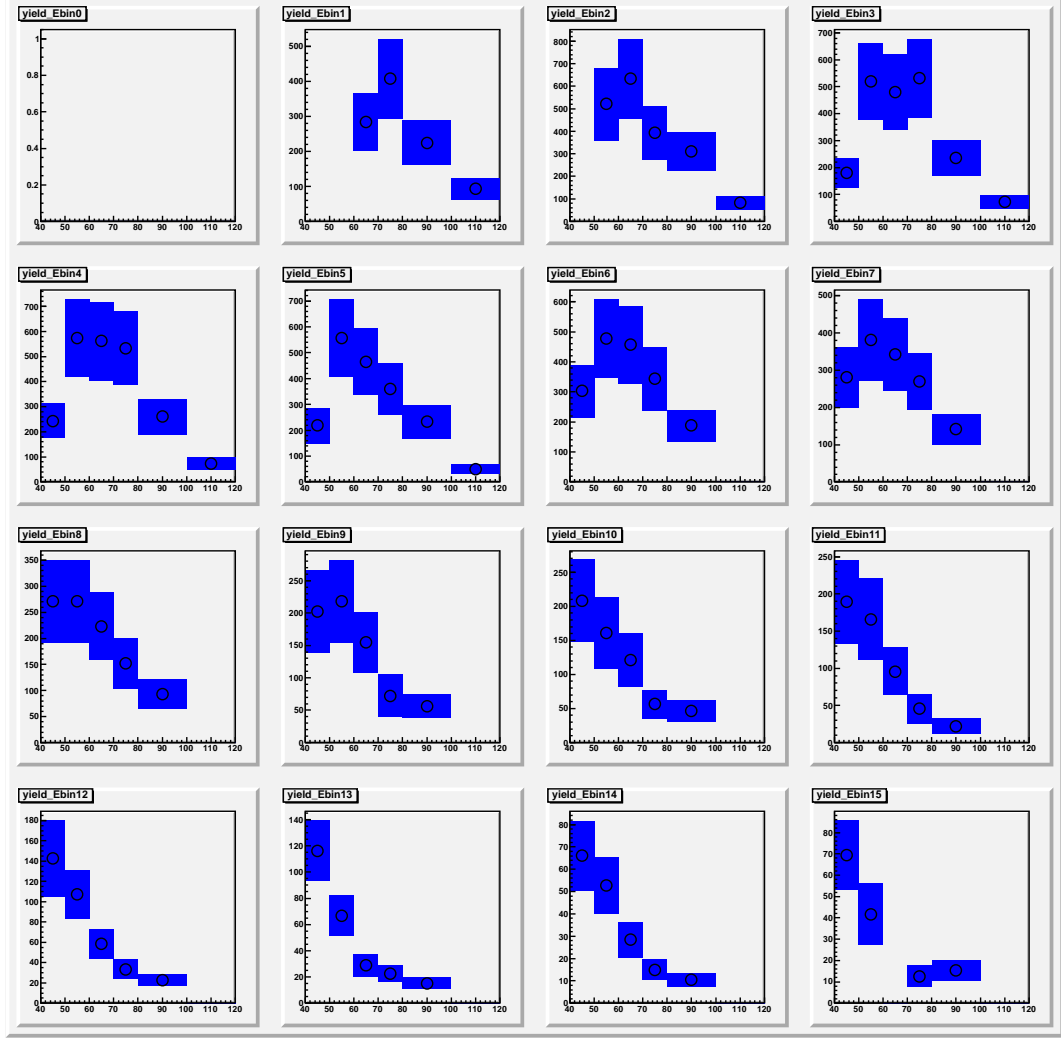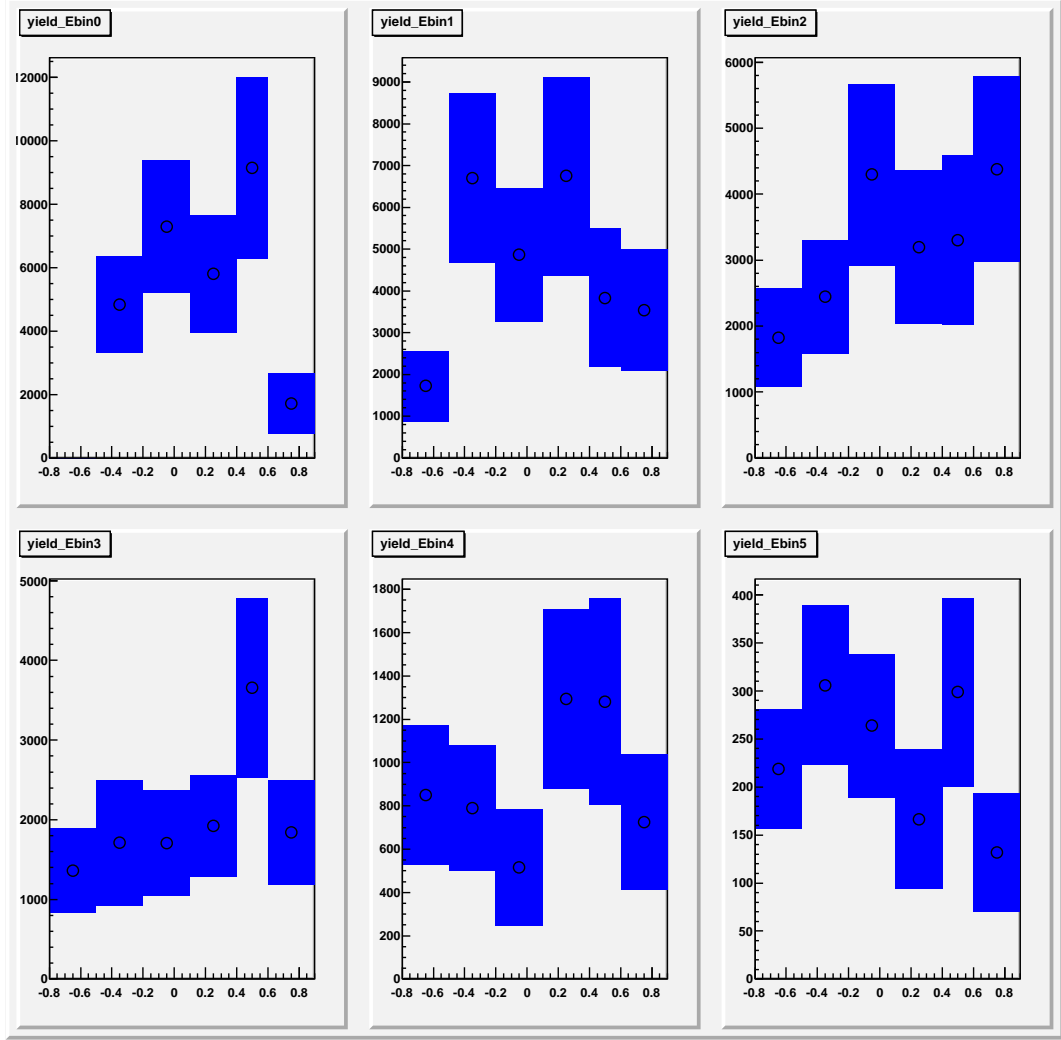
FIGURE 6.24. (**Neutron Channel**), $\Lambda^*(1520)$ yield distribution over $cos\theta_{K^-}^{GJ}$ at different E_γ bins. E_γ rises from left to right pads.
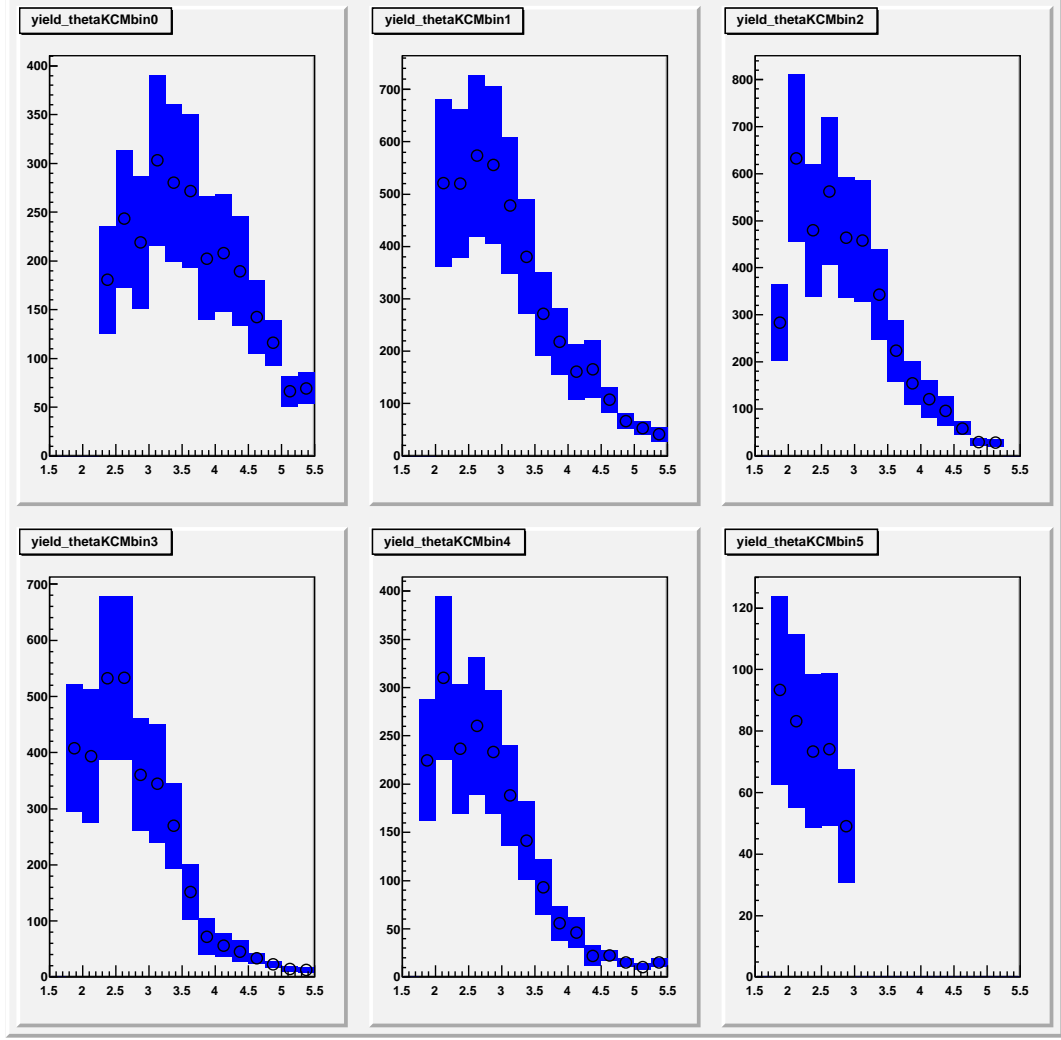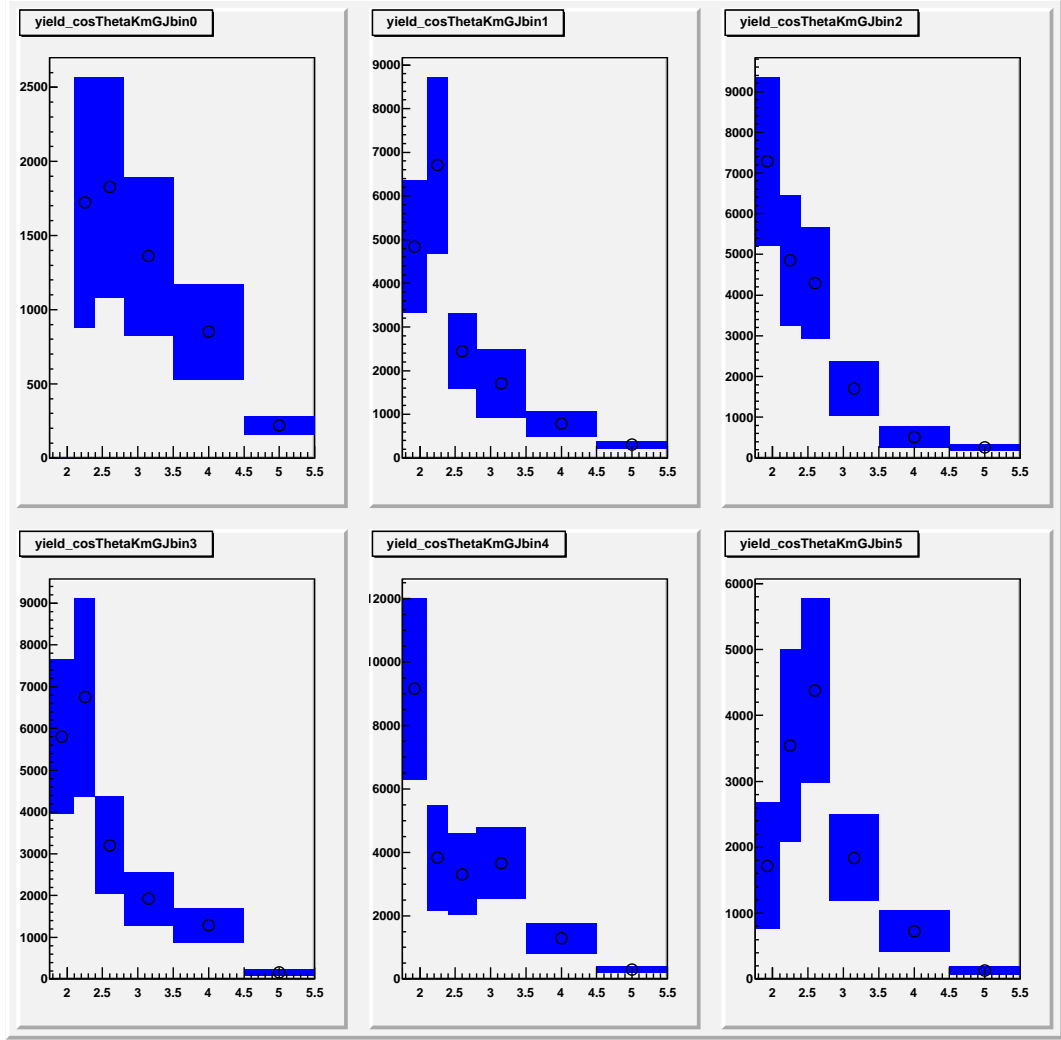
FIGURE 6.25. (**Neutron Channel**), $\Lambda^*(1520)$ yield distribution over E_γ at different $cos\theta_{K^-}^{GJ}$ bins. $\theta_{K^-}^{GJ}$ increases from top to bottom pads.

TABLE 6.4. Acceptance plots

kinematic binning (proton)	acceptance vs. A at E_γ	acceptance vs. E_γ at A
E_γ and t^*	Figure 6.26	Figure 6.27
E_γ and $\theta_{K^+}^{CM}$	Figure 6.30	Figure 6.31
E_γ and $cos\theta_{K^-}^{GJ}$	Figure 6.34	Figure 6.35
kinematic binning (neutron)	acceptance vs. A at E_γ	acceptance vs. E_γ at A
E_γ and t^*	Figure 6.28	Figure 6.29
E_γ and $\theta_{K^0}^{CM}$	Figure 6.32	Figure 6.33
E_γ and $cos\theta_{K^-}^{GJ}$	Figure 6.36	Figure 6.37

6.6. ACCEPTANCE

The acceptance is calculated in every kinematic bin as the ratio of $\Lambda^*(1520)$ yield of the simulated data over the number of events generated in that bin by the event generator. The results are shown in Figure. 6.25 - 6.36 as indicated in Table 6.4 for various combinations of kinematic variables. Generally the acceptance in a single bin is lower than 3%. The smooth distributions of acceptance over all kinematic variables indicate that the simulation behaves as expected.
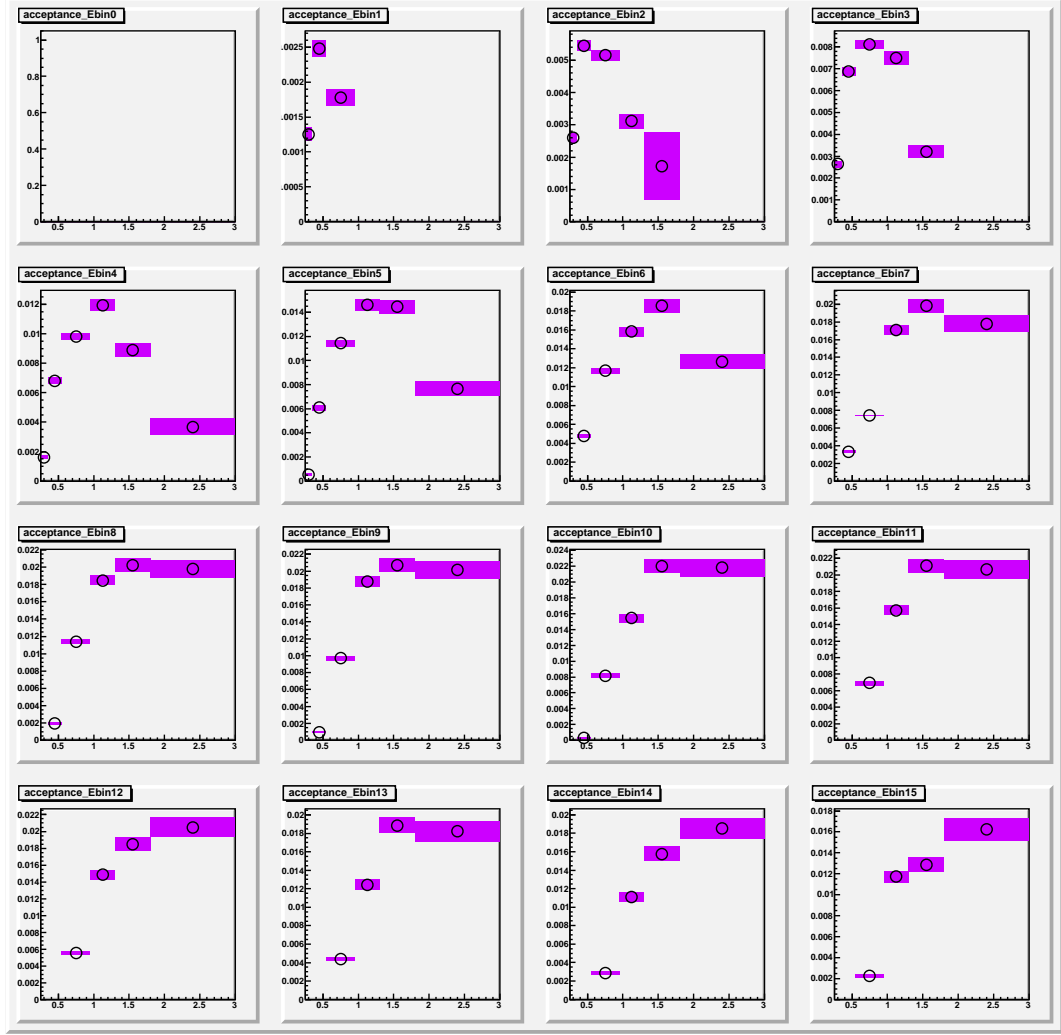
FIGURE 6.26. (**Proton Channel**), $\Lambda^*(1520)$ acceptance distribution over t^* at different E_γ bins. E_γ rises from left to right and top to bottom pads.
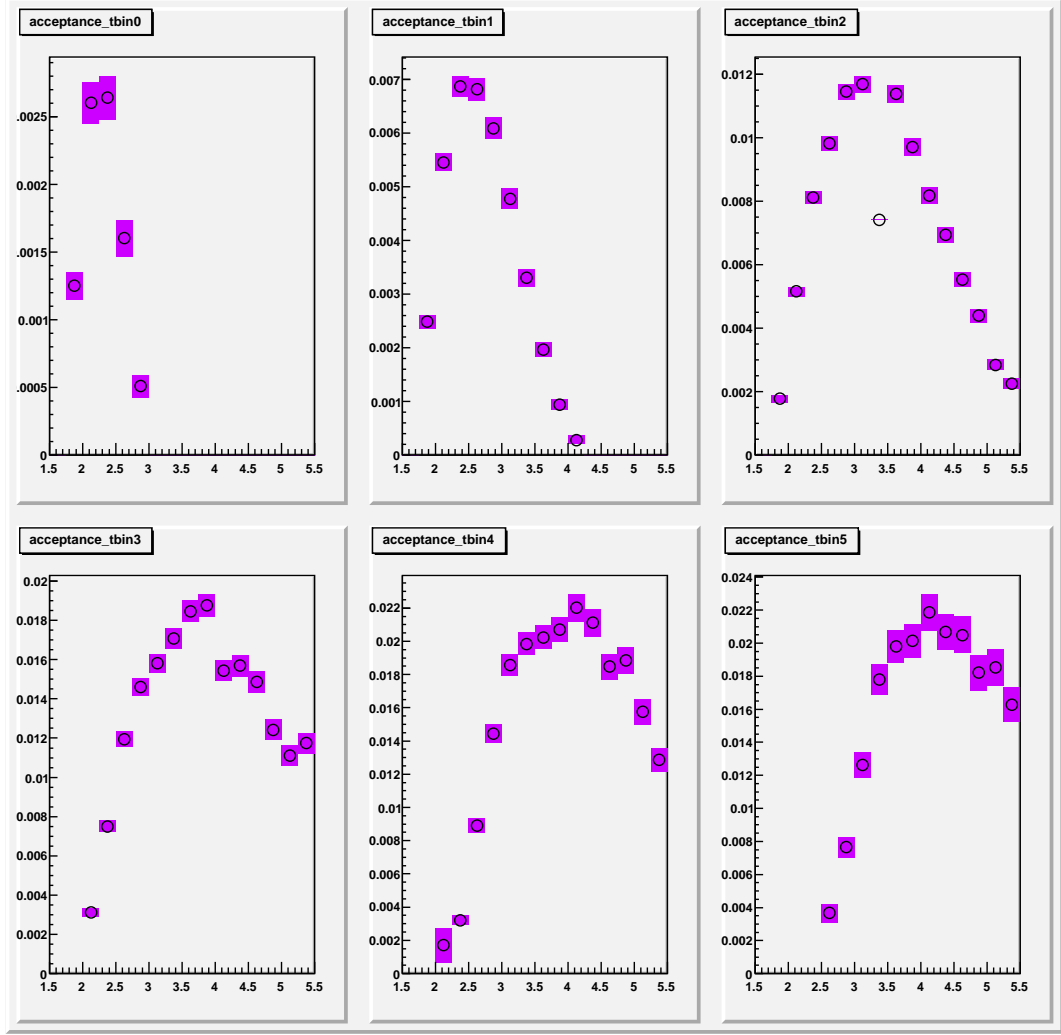
FIGURE 6.27. (**Proton Channel**), $\Lambda^*(1520)$ acceptance distribution over E_γ at different t^* bins. t^* rises from left to right and top to bottom pads.
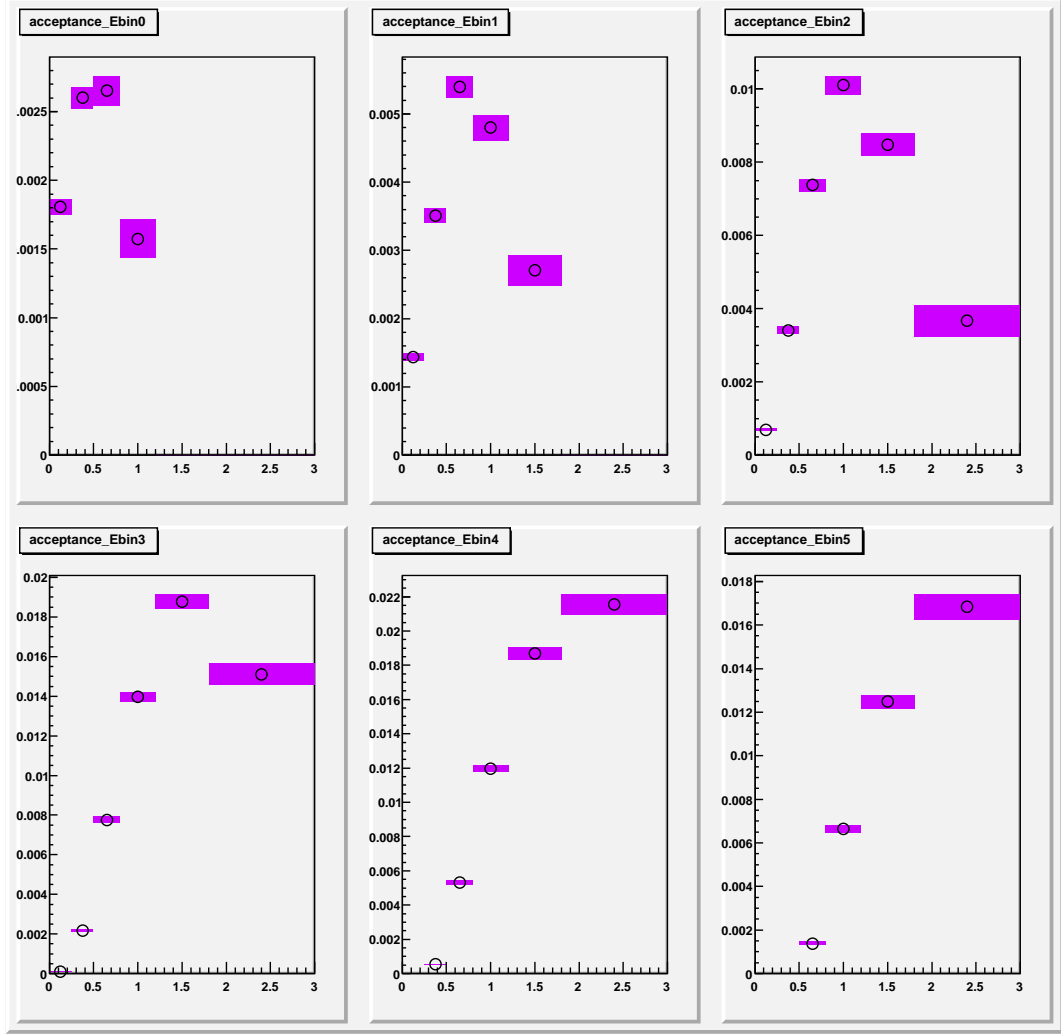
FIGURE 6.28. (**Neutron Channel**), $\Lambda^*(1520)$ acceptance distribution over t^* at different E_γ bins. E_γ rises from left to right and top to bottom pads.
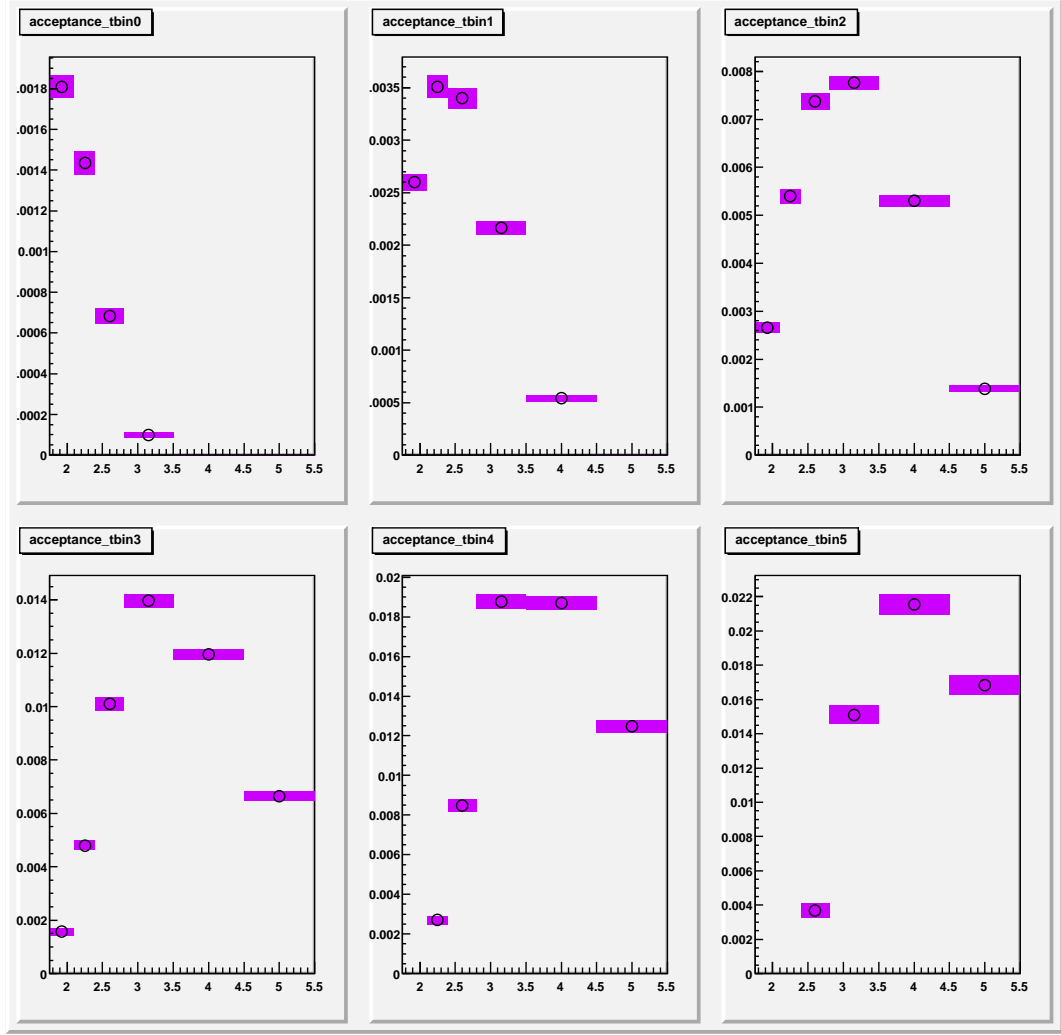
FIGURE 6.29. (**Neutron Channel**), $\Lambda^*(1520)$ acceptance distribution over E_γ at different t^* bins. t^* rises from left to right and top to bottom pads.
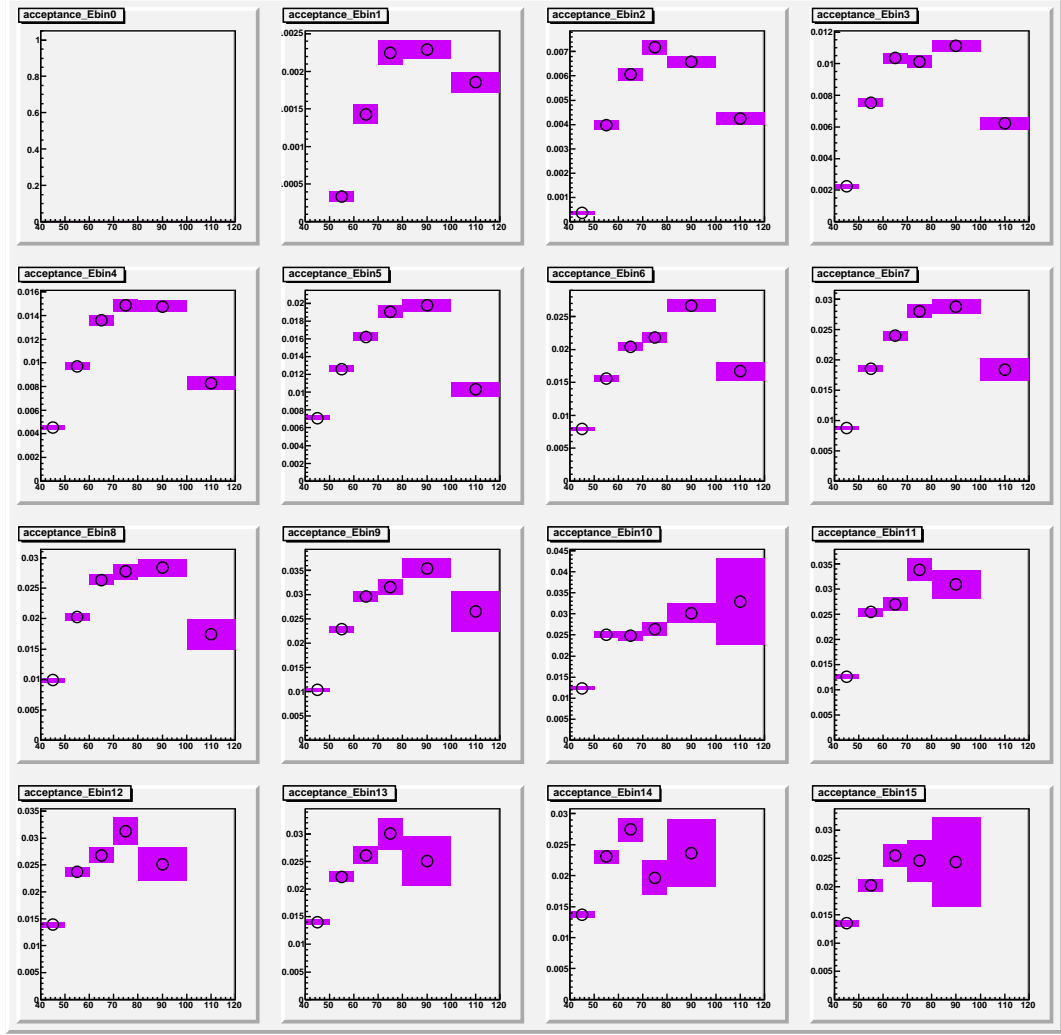
FIGURE 6.30. (**Proton Channel**), $\Lambda^*(1520)$ acceptance distribution over $\theta_{K^+}^{CM}$ at different E_γ bins. E_γ rises from left to right and top to bottom pads.
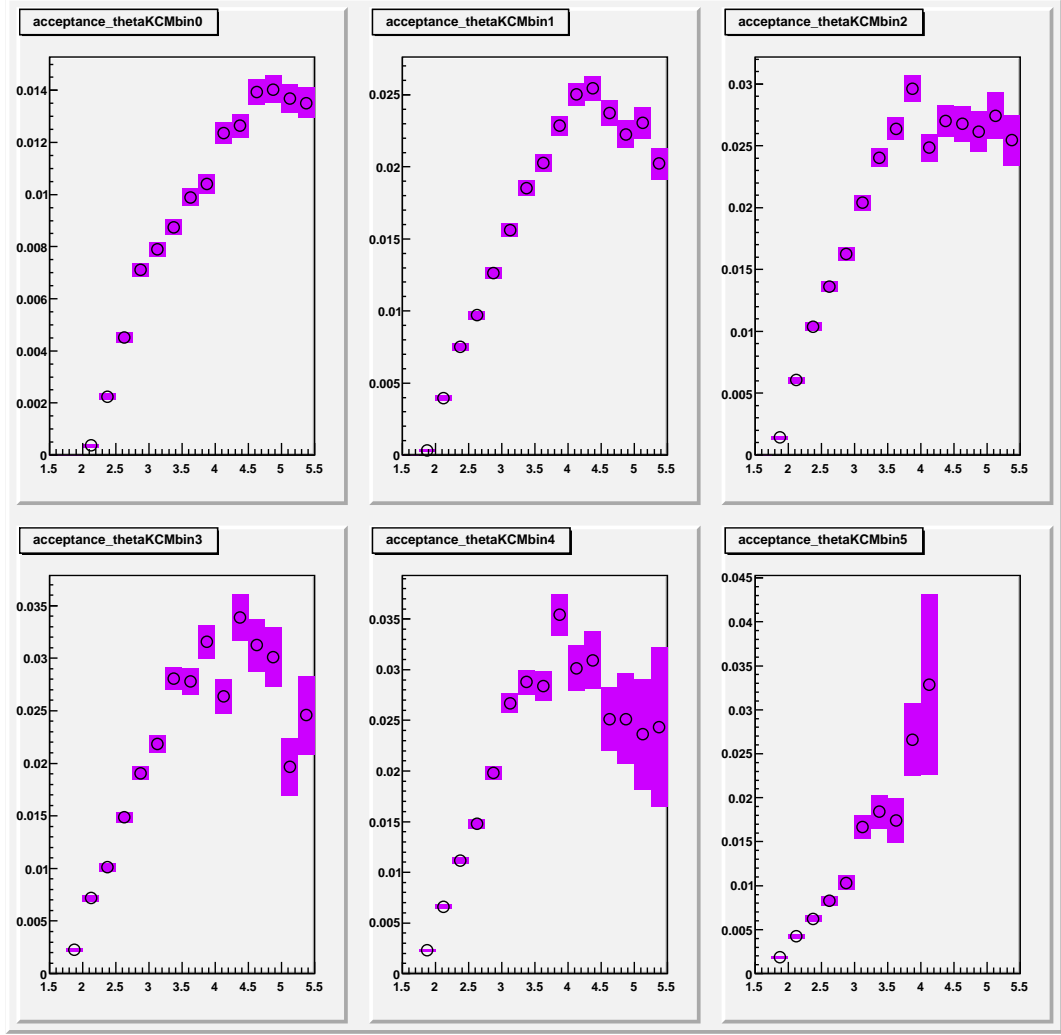
FIGURE 6.31. (**Proton Channel**), $\Lambda^*(1520)$ acceptance distribution over E_γ at different $\theta_{K^+}^{CM}$ bins. $\theta_{K^+}^{CM}$ rises from left to right and top to bottom pads.
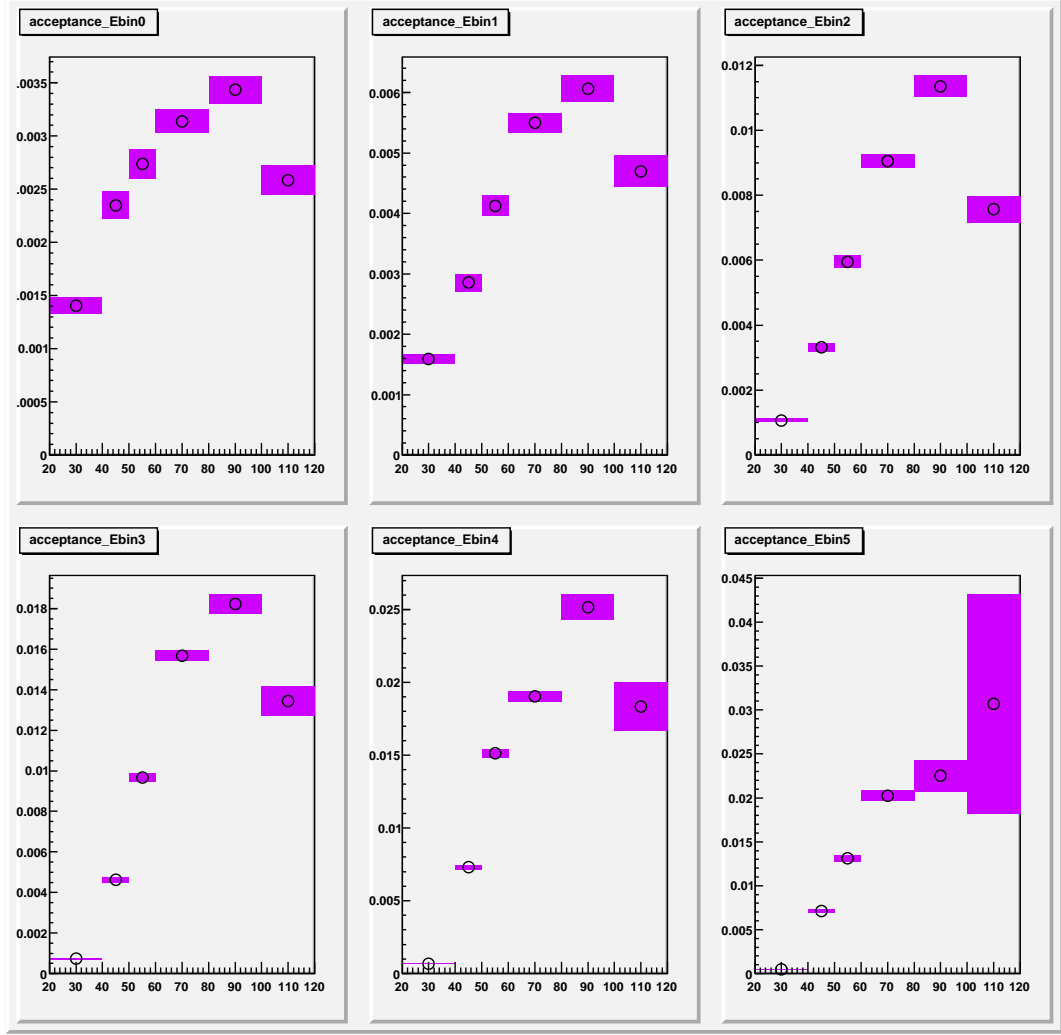
FIGURE 6.32. (**Neutron Channel**), $\Lambda^*(1520)$ acceptance distribution over $\theta_{K^0}^{CM}$ at different E_γ bins. E_γ rises from left to right and top to bottom pads.
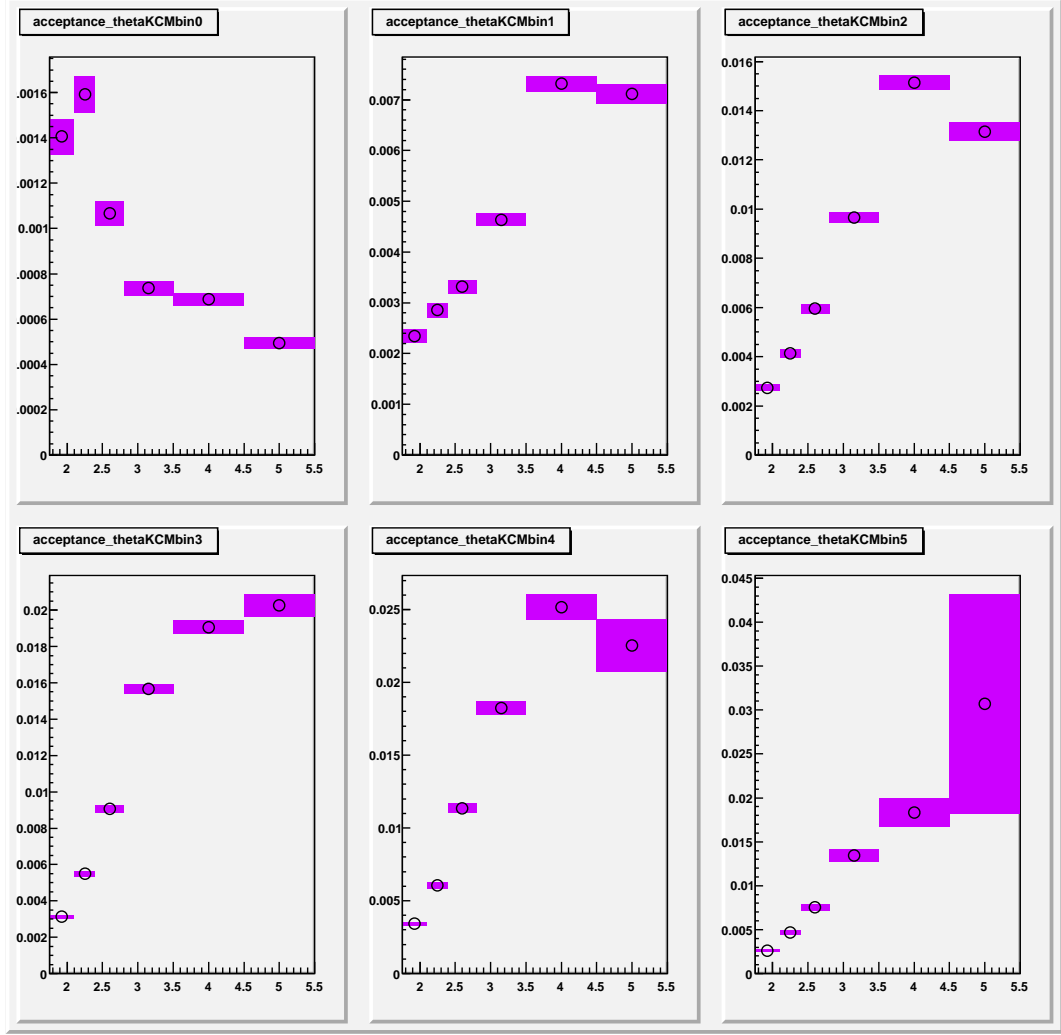
FIGURE 6.33. (**Neutron Channel**), $\Lambda^*(1520)$ acceptance distribution over E_γ at different $\theta_{K^0}^{CM}$ bins. $\theta_{K^0}^{CM}$ rises from left to right and top to bottom pads.
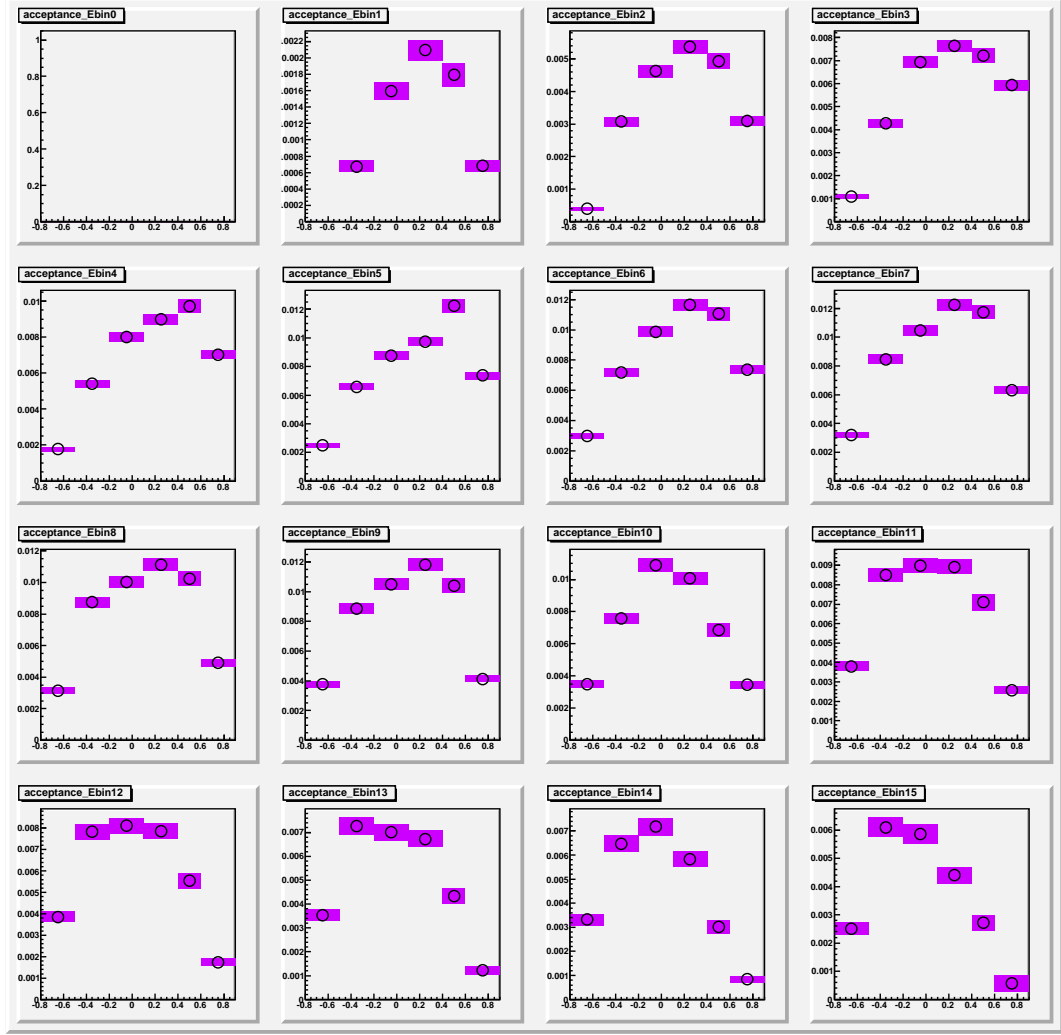
FIGURE 6.34. (**Proton Channel**), $\Lambda^*(1520)$ acceptance distribution over $cos\theta_{K^-}^{GJ}$ at different E_γ bins. E_γ rises from left to right and top to bottom pads.
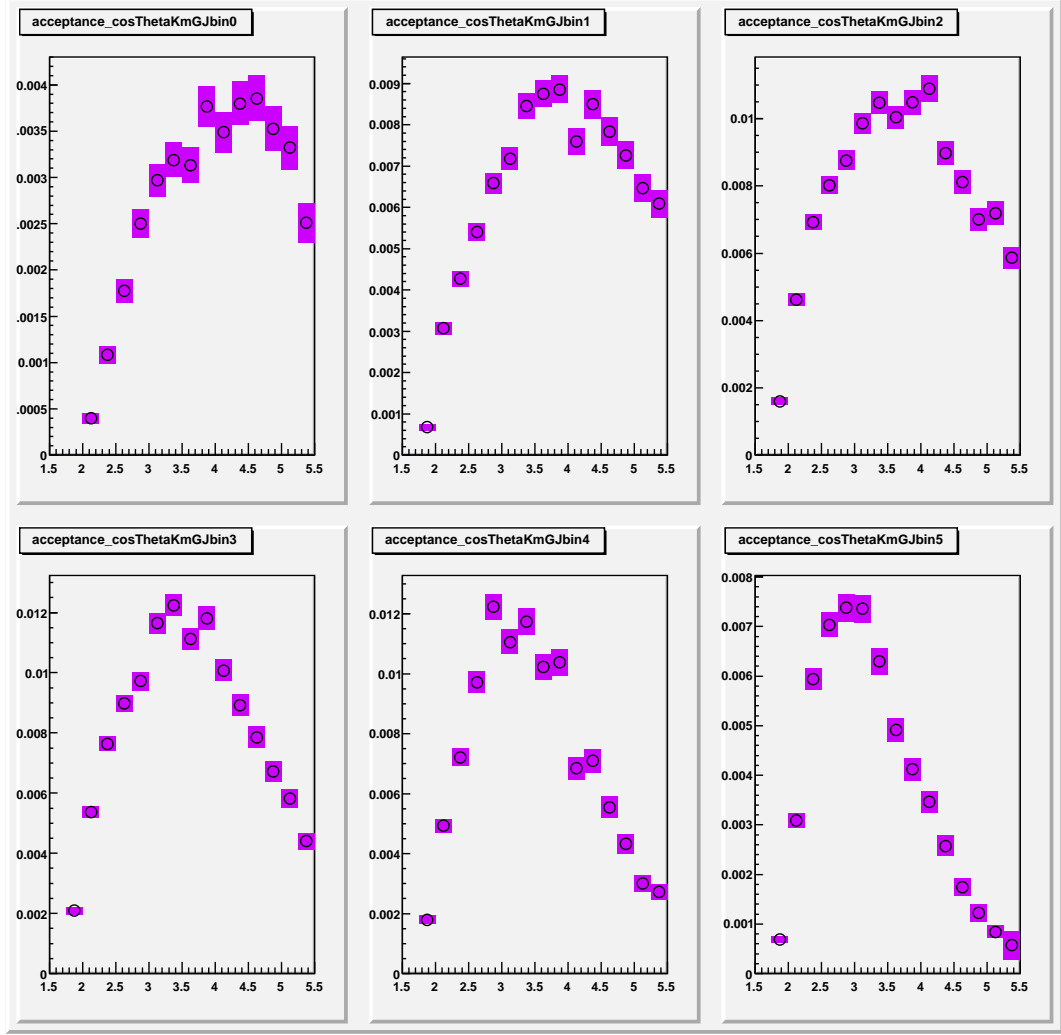
FIGURE 6.35. (**Proton Channel**), $\Lambda^*(1520)$ acceptance distribution over E_γ at different $cos\theta_{K^-}^{GJ}$ bins. $cos\theta_{K^-}^{GJ}$ rises from left to right and top to bottom pads.
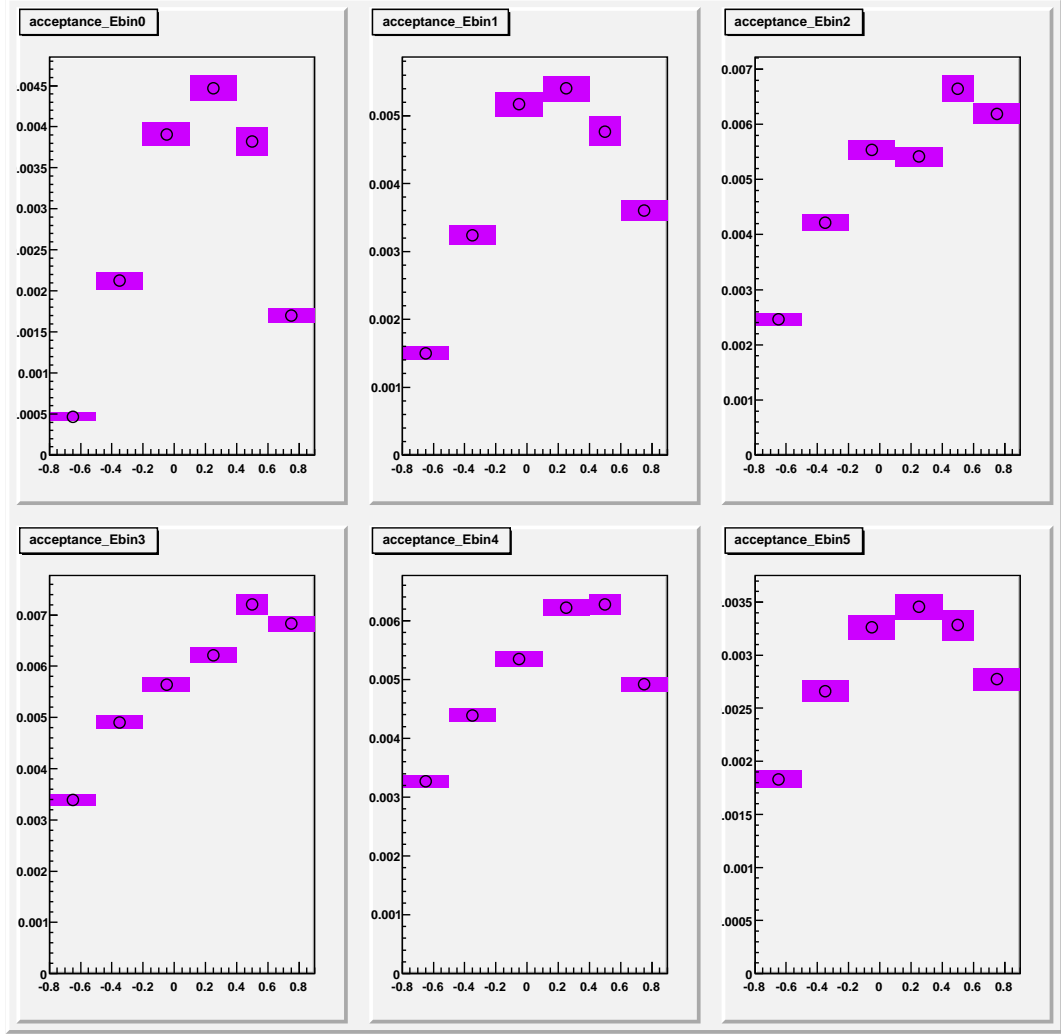
FIGURE 6.36. (**Neutron Channel**), $\Lambda^*(1520)$ acceptance distribution over $cos\theta_{K^-}^{GJ}$ at different E_γ bins. E_γ rises from left to right and top to bottom pads.

109
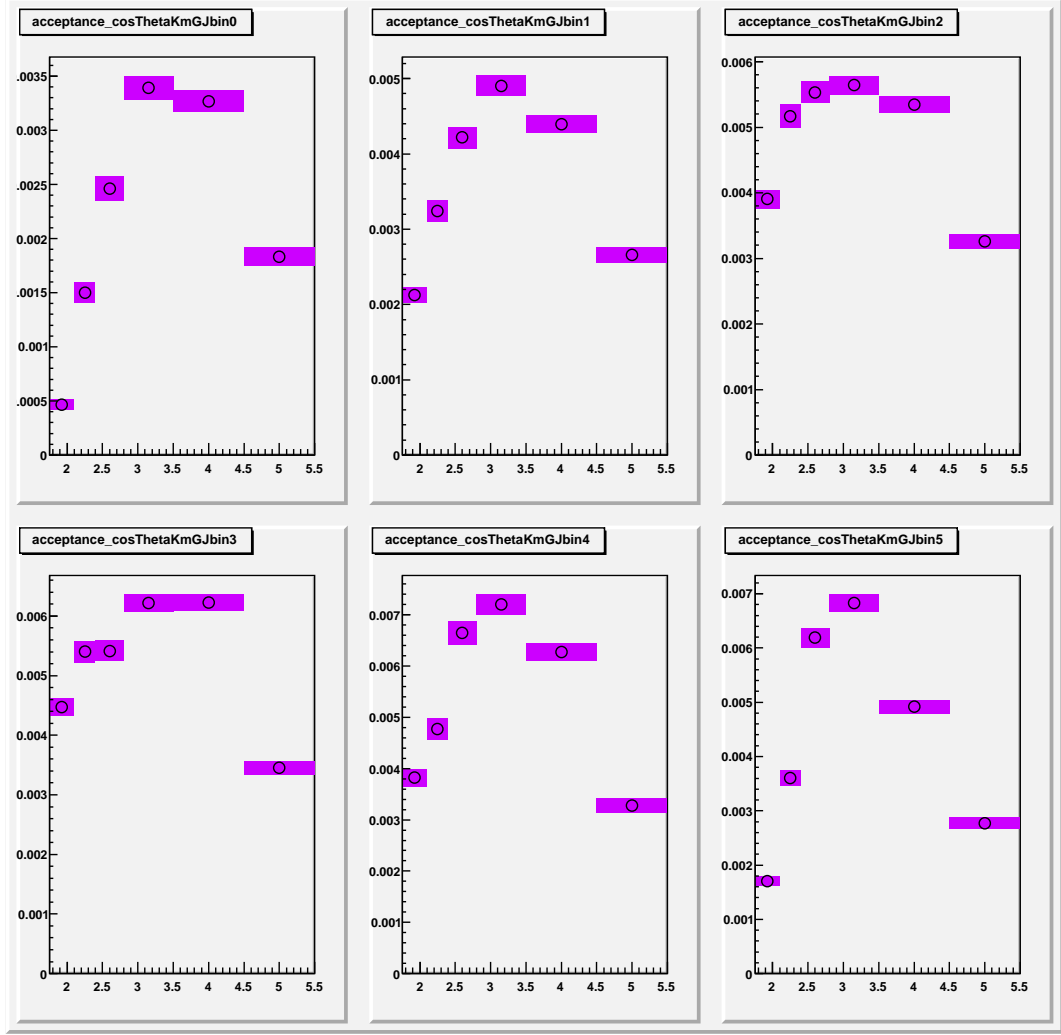
FIGURE 6.37. (**Neutron Channel**), $\Lambda^*(1520)$ acceptance distribution over E_γ at different $cos\theta_{K^-}^{GJ}$ bins. $cos\theta_{K^-}^{GJ}$ rises from left to right and top to bottom pads.

FIGURE 6.38. (**Proton Channel**), $\Lambda^*(1520)$ differential cross section $d\sigma/dt^*$ distributions over t^* at different E_γ bins. E_γ rises from left to right and top to bottom pads.

6.7. DIFFERENTIAL CROSS SECTION

6.7.1. E_γ versus t^*. The $\Lambda^*(1520)$ differential cross section $d\sigma/dt^*$ distributions over t^* are shown at various E_γ bins for the proton channel in Figure 6.38 and the neutron channel in Figure 6.39. The data points can be well parameterized by an exponential function $\alpha e^{-\beta t^*}$ for both the proton and neutron channels in the range $t^* = 0$ - 3 GeV^2 of the eg3 experiment. This indicates t-channel dominance of the $\Lambda^*(1520)$ production for both reactions.
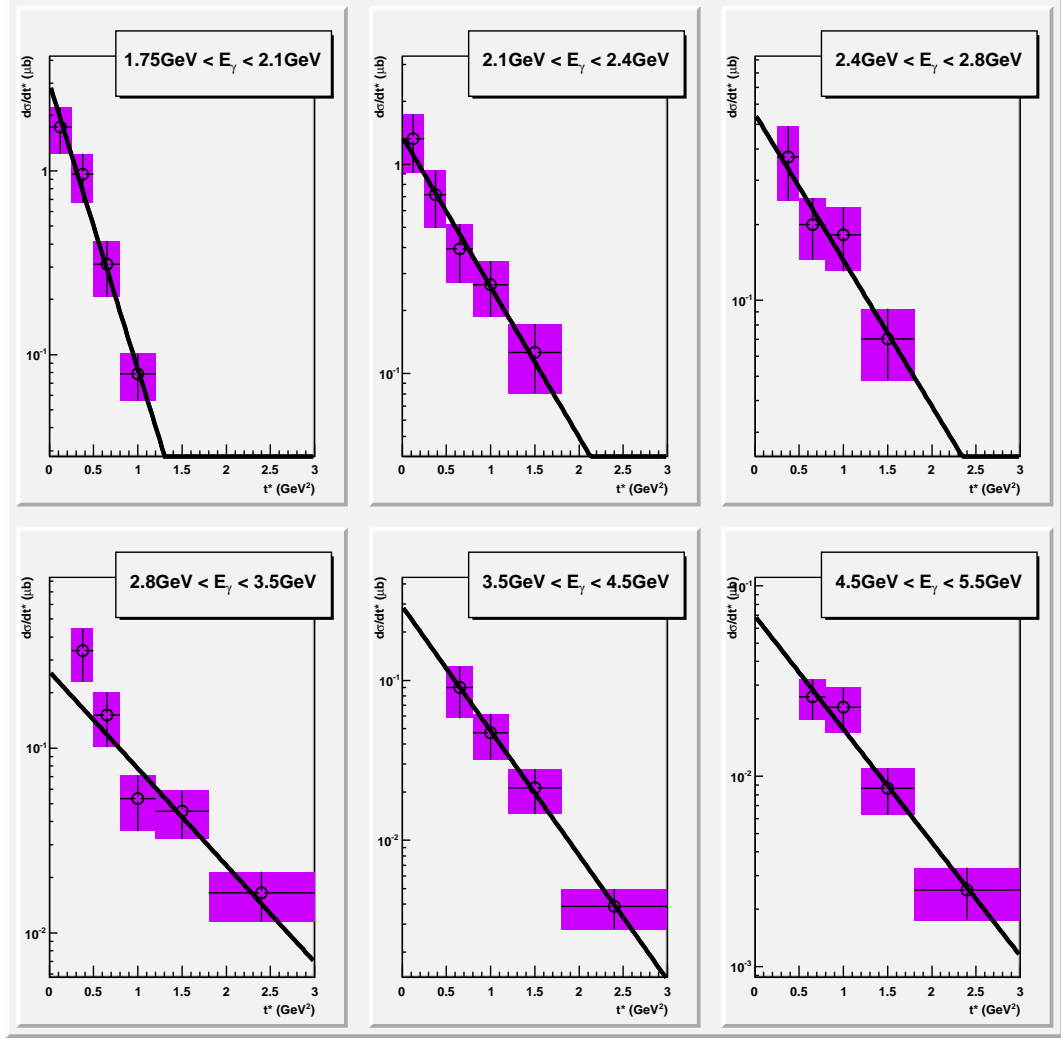
FIGURE 6.39. (**Neutron Channel**), $\Lambda^*(1520)$ differential cross section $d\sigma/dt^*$ distributions over t^* at different E_γ bins. E_γ rises from left to right and top to bottom pads.

The CLAS g11 experiment has studied $\Lambda^*(1520)$ photoproduction on a hydrogen target [36]. Their preliminary $\Lambda^*(1520)$ differential cross section $d\sigma/dt^*$ distributions over t^* are shown at 34 bins of $E_\gamma = 1.85$ - 3.75 GeV as shown in Figure 6.40. They can be well parametrized by an exponential function also like the eg3 experiment.

The fitted t-slopes from CLAS eg3 and g11 experiments are shown in Figure 6.41. The results of the neutron channel in eg3 are flat over all energies at about $\beta = 2c^4/GeV^2$. The results of the proton channel in eg3 have very similar behavior to those of g11. It is also mostly flat above $E_\gamma = 2.5 GeV$ at about $\beta = 2c^4/GeV^2$, but
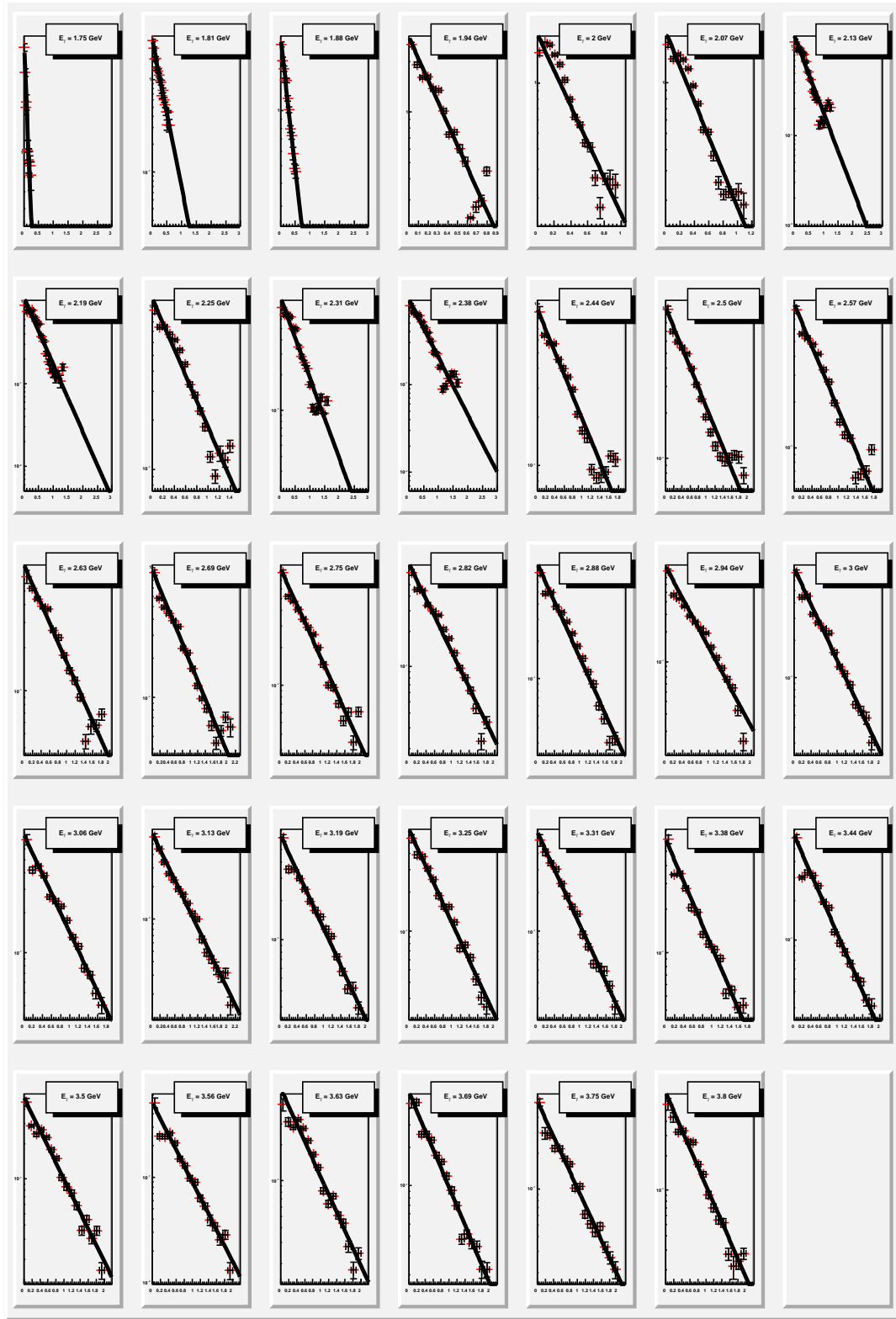
FIGURE 6.40. The preliminary results from the CLAS g11 experiment, $\Lambda^*(1520)$ differential cross section $d\sigma/dt^*$ distributions over t^* at different E_γ bins. E_γ rises from left to right and top to bottom pads.
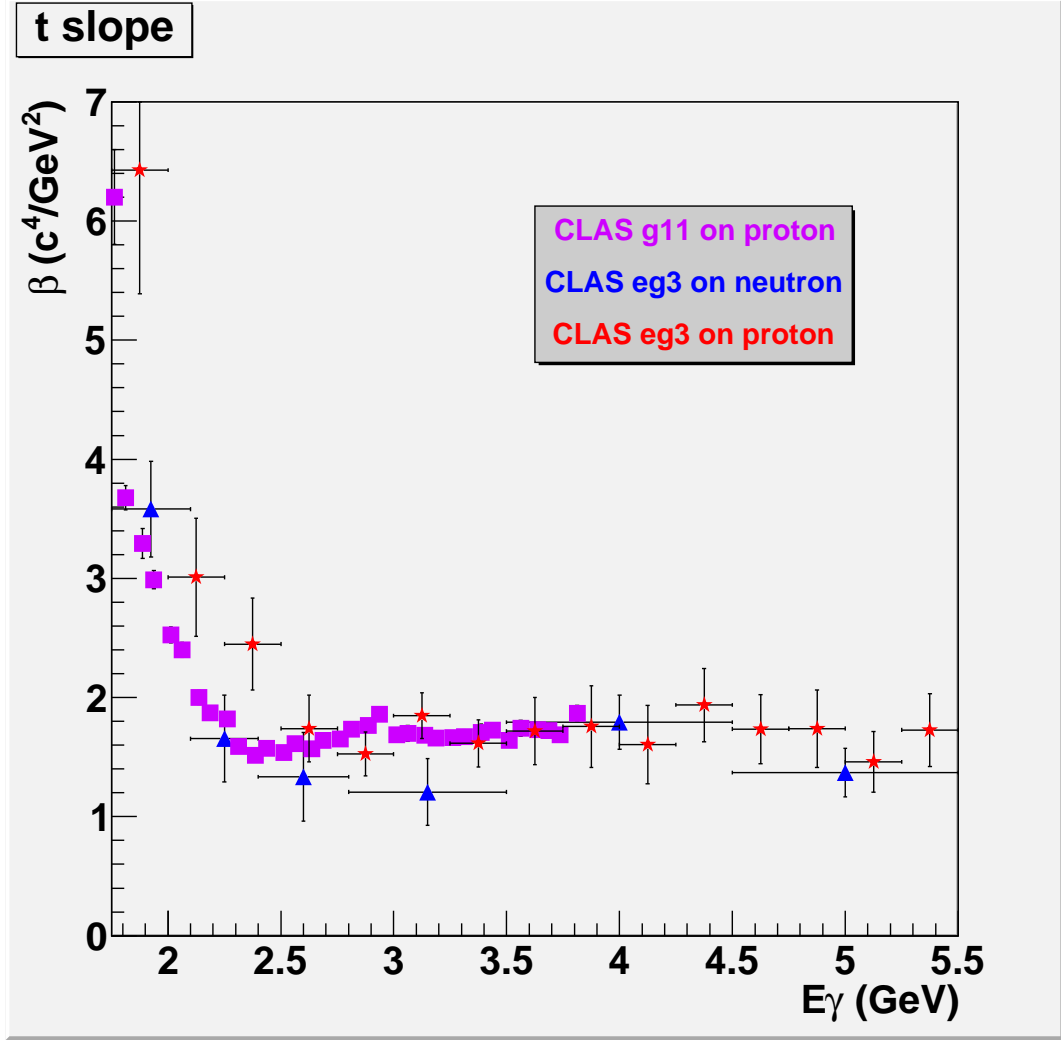
FIGURE 6.41. t-slopes from fitting of $d\sigma/dt^*$ over t^*

rises distinctively for lower E_γ. This may be caused by the $\phi(1020)$ overlapping with $\Lambda^*(1520)$ at lower energies (see Section 5.8), but it is not investigated in this study.
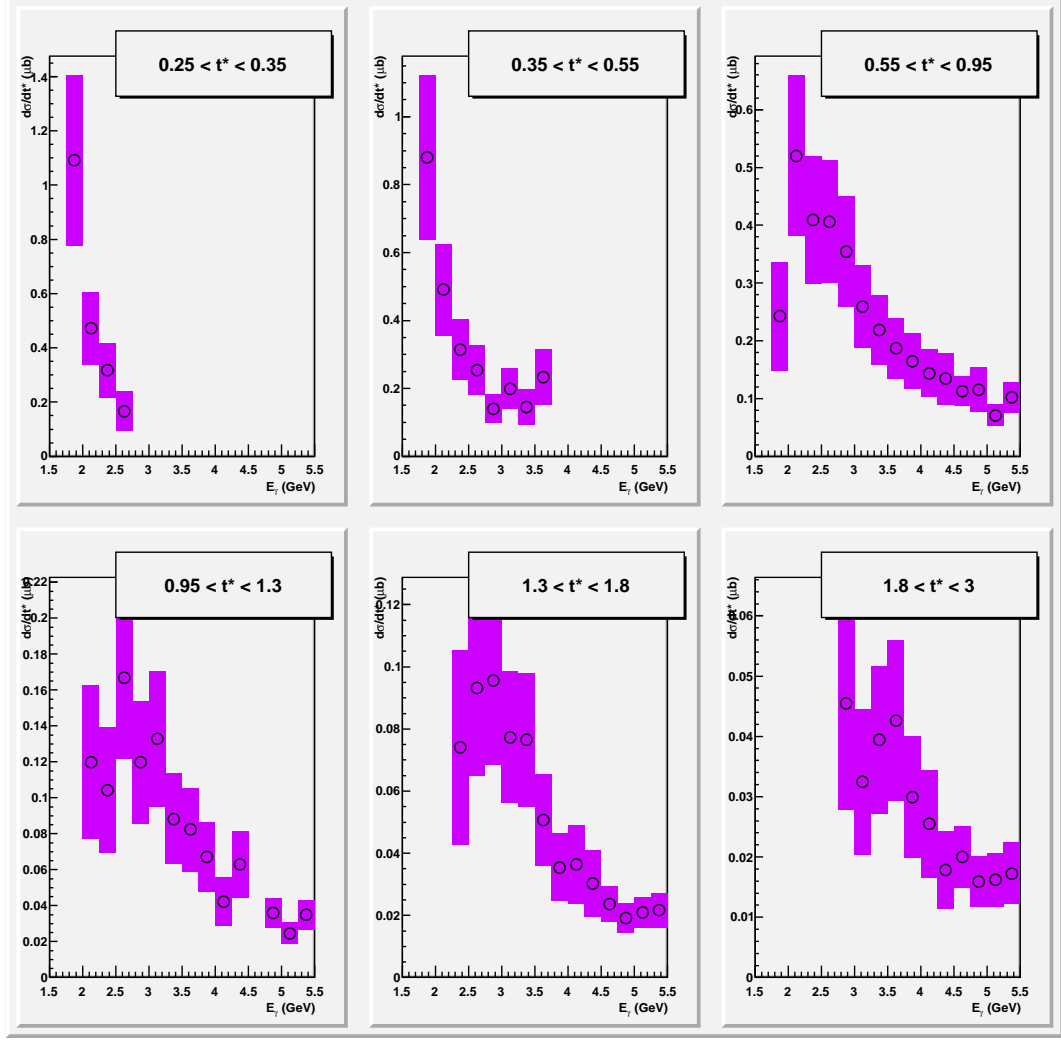
FIGURE 6.42. (**Proton Channel**), $\Lambda^*(1520)$ differential cross section $d\sigma/dt^*$ distributions over E_γ at different t^* bins. t^* rises from left to right and top to bottom pads.

The $\Lambda^*(1520)$ differential cross section $d\sigma/dt^*$ distributions over E_γ are shown at various t^* bins for the proton channel in Figure 6.42 and the neutron channel in Figure 6.43. The cross section shows a gradual decrease with increasing photon energies like other hyperon photoproduction, such as $K^+\Lambda(1116)$ and $K^+\Sigma^0(1193)$ [37]. Due to our limited statistics at low photon energy bins, the bump structure can only be seen at some t^* bins, but not all of them. There is no sign of resonance structures at any t^* bin.
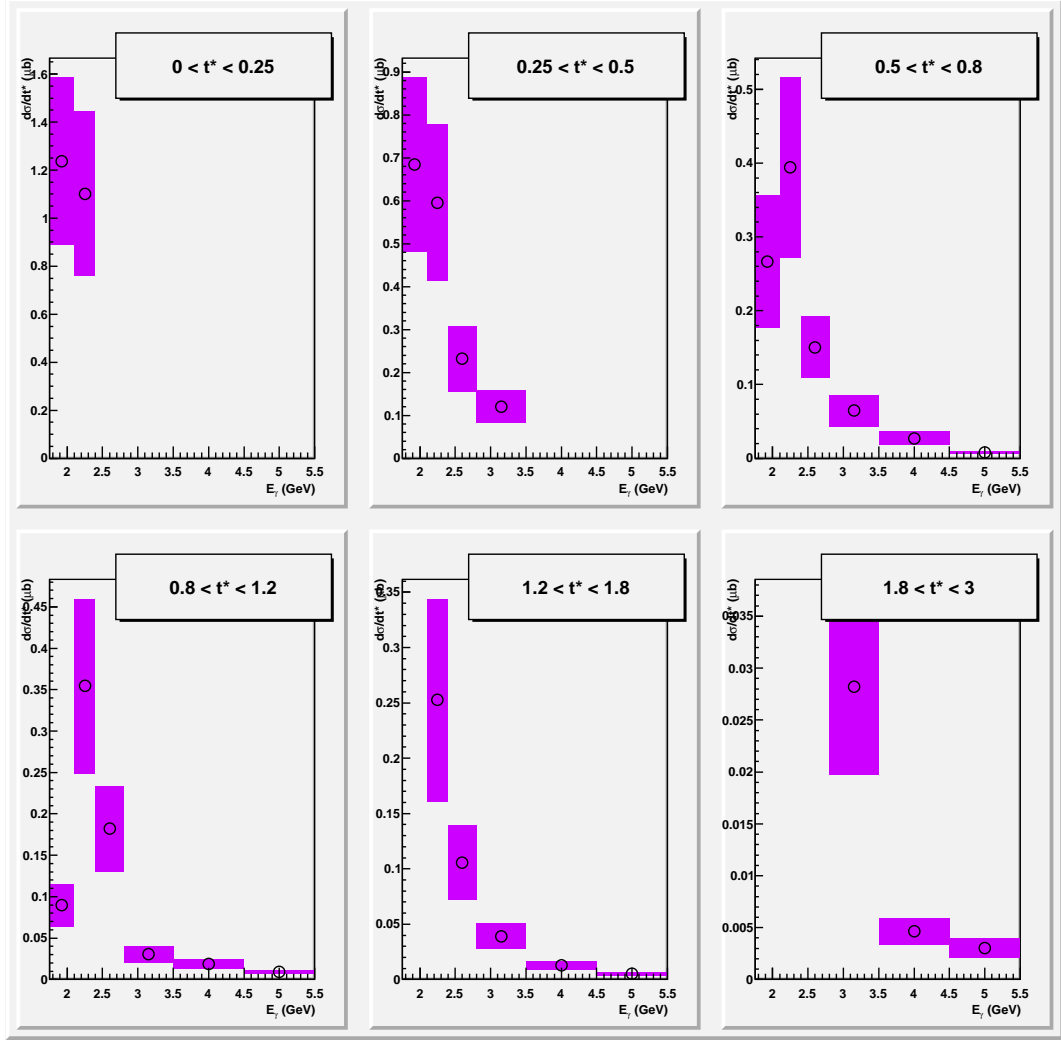
FIGURE 6.43. (**Neutron Channel**), $\Lambda^*(1520)$ differential cross section $d\sigma/dt^*$ distributions over E_γ at different t^* bins. t^* rises from left to right and top to bottom pads.

FIGURE 6.44. (**Proton Channel**), $\Lambda^*(1520)$ differential cross section $d\sigma/d\theta_{K^+/K^0}^{CM}$ distributions over θ_{K^+/K^0}^{CM} at different E_γ bins. E_γ rises from left to right and top to bottom pads.
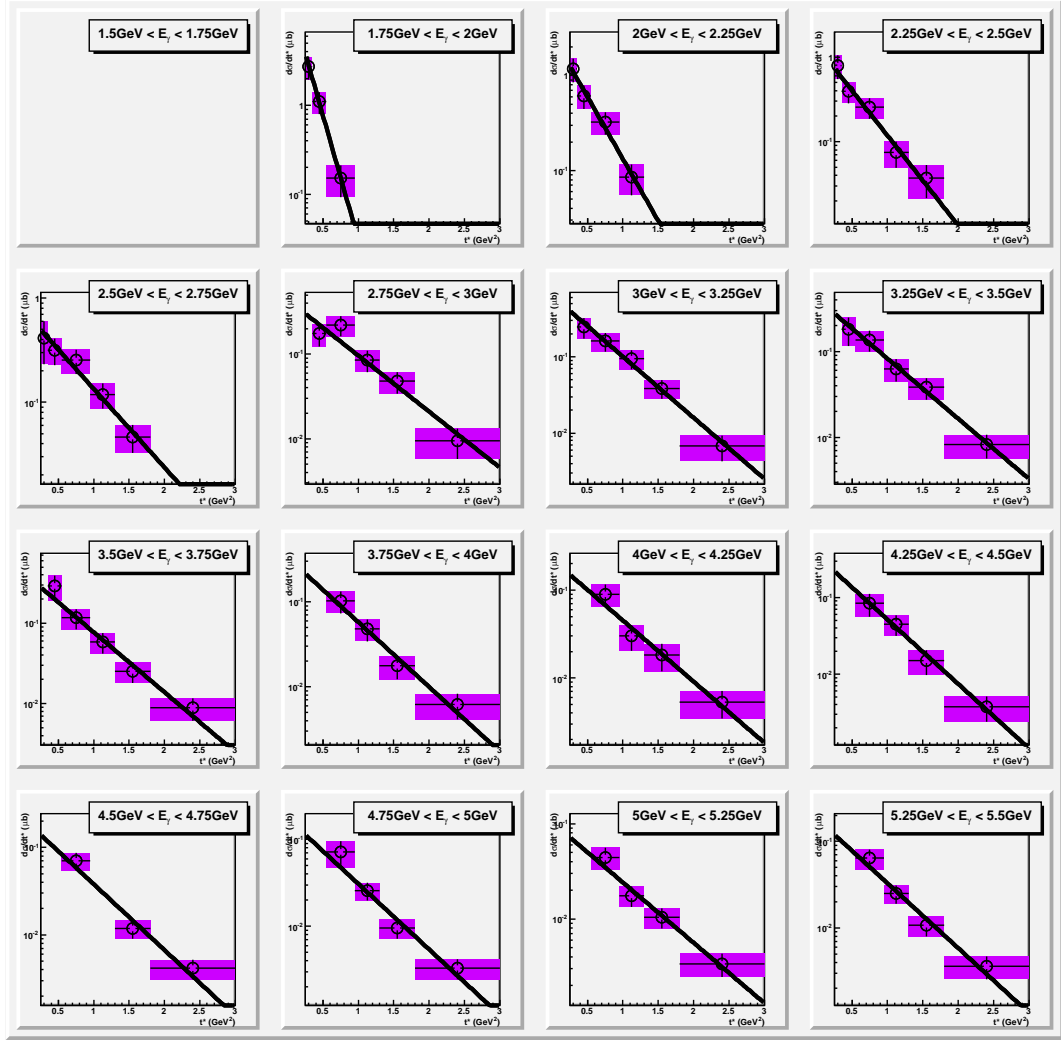
6.7.2. E_γ versus θ_{K^+/K^0}^{CM}. The $\Lambda^*(1520)$ differential cross section $d\sigma/d\theta_{K^+/K^0}^{CM}$ distributions over θ_{K^+/K^0}^{CM} are shown at various E_γ bins for the proton channel in Figure 6.44 and the neutron channel in Figure 6.45. In all E_γ bins, the differential cross sections in both channels have large contributions at forward angles and drop quickly when they go to backward angles. This again indicates the t-channel dominance of the $\Lambda^*(1520)$ production in both reactions.

117

FIGURE 6.45. (**Neutron Channel**), $\Lambda^*(1520)$ differential cross section $d\sigma/d\theta^{CM}_{K^+/K^0}$ distributions over $\theta^{CM}_{K^+/K^0}$ at different E_γ bins. E_γ rises from left to right and top to bottom pads.

LEPS has published the $\Lambda^*(1520)$ differential cross section on hydrogen at the forward K^+ angles from $0°$ to $55°$ in the center of mass frame [18] (see Section 1.3.1). They used several models to fit the data. Even though the position of the bump is just above the threshold where the cross section will generally rise and fall with increasing E_γ, the model that fits best to the data includes a resonance $N^*(2110)$ with the width 140 MeV and $J^p = 3/2^+$. Around the mass region, there are nucleon resonances like $D_{13}(2080)$ with 2-star status, $S_{11}(2090)$ and $P_{11}(2100)$ with 1-star status, and $G_{17}(2190)$ with 4-star status in the PDG particle listings [1]. These resonances have width much wider than 140 MeV, and there is no corresponding nucleon resonance at 2.11 GeV.

The eg3 $\Lambda^*(1520)$ differential cross section $d\sigma/d\theta_{K^+/K^0}^{CM}$ distributions over E_γ are shown at various θ_{K^+/K^0}^{CM} bins for the proton channel in Figure 6.46 and the neutron channel in Figure 6.47. Our angle coverage is from $40°$ to $120°$ for the proton channel and $20°$ to $120°$ for the neutron channel, so there are some overlaps with the angle coverage of LEPS, but our energy coverage E_γ from 1.75 to 5.50 GeV is much larger than the LEPS which only covers the near-threshold energies up to $E_\gamma = 2.4$ GeV. We are limited by statistics to have photon energy bins as small as those of LEPS at low energies. The bump structure can only be seen at some angle bins and the assumption of having a nucleon resonance to describe the data seems not plausible.

Before making any conclusion about if there is any resonance structure at the near-threshold, we need to have detailed investigation of the $\phi(1020)$ overlapping with $\Lambda^*(1520)$ at the same energy region.
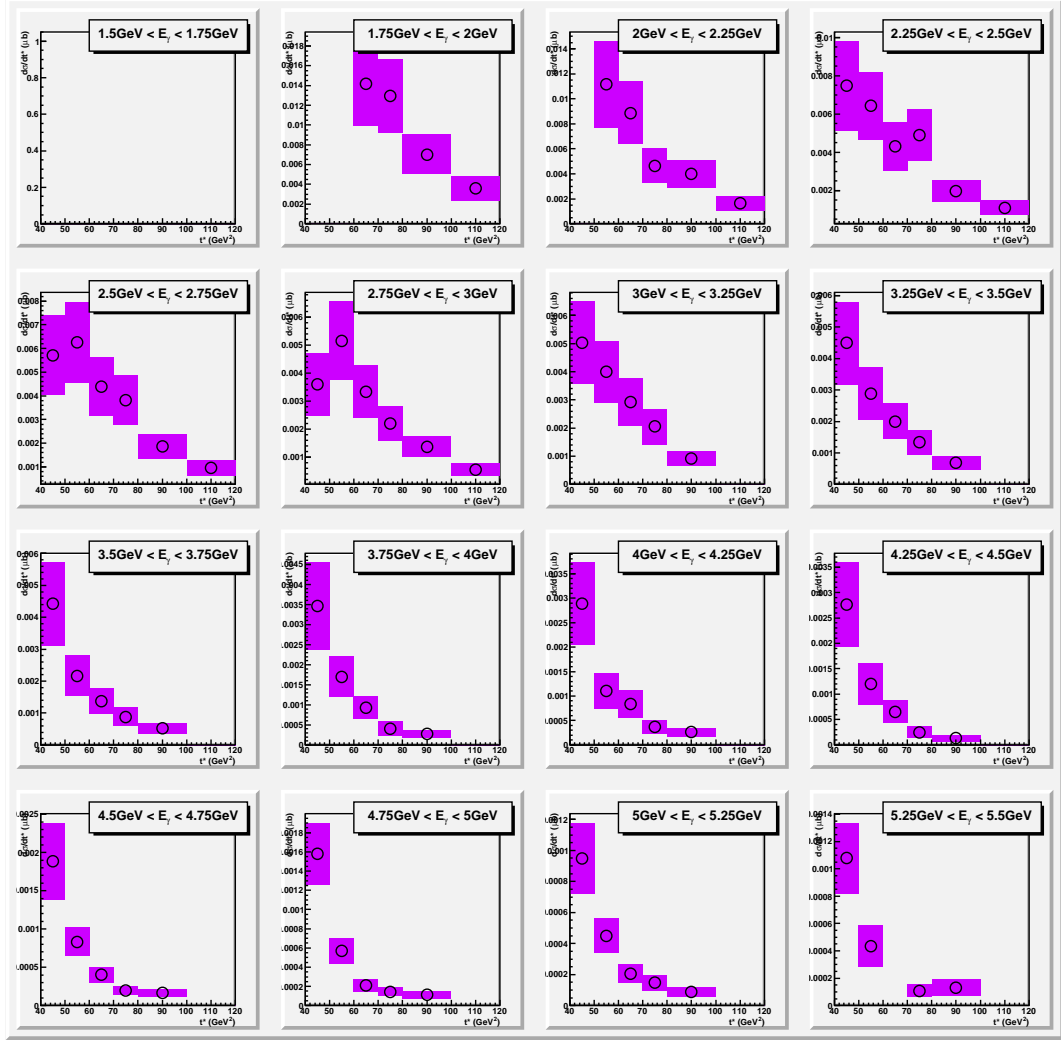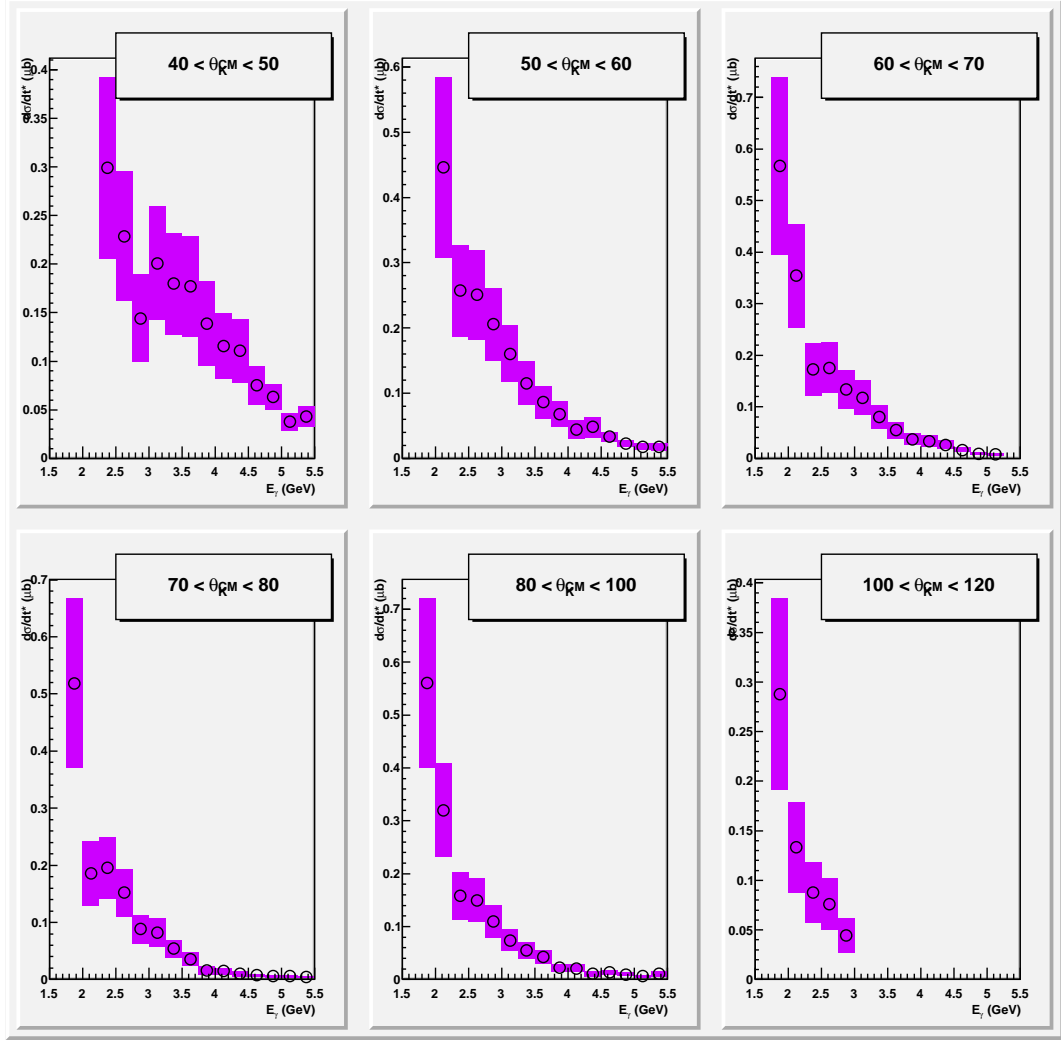
FIGURE 6.46. (**Proton Channel**), $\Lambda^*(1520)$ differential cross section $d\sigma/d\theta_{K^+}^{CM}$ distributions over E_γ at different $\theta_{K^+}^{CM}$ bins. $\theta_{K^+}^{CM}$ rises from left to right and top to bottom pads.

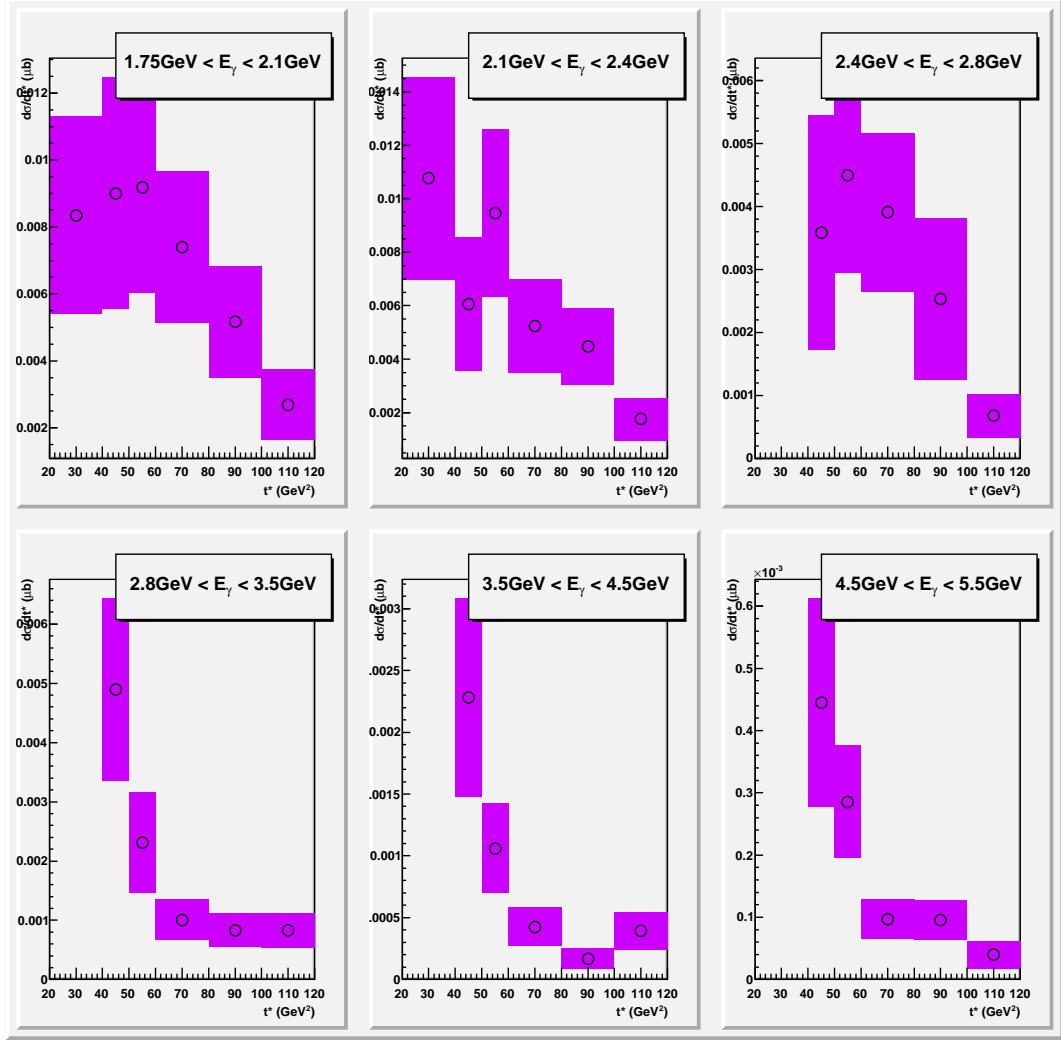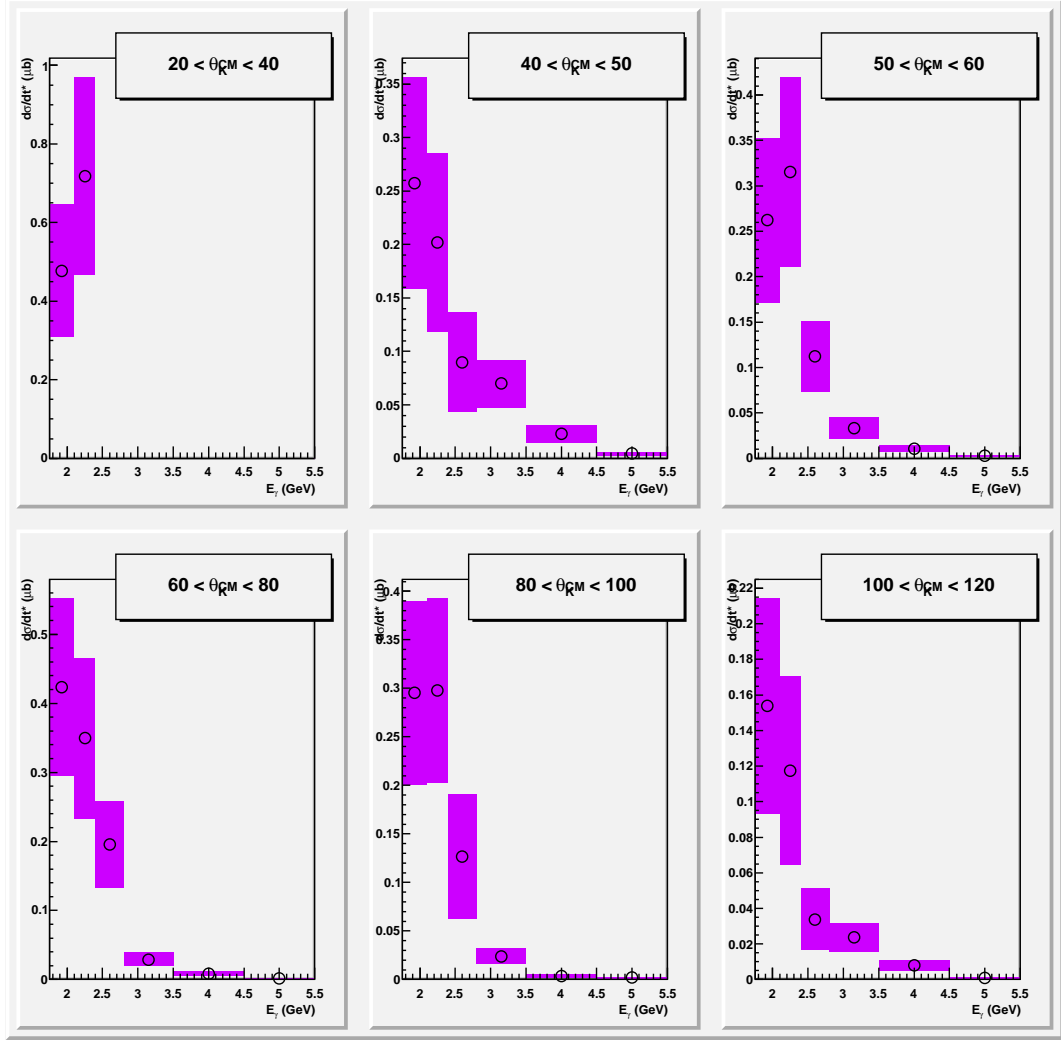FIGURE 6.47. (**Neutron Channel**), $\Lambda^*(1520)$ differential cross section $d\sigma/d\theta_{K^0}^{CM}$ distributions over E_γ at different $\theta_{K^0}^{CM}$ bins. $\theta_{K^0}^{CM}$ rises from left to right and top to bottom pads.

6.8. Total Cross Section

After extrapolating the exponential fitting functions of the $\Lambda^*(1520)$ differential cross section $d\sigma/dt^*$ distributions over t^* to the full t^* range at various E_γ bins, we integrate them and obtain the total cross section as shown in Figure 6.48. For the proton channel, at the photon energies below 2.5 GeV, the eg3 data has fewer bins and does not exhibit the threshold bump structure that the g11 data has; at the medium photon energies from 2.5 to 3.8 GeV, the eg3 result drops quickly and matches the g11 result well; at the high energies from 3.8 to 5.5 GeV, the Daresbury data is systematically higher than the eg3 results. Overall the eg3 results on protons are similar to the previous CLAS g11 results [36] and establish a systematic discrepancy with the older Daresbury results [3]. For the neutron channel, the eg3 results drop as photon energy increases just like the results in the proton channel. The magnitude of cross sections on neutrons are also close to those on protons with the ratio of neutron over proton results of 0.7±0.2. This is much higher than what the theory has expected [4] (see Section 1.3.1). The theory predicts 30 nb at the near-threshold energy for the neutron channel while our results show that it is about 400 nb. Our eg3 results on neutrons are also in contradiction to the LEPS results on neutrons [6], which are at least one order less than the results on protons and matches the theory prediction even though the LEPS coverage is at backward K^0 angles in the center of mass frame while the eg3 coverage is at forward K^0 angles.
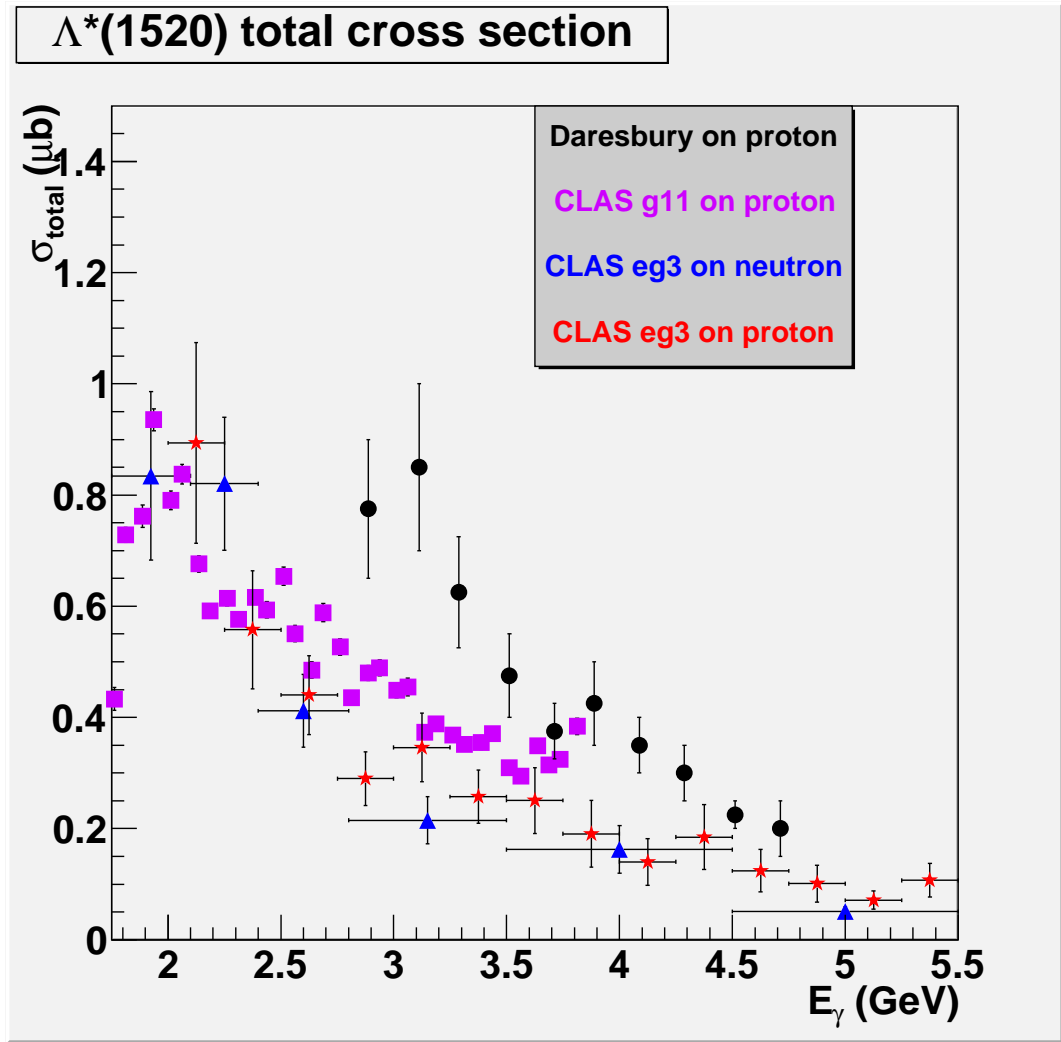
FIGURE 6.48. Total cross section of $\Lambda^*(1520)$.

6.9. Decay Angle

As mentioned in Section 1.3.2, the $\Lambda^*(1520)$ decay reveals the characteristic of the t-channel exchange particles. The distributions of K^- decay angle $cos\theta_{K-}^{GJ}$ in the Gottfried-Jackson frame at various E_γ bins are shown for the proton channel in Figure 6.49 (top) and the neutron channel in Figure 6.50 (top). In most of the bins, the distributions can be fitted well by Equation 1.1. The fitting results show strong dependence on E_γ as shown for the proton channel in Figure 6.49 (bottom) and the neutron channel in Figure 6.50 (bottom). The overall γ is very small and thus the interference term is not significant. β/α ratios are around 1, which is between the 3 for only K^* exchange and 0 for only K exchange. This indicates that both K and K^* exchanges contribute in the two reaction channels.

Note that due to our limited statistics, the decay angle distributions in this study are integrated over all θ_K^{CM} (mainly forward angles for eg3), while Ref. [5] has suggested that it can have strong dependence on E_γ as well as on θ_K^{CM}. Therefore, more data needs to be obtained in further investigations.
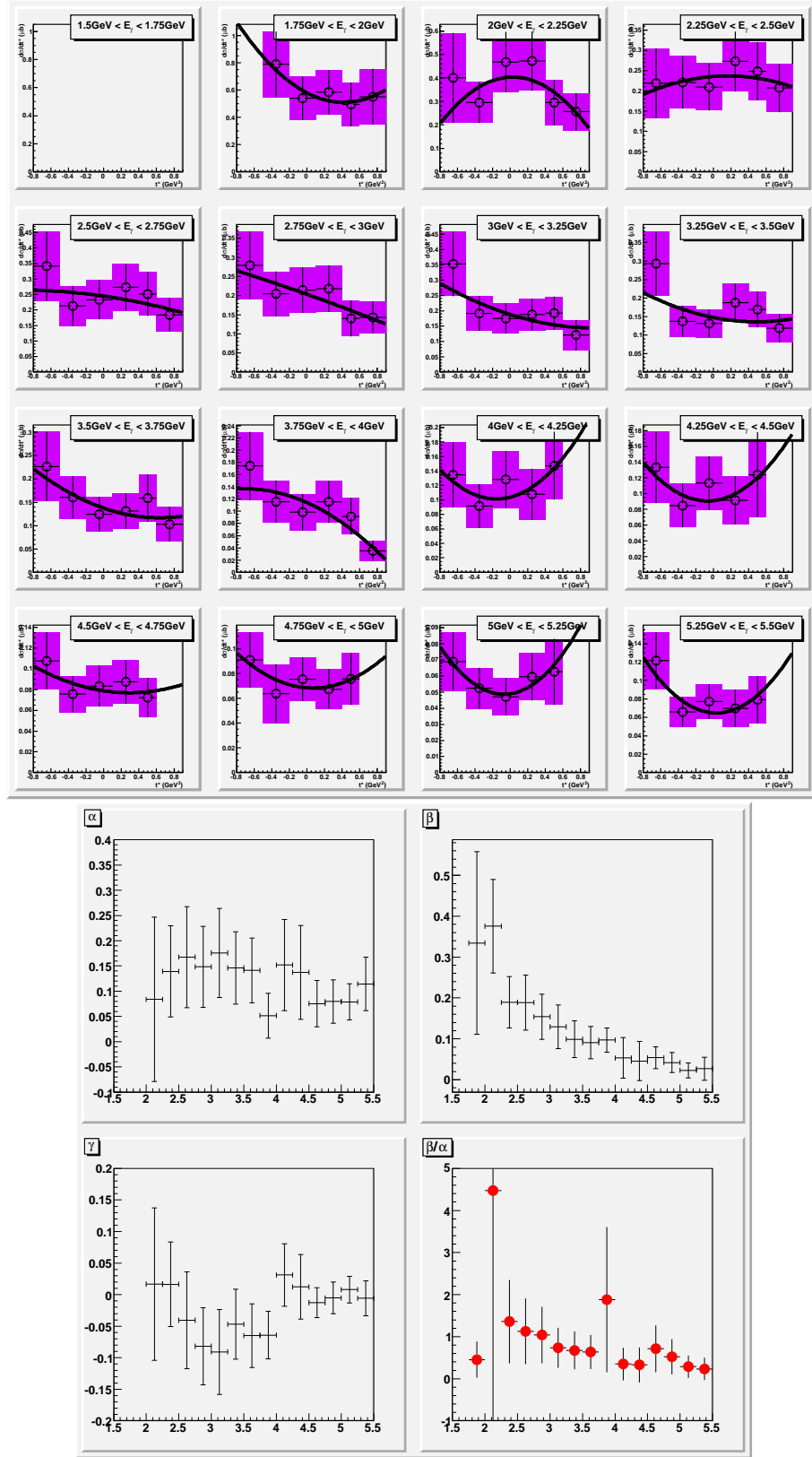
FIGURE 6.49. (**Proton Channel**), (top) the decay angle distributions at different E_γ bins. E_γ rises from left to right and top to bottom pads. (bottom) the fit results of the decay angle distributions.

125
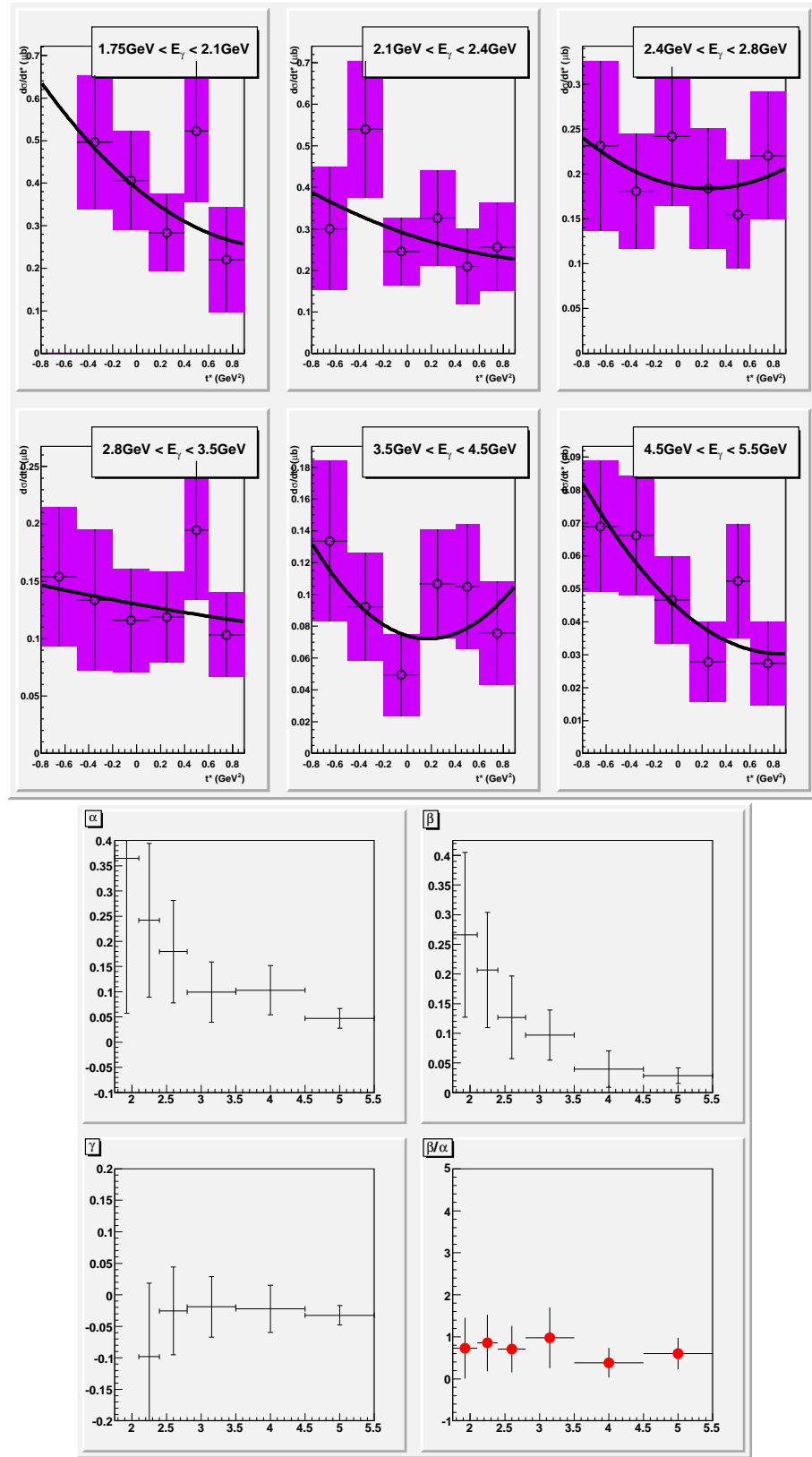
FIGURE 6.50. (**Neutron Channel**), (top) the decay angle distributions at different E_γ bins. E_γ rises from left to right and top to bottom pads. (bottom) the fit results of the decay angle distributions.

6.10. SYSTEMATICS

Only statistical errors are shown for all of the plots in this work. The systematic errors are studied by examining how much the variation of the various corrections, cuts and event selecting condition affect the cross section and decay angle results for both reaction channels. There are large contributions from the untriggered tagger T-Counter correction about 15% and the trigger efficiency correction about 20%. All other corrections and cuts applied to the experimental data only affect the final results slightly and their total systematic error is about 5%. The various event selection conditions have about total 5% error also. The systematic error of acceptance calculation from the simulation is estimated to be 6% and the normalization by using photon flux has error about 2%. The overall systematic error is about 35% for the results of cross sections and decay angle distributions in our study. This is comparable to other analyses based on the CLAS eg3 data set, like the pentaquark $\Phi^{--}(1862)$ search [33], the $\Sigma^{*-}(1385)$ cross section [38], and the Δ^{++} cross section [34].

Chapter 7

Conclusion

To better measure the cross section and decay angular distribution of the $\Lambda^*(1520)$, put constraints on the model predictions, gain insights into the production mechanism, and search possible N^* resonances, we have studied the photoproduction of $\Lambda^*(1520)$ off both protons and neutrons in deuterium by using the CLAS eg3 run data set. The reactions are $\gamma d \to K^+ \Lambda^*(n)$ with $\Lambda^* \to pK^-$ and $\gamma d \to K^0 \Lambda^*(p)$ with $\Lambda^* \to pK^-$ and $K^0 \to K_s \to \pi^+ \pi^-$.

$\Lambda^*(1520)$ differential cross sections $d\sigma/dt^*$ distributions over t^* in both reaction channels show a strong t-channel dominance over the full photon energy range, 1.75 GeV $< E_\gamma < 5.50$ GeV, which is similar to the results of previous studies from Daresbury, LEPS, and CLAS. The fitted t-slopes of the neutron channel in eg3 are flat over all energies at about $\beta = 2c^4/GeV^2$. The results of the proton channel in eg3 have very similar behavior like those from g11. It is also mostly flat above $E_\gamma = 2.5 GeV$ at about $\beta = 2c^4/GeV^2$, but rises distinctively for lower E_γ. This may be caused by the $\phi(1020)$ overlapping with $\Lambda^*(1520)$ at lower energies, but it is not investigated in this study.

The $\Lambda^*(1520)$ differential cross section $d\sigma/dt^*$ distributions over E_γ at various t^* bins show a gradual decrease with increasing photon energies for both the proton and neutron channels. There is no sign of resonance structures at any t^* bin with our limited statistics.

The $\Lambda^*(1520)$ differential cross section $d\sigma/d\theta_{K^+/K^0}^{CM}$ distributions over θ_{K^+/K^0}^{CM} at various E_γ bins in the proton and neutron channels have large contribution at forward

angles and drop quickly when they go to backward angles. This again indicates the t-channel dominance of the $\Lambda^*(1520)$ production in both reactions.

The $\Lambda^*(1520)$ differential cross section $d\sigma/d\theta_{K^+/K^0}^{CM}$ distributions over E_γ at various θ_{K^+/K^0}^{CM} bins do not have the bump structures as observed by the LEPS study [18]. Our angle coverages from $40°$ to $120°$ for the proton channel and $20°$ to $120°$ for the neutron channel only have small overlap with the LEPS angle coverage from $0°$ to $55°$, and our statistics is limited at near-threshold energies. Therefore, we cannot rule out the possibility that there is a possible nucleon resonance $N^*(2110)$ as suggested by LEPS, but the description of the eg3 data does not require the nucleon resonance.

The total cross section of $\Lambda^*(1520)$ is obtained by extrapolating the exponentially fitting functions of the differential cross section $d\sigma/dt^*$ distributions over t^* to the full t^* range at various E_γ bins and integrating them. For the proton channel, at the photon energies below 2.5 GeV, the eg3 data only has fewer bins and does not exhibit the threshold bump structure that the g11 data has; at the medium photon energies from 2.5 to 3.8 GeV, the eg3 result drops quickly and matches the g11 result well; at the high energies from 3.8 to 5.5 GeV, the Daresbury data is systematically higher than the eg3 results. Overall the eg3 results on protons are similar to the previous CLAS g11 results [36] and establish a systematic discrepancy with the older Daresbury results [3]. For the neutron channel, the eg3 results drop as photon energy increases just like the results in the proton channel. The magnitude of cross sections on neutrons are also close to those on protons with the ratio of proton over neutron results about 1.5 ± 0.5. This is much higher than what the theory has expected [4] (see Section 1.3.1). The theory predicted 30 nb at the near-threshold energy for the neutron channel while our results show that it is about 400 nb. Our eg3 results on neutrons are also in contradiction to the LEPS results on neutrons [6] which are at least one order less than the results on protons and matches the theory prediction even though the LEPS coverage is at backward K^0 angles in the center of mass frame while the eg3 coverage is at forward K^0 angles.

$\Lambda^*(1520)$ decay reveals the characteristic of the t-channel exchange particles. The distributions of K^- decay angle $cos\theta_{K^-}^{GJ}$ in the Gottfried-Jackson frame at various E_γ bins are fitted by two terms of $\Lambda^*(1520)$ spin projection $m_z = \pm 1/2$ and $m_z = \pm 3/2$ respectively and an interference term. The fitting results show strong dependence on E_γ as shown for the proton and neutron channels. The interference term is small and the ratio of $m_z = \pm 3/2$ to $m_z = \pm 1/2$ terms is around 1, which is between the 3 for only K^* exchange and 0 for only K exchange. This indicates that both K and K^* exchanges contribute in the two reaction channels. Note that due to our limited statistics, the decay angle distributions in this study are integrated over all θ_K^{CM} (mainly forward angles for eg3), while Ref. [5] has suggested that it can have strong dependence on E_γ as well as on θ_K^{CM}. Therefore, more data needs to be obtained in further investigations.

In summary, the photoproduction of the $\Lambda^*(1520)$ off both protons and neutrons in deuterium has been studied using the CLAS eg3 run data. $\Lambda^*(1520)$ differential and total cross sections and decay angle distributions are extracted in the photon energy region 1.75 GeV $< E_\gamma <$ 5.50 GeV. This is the first time that exclusive photoproduction of $\Lambda^*(1520)$ on neutrons has been reported, and we extend the results on protons to higher energies than in previous studies. $\Lambda^*(1520)$ differential cross sections in both reaction channels show a strong t-channel dominance. And there is no sign of resonance structures at the covered forward kaon angles in either channel. The total cross section on protons is similar to the world data. And the total cross section on neutrons is close to the results of the proton channel with the ratio of neutron over proton results of 0.7±0.2, which is much higher than what the theory has predicted. $\Lambda^*(1520)$ decay angle distributions in the Gottfried-Jackson frame show complicated structures indicating that both K and K^* exchanges contribute to the two reactions.

Bibliography

[1] W. M. Yao et al. Review of particle physics. *J. Phys.*, G33:1–1232, 2006.

[2] Simon Capstick and W. Roberts. $N\pi$ decays of baryons in a relativized model. *Phys. Rev. D*, 47:1994–2010, 1993.

[3] D. Barber et al. Strangeness exchange in the photoproduction of $K^+\Lambda(1520)$ between 2.8 and 4.8 GeV. *Z. Phys. C*, 7:17, 1980.

[4] Seung-Il Nam, Atsushi Hosaka, and Hyun-Chul Kim. $\Lambda(1520, 3/2-)$-photoproduction reaction via $\gamma N \rightarrow K\Lambda * (1520)$. *Phys. Rev. D*, 71(11):114012, Jun 2005.

[5] Seung-il Nam and Chung-Wen Kao. $\Lambda(1520)$ photoproduction off a proton target with regge contributions. *Phys. Rev. C*, 81(5):055206, May 2010.

[6] N. Muramatsu et al. Near-threshold photoproduction of $\Lambda(1520)$ from protons and deuterons. *Phys. Rev. Lett.*, 103(1):012001, Jul 2009.

[7] S. P. Barrow et al. Electroproduction of the $\Lambda(1520)$ hyperon. *Phys. Rev. C*, 64(4):044601, Aug 2001.

[8] Richard Feynman. Quantum electrodynamics. *ISBN 978-0201360752*, 1998.

[9] Walter Greiner and Andreas Schafer. Quantum chromodynamics. *ISBN 0-387-57103-5*, 1994.

[10] Rajan Gupta. Introduction to lattice QCD. *arXiv hep-lat/9807028*, 1997.

[11] Murray Gell-Mann. Symmetries of baryons and mesons. *Phys. Rev.*, 125(3):1067–1084, Feb 1962.

[12] Simon Capstick and W. Roberts. Strange decays of nonstrange baryons. *Phys. Rev. D*, 58(7):074011, Sep 1998.

[13] T. Nakano et al. Evidence for a narrow $S = +1$ baryon resonance in photoproduction from the neutron. *Phys. Rev. Lett.*, 91(1):012002, Jul 2003.

[14] T. Nakano et al. Evidence for the Θ^+ in the $\gamma d \to K^+ K^- pn$ reaction by detecting $K^+ K^-$ pairs. *Phys. Rev. C*, 79(2):025210, Feb 2009.

[15] Y. Qiang et al. Properties of the $\Lambda(1520)$ resonance from high-precision electroproduction data. *arXiv:1003.5612v1 [hep-ph]*.

[16] T. Azemoon et al. Production of hyperons by virtual photons. *Nuclear Physics B*, 95(1):77 – 97, 1975.

[17] A. M. Boyarski et al. Photoproduction of K^+-hyperon from hydrogen and deuterium at 11 GeV. *Physics Letters B*, 34(6):547 – 550, 1971.

[18] H. Kohri et al. Near-threshold $\Lambda(1520)$ production by the $\gamma \to p \to K + \Lambda(1520)$ reaction at forward $K+$ angles. *Phys. Rev. Lett.*, 104(17):172001, Apr 2010.

[19] Seung-il Nam, Ki-Seok Choi, Atsushi Hosaka, and Hyun-Chul Kim. Test of the reaction mechanism for $\gamma N \to K\Lambda(1520)$ using the polarized photon. *Phys. Rev. D*, 75(1):014027, Jan 2007.

[20] A. I. Titov, B. Kämpfer, S. Daté, and Y. Ohashi. Coherent Θ^+ and $\Lambda(1520)$ photoproduction off the deuteron. *Phys. Rev. C*, 72(3):035206, Sep 2005.

[21] B. A. Mecking et al. The cebaf large acceptance spectrometer (clas). *Nuclear Instruments and Methods in Physics Research Section A: Accelerators, Spectrometers, Detectors and Associated Equipment*, 503(3):513 – 553, 2003.

[22] D. I. Sober et al. The bremsstrahlung tagged photon beam in hall b at jlab. *Nucl. Instrum. Methods A*, 440(2):263 – 284, 2000.

[23] E. Smith et al. Proposal to search for excotic cascades with clas using an untaggered virtual photon beam. *CLAS Proposal*, 2003.

[24] CLAS-CVS packages/user_ana.

[25] CLAS-CVS packages/fsgen.

[26] CLAS-CVS packages/gsim_bat.

[27] CLAS-CVS packages/gpp.

[28] E. Pasyuk. Energy loss corrections for charged particles in clas. *CLAS-NOTE*, (2007-016), 2007. CLAS-CVS packages/eloss.

[29] Paul Mattione. Kinematic fitting of detached vertices. *JLAB-PHY-07-643*, 2007. CLAS-CVS packages/utilities/decayutils.

[30] H. Crannell D. Sober, , and F.J. Klein. The tagger energy scale: Interpreting the cmu kinematic fit results. clas note . *CLAS-NOTE*, (2004-019), 2004.

[31] Maurizio Ungaro and Ji Li. Procedure for drift chamber inefficiencies. *CLAS-NOTE*, (2003-006), 2003. CLAS-CVS packages/utilities/pdu/dc_eff.

[32] J. Ball and E. Pasyuk. Photon flux determination through sampling of "out-of-time" hits with hall b photon tagger. *CLAS-NOTE*, (2005-014), 2005. CLAS-CVS packages/utilities/gflux.

[33] H. Egiyan et al. Upper limits for the photoproduction cross section for the $\Phi^{--}(1862)$ pentaquark state in $\Sigma^- \pi^-$ decay channel using eg3 data. *CLAS-ANALYSIS 2009-104*, 2009.

[34] L. Graham et al. Normalization study of the eg3 data through Δ^{++} investigation. *CLAS-NOTE 2009-106*, 2009.

[35] C. Wu et al. Photoproduction of ρ mesons and Δ-baryons in the reaction $\gamma p \to p\pi^+\pi^-$ at energies up to $\sqrt{s} = 2.6$ GeV. *Eur. Phys. J.*, A23:317–344, 2005.

[36] R. De Vita. *private communication*.

[37] R. Bradford et al. Differential cross sections for $\gamma + p \to K^+ + Y$ for Λ and Σ hyperons. *Phys. Rev. C*, 73(3):035202, Mar 2006.

[38] H. Y. Lu et al. Exclusive photo-production measurement of $k^+\sigma^{*-}$ off quasi-free neutrons in deuterium. *PhD Dissertation, University of South Carolina*, 2010.